TABLE OF CONTENTS

1. Robmech

2. PRASA

3. SAUPEC

2019 SAUPEC/RobMech/PRASA Conference
Bloemfontein, South Africa, January 28-30, 2019

Concentrated Thermal Photovoltaic Power Generation Improvement Through the Use of Three-Dimensional Technology

Olufunmilayo Alice Mafimidiwo
mafimidiwoo@ukzn.ac.za; alicemafi1@gmail.com
School of Engineering,
Howard College Campus,
University of KwaZulu-Natal,
King George V Avenue
Durban, 4041, South Africa

Akshay Kumar Saha
Saha@ukzn.ac.za
School of Engineering,
Howard College Campus,
University of KwaZulu-Natal,
King George V Avenue
Durban, 4041, South Africa

***Abstract*— Recent research conducted on improving solar power generation and efficiency has led to the study and the use of new technology in three-dimensionality in achieving these tasks. This paper presents the modelling and simulation of a concentrated thermal photovoltaic system in two-dimensions and three-dimensions to investigate the effect of three-dimensional technology on concentrated thermal photovoltaic structures of similar capacity and materials. The results showed that the performances of the system modelled in three-dimensions is better than that modelled in two-dimensions in terms of the generated output power as well as the efficiency. Furthermore, the point graphs and other simulated plots were obtained on the modelled two-concentrated thermal photovoltaic system and the three-concentrated thermal photovoltaic system. The results obtained revealed that the damaging effect of temperature was much less on the three-dimensional concentrated thermal photovoltaic system than that of the two-dimensional concentrated thermal photovoltaic system.**

***Keywords*— Solar power generation, efficiency, three-dimensional technology, concentrated thermal photovoltaic system, modelling and simulation**

I. INTRODUCTION

Generation of solar energy through the use of three-dimensional (3D) technology is becoming a household name for improving the generated output power and efficiency of solar system. The 3D technology is relatively a newer technique of solar power generation when compared with the regular method of two-dimensional (2D) power generation otherwise known as the convectional method. The 3D technology is fast gaining ground all over the world. The realization that physical devices possess 3D images while the traditional display is capable of showing only 2D flat images that is devoid of depth has informed the study on enhancing solar power generation through 3D technology.
According to research study in 3D technology, solar energy structures have been discovered to take in light and produce more energy in the ratio 2 - 20 higher than the flat panels of the same area footprint [1], [2]. Researchers in solar energy generation are now taking the advantages of 3D technology to optimize the solar energy generated [3], [4]. Other scholars who have also researched into 3D technology [5], [6], [7] have established that 3D structures favour more significant generation of electrical power and higher efficiency than the conventional planar 2D structures.

Solar energy generation can be either by photovoltaics (electricity generation directly from the sunlight energy) [8], [9] or by concentrated power (electricity generation from concentrating sunrays that pass though lenses and mirrors onto small, but highly efficient photovoltaic solar cells [10], [11] with multi-junctions (MJ)]. The solar energy generation being considered in this paper is that of concentrated power.

II. OPERATING PRINCIPLE OF CONCENTRATED THERMAL PHOTOVOLTAIC SYSTEM

The concentrated thermal photovoltaic system (CTPV) device is hereby presented as an energy circle with burning fuel (flame) inside which represents the solar energy radiating a high degree of heat by using mirrors or lenses to concentrate the heat which is captured by the small area of the PV cells. The combustion of fuel and the radiated heat in the concentrating medium of the CTPV system is then converted to electricity [12]. The normal efficiency of a CTPV system varies between one percent and twenty percent [13], [7]. The unutilized radiated heat in the system escapes as loss and combines with the heat transferred through conduction in the CTPV system to increase the temperature of the PV cells, thereby reducing the amount of electrical power generated and its efficiency. The nature of the materials configuration used in the CTPV system affect the extent to which heat is lost.

A. Concentrated thermal photovoltaic modelling and simulation in 2D and 3D

The modelling of the CTPV system was carried out using COMSOL Multiphysics software. The CTPV system was modelled as an energy circle with heat at its center and containing other modelled materials. A prototype of such system is as shown in Figure 1.

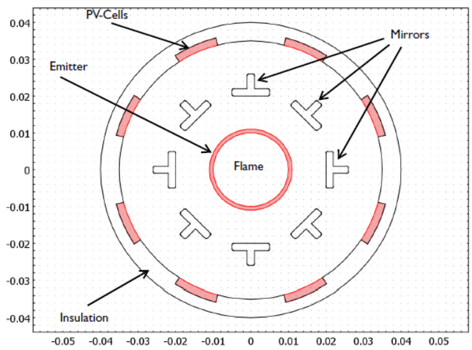

Figure 1: Geometry and dimensions of modelled Thermal PV system [13]

The thermal properties of the CTPV system and of the materials used, were modelled both in 2D and in 3D. All modelling details like the definition, geometry, dimensions and meshing were also carried out as 2D and 3D models. The materials used in modelling the CTPV system were the followings:

i. The emitter, with assigned specific temperature, $T_{\_heater}$, on the inner boundary.
ii. The mirrors of low emissivity that were used in concentrating the rays on the PV cells.
iii. The PV cells of high emissivity on which the sun rays were concentrated.
iv. The insulation of low emissivity.

The physical properties of these materials are as presented in Table 1 and some of the models achieved are presented in Figure 2(a) to Figure 2(j).

B. *Table 1: Properties of the materials used in the CTPV modelling [13]*

Component	*k* [W/(m·K)]	ρ (rho) [kg/m³]	*Cp* [J/(kg·K)]	ε
Emitter	10	2000	900	0.99
Mirror	10	5000	840	0.01
PV Cell	93	2000	840	0.99
Insulation	0.05	700	100	0.1

Conduction of heat on different boundaries took place in the CTPV system. In order to reduce temperature resulting from the heat generated, water was used as coolant on the CTPV rear surface (their interface with the insulator). On the PV cells inner boundaries, radiation boundary conditions were applied. The heat generated by the PV cells was doused by the heat sinks provided on the inner boundaries of the PV cells, hence more of the irradiation was converted to electricity. The boundary heat source, q, is as given in (1).

$$q = -G\eta_{pv} \tag{1}$$

where,

G = irradiation flux (W/m^2), and

η_{pv} = Voltaic efficiency of the PV panel

At the outer boundary of the PV cells, water cooling by convection was applied which satisfied the convective heat transfer with the water cooling equation defined in (2) as:

$$q_0 = h \,.\, (T_{ext} - T) \tag{2}$$

where,

The heat flux is q_0 and the heat flux is for any fluid which can be liquid or gas/air. The fluid considered here is water.

For water;

$h = h_{water}\ (D, T_{ext}\ )$,

h_{water} was set at 5 W/m^2K

T_{ext} = external or ambient temperature = 293.15 K

On the insulation inner boundaries, radiation boundary conditions were also applied while at the outer boundary of the insulation, convective cooling for air was set and applied with h set to 5 $W/(m^2{\cdot}K)$ and T_{amb} to 293 K.

The emitter was simulated the with a fixed temperature, $T_{\_heater}$, on the inner boundary while at the outer emitter boundary, surface-to-surface radiation was applied.

The physics and the global definition prevailing on the operations of the PV cells and the heater are as presented in Table 2.

Table 2: Global definition for the PV Cell and the heater

Name	Expression	Unit	Description
eta_pv	if(T<1600[K], 0.2 x (1 - (T/800[K] - 1)^2), 0)		Voltaic efficiency, PV cell
q_out	ht.Gm x eta_pv	W/m^2	Electric output power
T_heater	1000 [K]	K	Temperature, emitter inner boundary

C. Other operating equations in the modelling.

The following equations were operated in determining the activities taking place in the CTPV system.

According to [14] the heat exchange equations as expressed in by conduction and convection for solid and fluid domains in (3) and (4) are:

$$\rho C_p \mathbf{u} \cdot \nabla T + \nabla \cdot \mathbf{q} = Q + Q_{ted} \tag{3}$$

$$\mathbf{q} = -k\nabla T \tag{4}$$

The efficiency η_{pv} of the PV cells is directly related to the surrounding temperature as expressed [14] in (5) as:

$$\eta_{pv} = \begin{cases} 0.2\left[1 - \left(\frac{T}{800\ K} - 1\right)^2\right] & T \leq 1600\ K \\ 0 & T > 1600\ K \end{cases} \tag{5}$$

The unconverted radiation was generated as heat which raised the PV cells temperature and therefore dropped the PV cells efficiency. The heat transfer equation, when expressed as an internal heat generated, Q, is a function of the efficiency of the PV panel, η_{pv}, the surface area of the PV panel, A_{panel} and the volume of the PV cells in the panel, $V_{pc.panel}$. The heat transferred is related to the absorbed solar radiation as expressed in (6) as:

$$Q = \frac{(1 - \eta_{pv})\ x\ S\ x\ A_{panel}}{V_{pc.cell}} \tag{6}$$

III. SIMULATIONS AND RESULTS

The geometric data obtained for the modelled 2D and 3D CTPV systems are summarised in Table **3.** The several boundary selections for the 2D and 3D were different in number. The 3D model considered the various points on the x, y and z axes while 2D model considered only the x and y planes. These boundary selections are significant in the required physics application for the modelling and simulation. The comparative analysis of the geometry for the modelled 2D and 3D CTPV systems are in Table 3.

Table 3: Geometry statistics of Two-dimensional and Three-dimensional Geometries

2D Geometry		3D Geometry	
Description	**Value**	**Description**	**Value**
Space dimension	2	Space dimension	3
Number of Domains	20	Number of Domains	20
Number of boundaries	184	Number of boundaries	224
Number of edges	Not applicable	Number of edges	544
Number of vertices	176	Number of vertices	352

The effect of modelling in 2D and 3D (while maintaining the number of PV cells/mirrors as eight) on the temperature distribution, efficiency and the electrical power output of the CTPV system was studies and analysed. The modelled materials for the 2D and 3D CTPV systems are comparatively illustrated in Figure 2(a) to Figure 2(j).

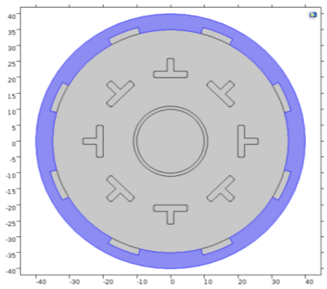

Figures 2(a): Modelled insulation for 2D CTPV system

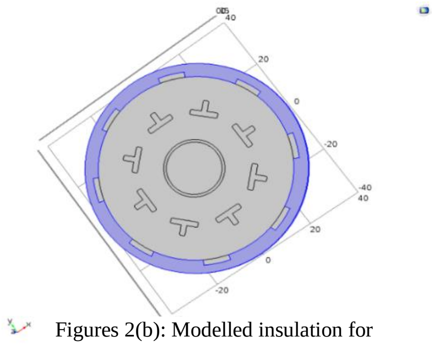

Figures 2(b): Modelled insulation for 3D CTPV system

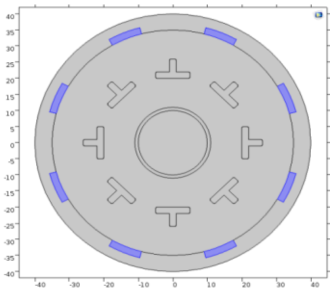

Figures 2(c): Modelled PV cells for 2D CTPV system

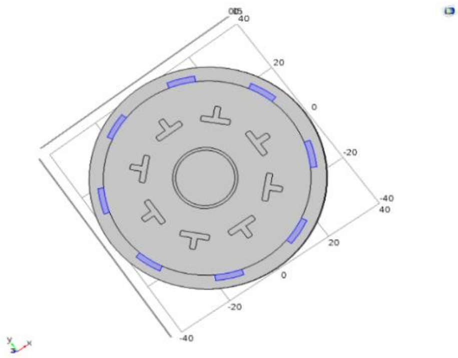

Figures 2(d): Modelled PV cells for 3D CTPV system

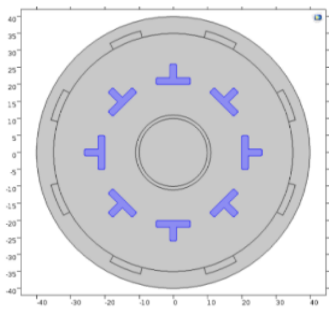

Figures 2(e): Modelled mirrors for 2D CTPV system

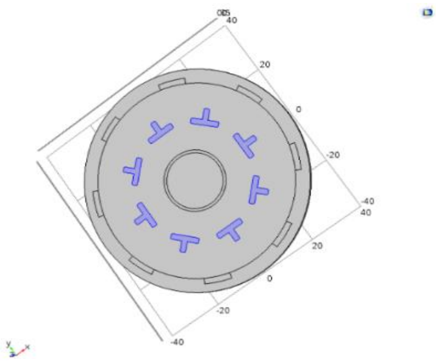

Figures 2(f): Modelled mirrors for 3D CTPV system

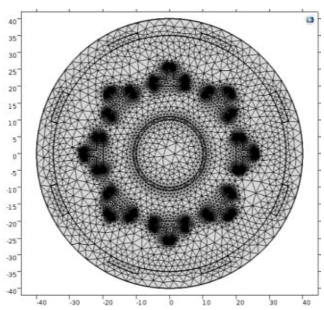

Figures 2(g): Meshed result of 2D CTPV thermal PV system

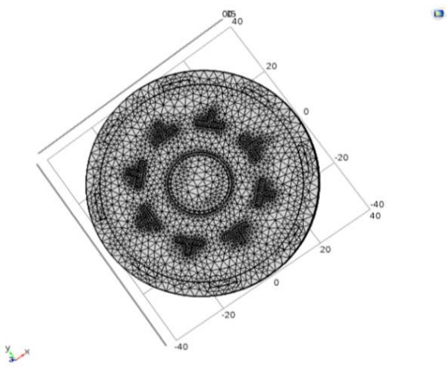

Figures 2(h): Meshed result of 3D CTPV thermal PV system

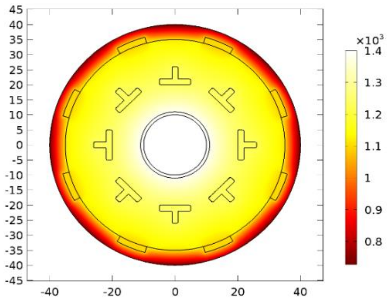

Figures 2(i): Stationary temperature distribution of modelled 2D CTPV system

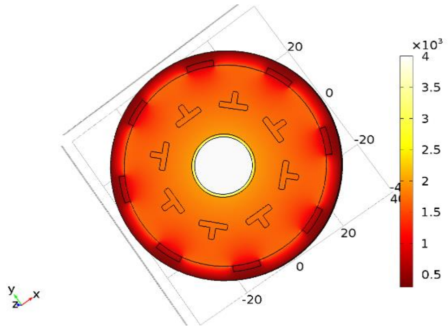

Figures 2(j): Stationary Temperature distribution of modelled 3D CTPV system

IV. RESULTS

The results obtained for the 2D and 3D simulations are presented graphically in Figure 3(a) to Figure 3(f) and are as summarised in Table 4.

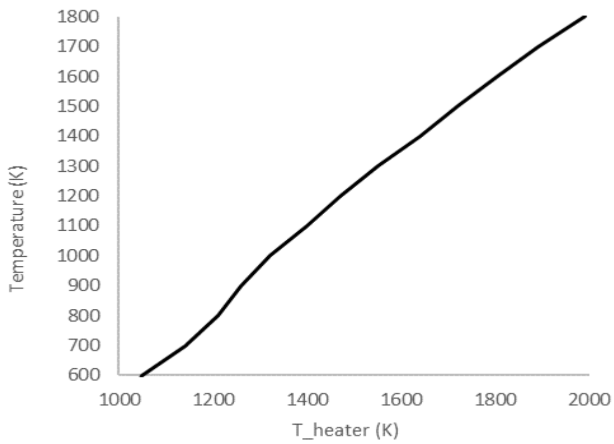

Figure 3(a): Point graph - Temperature variation in a 2D CTPV system

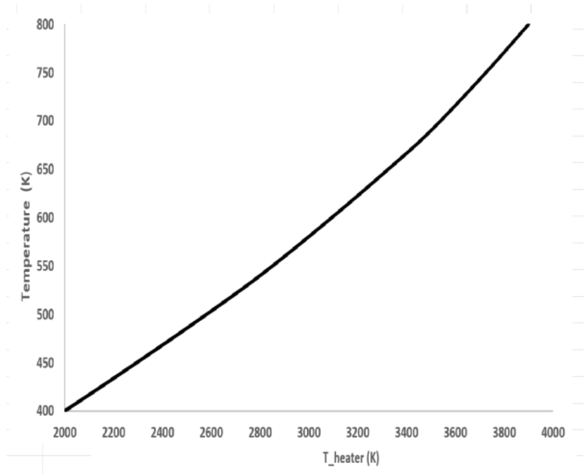

Figure 3(b): Point graph - Temperature variation in a 3D CTPV system

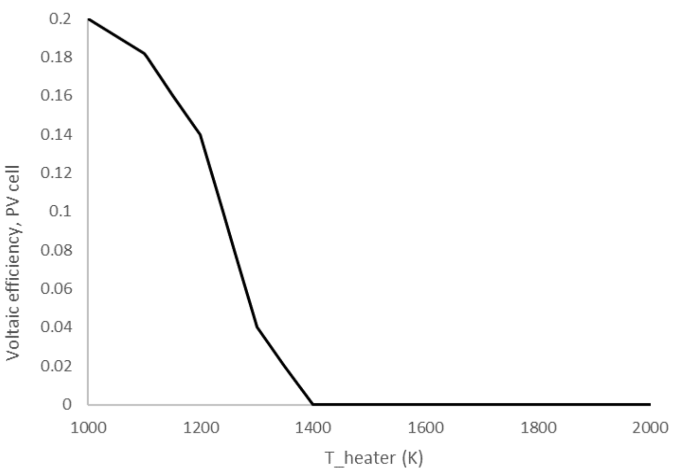

Figure 3(c): Voltaic efficiency versus Temperature in a 2D CTPV system

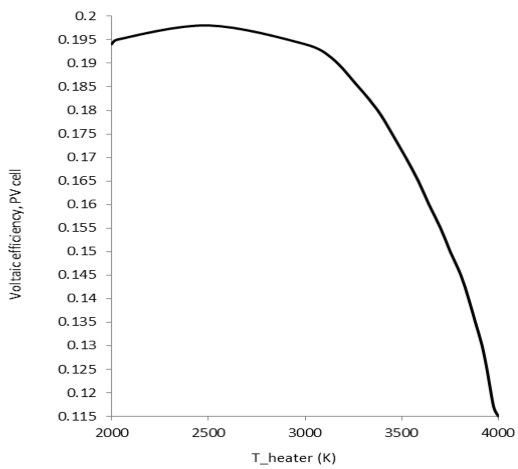

Figure 3(d): Voltaic efficiency versus Temperature in a 3D CTPV system

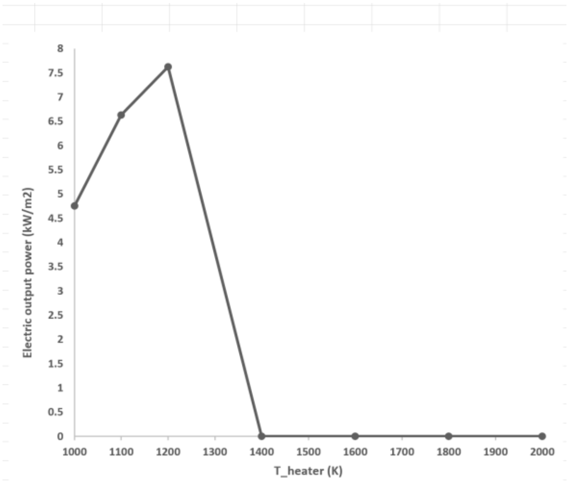

Figure 3(e): Electric power output versus Temperature in a 2D CTPV system

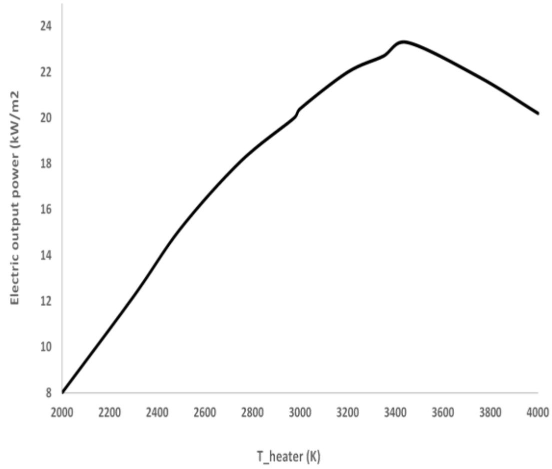

Figure 3(f): Electric power output versus Temperature in a 3D CTPV system

Table 4: Results summary on 2D and 3D CTPV modelling

Parameters	**2D CTPV system**	**3D CTPV system**
Prevailing operating condition (Emitter temperature)	1,400 K	4,000 K
Temperature range for the heater operation	1,000 K to 2,000 K	2,000 K to 4,000 K
Maximum output power operating condition (Emitter temperature)	1,200 K	3,600 K
PV cells attained temperature	1,820 K	850 K
PV cells optimal output power temperature	780 K	715 K
Output power	7.8 kW/m^2	23.2 kW/m^2
CTPV system attained efficiency	19.8 %	19.9%

V. CONCLUSION

The CTPV system and its materials were successfully modelled in 2D and 3D. Some of the modelled results are presented in Figures 2(a) to Figure 2(j). The geometric statistics obtained for the 3D CRPV system were more indepth than those of the 2D. The voltaic efficiency of the 2D CTPV in Figure 3(c) was almost the same with that of the 3D in Figure 3(d) but it could not be sustained for long for the 2D CTPV system before it would drop to zero at any temperature beyond 1400 K while that of the 3D was better fairly distributed and sustained Figure 3(d). The 3D CTPV system for the 3D was able to operate safely under the effect of more intense heat without its PV cells temperature getting unnecessarily heated-up as seen in Table 4. Hence, the heat was not excessive to cause any hinderance for the generated output power and its efficiency. The generated output power of the 3D CTPV system was able to reach 23.2 kW/m^2 as against that of the 2D CTPV system with value of 7.8 kW/m^2. This paper has been able to establish that the 3D configuration is capable of giving better performance than the same system of 2D CTPV of the same capacity and materials composition and physics. The paper could allow potential increase in the use CTPV system.

VI. LIST OF ENGINEERING SYMBOLS

Some Engineering symbols/abbreviations	Meanings/interpretations
n	surface normal
$\boldsymbol{\varepsilon}$	surface emissivity
$\boldsymbol{\sigma}$	Stefan-Boltzman constant = 5.67x10^{-8} W/m^{2}K^4
C_p	Specific heat capacity of the fluid (J/kg K)
k	thermal conductivity of the fluid (W/m K)
ρ	Density of film of the fluid on the front face of the PV module (kg/m^3)
u	velocity of the fluid (m/s)
p	pressure of the fluid (Pa)
μ	dynamic viscosity of the fluid on the front face of the PV module (Pa s)
q	Heat transferred by conduction (W)
Q	Internal Heat Generation (W)
μ_T	Turbulent viscosity (Pa s)
k	Turbulent kinetic energy
K	Temperature unit in Kelvin
T_{pv}	Temperature for the surface of the module
T_{heater}	Temperature for emitter inner boundary
T_{amb}	Ambient temperature
η_{pv}	Voltaic efficiency of the PV Panel
η_{elec}	Efficiency of the PV module
η_{Tref}	PV module efficiency at reference conditions
T_{pv}	Surface temperature of the PV module
β_{ref}	Thermal coefficient of the PV module
G	Irradiation flux (W/m2)
G_{amb}	Ambient irradiation (W/m^2.K)
Q_{vd}	Viscous dissipation ()
F	Geometric factor
F_{amb}	Geometric factor for the ambient
k_{cond}	Thermal conductivity (W/m K)

REFERENCES

[1] B. Myers. M. Bernardi and J. C. Grossman. Bryan Myers, "Three-Dimensional Photovoltaics," *American Institute of Physics,* vol. 96, pp. 071902 - 071902-3, 2010.

[2] O.A. Mafimidiwo and A.K. Saha “Incorporating three dimensional Photovoltaic structure for optimum solar power generation - the effect of height” in DOHET, Journal of Energy in Southern Africa (JESA). Date of acceptance: December, 2015.

[3] N. F. Marco Bernardi, Jin H. Wan, Rachelle Villalon and Jeffrey C. Grossman, "Solar Energy Generation in Three Dimensions," The Royal Soceity of Chemistry, pp. 1-5, 2012.

[4] O.A. Mafimidiwo and A.K. Saha “Improving Solar Energy Generation Through the use of Three-dimensional Photovoltaics Technology, Proceedings of the 22nd Southern African Universities Power Engineering Conference (SAUPEC) – Digital Edition, 30 – 31 January 2014, University of KwaZulu-Natal, Durban, South Africa, pp. 294-300; print ISBN: 978-1-86840-619-7 Publisher: Southern African Universities Power Engineering Conference.

[5] L. T. Seiji Suzumoto1, Toshiaki Yachi, "Output Power Characteristics of a Three-Dimensional Photovoltaic Module Using Fibonacci Number Composition," IEEE, p. 7, 2012.

[6] A. Yuji and T. Yachi, "A novel photovoltaic module assembled three-dimensional," in Photovoltaic Specialists Conference (PVSC), 2010 35th IEEE, 2010, pp. 002811-002816.

[7] O.A. Mafimidiwo and A.K. Saha “Incorporating three dimensional Photovoltaic structure for optimum solar power generation - the effect of height” in DOHET, Journal of Energy in Southern Africa (JESA), 2016.

[8] J.O. Oji, N. Idusuyi, T.O. Aliu, M.O. Petinrin, O.A. Odejobi. and A.R. Adetunji. “Utilization of Solar Energy for Power Generation in Nigeria”. In International Journal of Energy Engineering, DOI: 10.5923/j.ijee.20120202.07, 2(2): 54-59, 2012

[9] A. Sahaya, V.K. Sethia. and A.C. Tiwarib. “Cost Performance of Thin Film and Crystalline Photovoltaic Cells – A Comparative Study”. In International Journal of Current Engineering and Technology, ISSN 2277 – 4106, Vol.3, No.3, 2013

[10] S. Philipps, A. Bett, K. Horowitz, and S. Kurtz, "Current Status of Concentrator Photovoltaic (CPV) Technology," National Renewable Energy Laboratory (NREL), Golden, CO.2015.

[11] H.L. Zhang, J. Baeyens, J. Degreve and G. Caceres “Concentrated solar power plants: Review and design methodology”. In Elsevier Journal on Renewable and Sustainable Energy Reviews,2013

[12] C. Renno and F. Petito, "Energy Analysis of a Concentrating Photovoltaic Thermal (CPV/T) System," Energy Science and Technology, vol. 6, pp. 53-63, 2013.

[13] AB, COMSOL, "Thermo-Photo-Voltaic Cell," In Application Library path: Heat_Transfer_Module/Thermal_Radiation/tpv_cell, COMSOL Multiphysics User’s Guide, Version 5.1, Ed., ed, p. 22, 2015

[14] M.U. Siddiqui, A.F.M. Arif, L. Kelley, and S. Dubowsky, "Three-dimensional thermal modeling of a photovoltaic module under varying conditions," Solar Energy, vol. 86, pp. 2620-2631, 9// 2012.

2019 SAUPEC/RobMech/PRASA Conference
Bloemfontein, South Africa, January 28-30, 2019

Optimal Distribution Automation Devices Placement for Reliability Improvement of a Real Distribution Network with Sub-Feeders Considering Customer Interruption Cost

J. Masimula* and K. Awodele**

**Department of Electrical Engineering, University of Cape Town, Rondebosch 7701, Cape Town, South Africa. Email: *20923591jr@gmail.com **kehinde.awodele@uct.ac.za*

Abstract: This paper presents predictive analytical and simulation approaches to reliability worth/cost assessments conducted on a test system and a typical Cape Town real system. Feeder 3 of bus 6 of the RBTS was utilized to illustrate various cases of switch configurations and for each arrangement the reliability indices were evaluated analytically as well as in Monte Carlo Simulation and results found to be similar. The objective function behind placement can either be based on SAIDI or the ECOST and the best switch position for SAIDI might be worst position for the ECOST. In this paper three scenarios were investigated in the Waterkloof Farmers-1 11 kV network (real system); Reliability assessment was firstly performed without automation devices (Scenario 1), secondly with automation devices in the current or existing positions (Scenario 2) and lastly, with optimal placement of automation the devices on the feeder using analytical and evolutionary algorithms methodologies (Scenario 3).

Keywords: Reliability, Distribution automation devices, Interruption, Customer, Artificial intelligence.

1. INTRODUCTION

The distribution system remains the integral part of the power system since they account for up to 90% of all customer reliability problems [1]. The medium voltage (MV) network is usually very large and exposed to external disturbances such as bad weather and vegetation. Modern society has come to expect a continuity of supply since delicate electrical devices are connected to the grid. Interruptions are usually caused by random failures of equipment and system, which are generally beyond the control of power system engineers or personnel. The impacts of unplanned outages is not restricted to the loss of revenue by service providers but also include indirect costs imposed on the society and environment due to the outage [1], [2]. The basic load-point reliability indices employed to predict the reliability of a distribution system are the average load point failure rate (λ_s), the average load point outage duration (r_s), and the average annual load point unavailability (U_s) [3]. The indices work in a way such that the lower the indices the more reliable the system is. The reliability and load-point indices are often determined on annual basis and following stochastic nature of power system, the yearly indices are random variables and functions of the repair times, failure rates and restoration times within a year [4].

There are two basic approaches to reliability evaluation namely, analytical and simulations approaches [5]. The customer interruption cost (CIC) is defined in [6] as the degree of the loss that the consumer suffers as result of unavailability of electrical power supply. The objective of optimal switch placement is to find the best possible configuration of switch locations which minimises the total cost (including Investment cost, O&M cost of switching device and customer interruption cost) and still meet reliability indices [7].

There are quite several approaches towards solving optimization problem. Typical heuristic methodologies are illustrated in Figure 1. In exact optimization; the optimization problem is mathematically formulated and solved. This approach is basically based on principles that involve certain degree of trial-and-error or exploratory problem-solving. Evolutionary algorithms (EA), genetic algorithms (GA) and particle swarm optimization (PSO) algorithms are typical examples of meta-heuristic methodologies and are set-based algorithms [8]. Both GA and PSO are more applicable to solve this specific problem, since the problem can be modelled in a manner that suit the mechanics of the algorithms [8], [10].

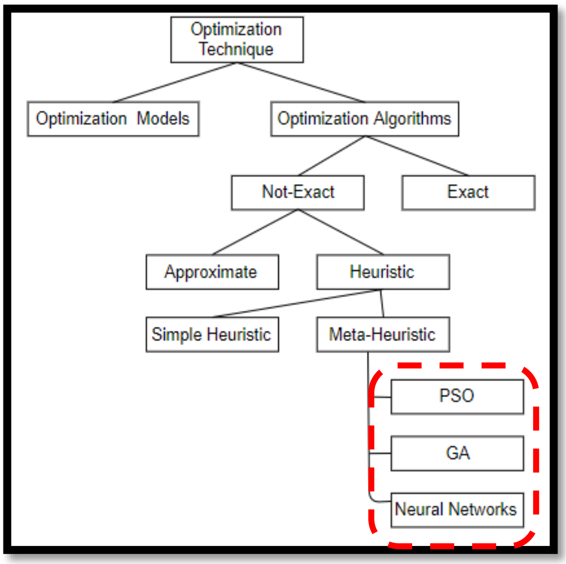

Figure 1: Types of Optimization Techniques [8]

2. RELIABILITY WORTH/COST ASSESSMENT TEST SYSTEM

The assessment was carried out on a test system called the Roy Billinton Test System (RBTS). The RBTS is a small 6-bus system which was established for educational purposes. Bus 6 consists of four feeders namely F1, F2, F3 and F4 and total number of customers connected in the respective feeders are 764 customers in F1, 969 customers in F2, 22 customers in F3 and 1183 customers in F4. The lengths of the feeder sections of bus 6 are adopted from [11] and presented in table 1 below.

Table 1: Bus 6 Components Lengths [11]

Feeder Type (**Bus 6**)	Length (km)	Feeder Section Numbers
1	0.6	2 3 8 9 12 13 17 19 20 24 25 28 31 34 41 47
2	0.75	1 5 6 7 10 14 15 22 23 26 27 30 33 43 61
3	0.8	4 11 16 18 21 29 32 35 55
4	0.9	38 44
5	1.6	37 39 42 49 54 62
6	2.5	36 40 52 57 60
7	2.8	35 46 50 56 59 64
8	3.2	45 51 53 58 63
9	3.5	48

Figure 2 illustrates the distribution network of bus 6 of the RBTS and highlighted is feeder 3 (F3) where 5 cases of various switch configuration were investigated to show the impact of switching device on the reliability of distribution systems. The values in Table 1 were utilized to conduct relevant reliability evaluations on the network. The Failure Modes Effect Analysis (FMEA) for analytical and Monte Carlo simulations approaches were used for reliability evaluation. The reliability data of the RBTS was adopted from [12] for both the 33 kV and 11 kV network components and it consist of adequate information to perform basic assessments incorporated in this paper. Disconnects and fuses are assumed to be 100% reliable, failure rate, switching times, repair times, lengths of line are espoused from [11]. According to reference [3], lines and cables in practice have a failure rate proportional to their length. Consequently, the main feeder sections or components (L1-L64) have a failure rate of 0.065 f/km yr. [3]. The 11 kV Feeder 3 of RBTS (F3) was considered in the research. Results obtained were validated with that found in literature.

The different switch configurations conducted on F3 of bus 6 RBTS are as follows;

- **Base Case** - F3 with 3 witches (original).
- **Case 1**- F3 with 1 switch placed (in component 29).
- **Case 2** - F3 with 1 switch (in component 31).
- **Case 3** - F3 with 1 switch (in component 33).
- **Worst Case** - F3 without switches.

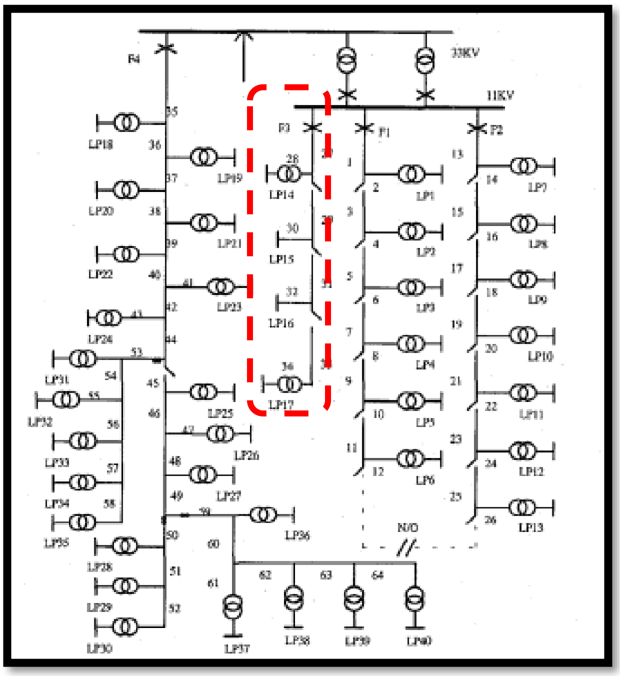

Figure 2: Bus 6 of the RBTS [3]

OPTIMAL SWITCH PLACEMENT WATERKLOOF FARMERS-1 11 KV NETWORK

The real system (Pilot feeder) to be modelled is the Waterkloof Farmers 1 11 kV distribution feeder. The reliability performance of this pilot feeder is assessed to see if automation devices installed in the network are in the most optimal positions. The overview of the real network to be assessed is demonstrated in Figure 3 and showing the current positions of the automation devices such as Fuse saver, Trip saver, IntelliRupter, Recloser and FPI. The reliability-network-equivalent approach was implemented since it simplifies the analytical process. Both approaches were used based on the assumptions that the failure rate of the pilot feeder is 1.0947 f/km.yr, transformer failure rate per year is 0.015, repair time is 5 hours, switching time is 1 for manual switches while with automation devices its 10 minutes, the reliability of protection devices is 100 % and transformer replacement with a spare would take 10 hrs. [14].

The three configurations investigated in the pilot feeder are as follows:

- **Scenario 1**- The reliability was assessed on the real system without automation devices such as the fuse saver, trip saver, IntelliRupter and recloser. The system is only left with the standard fuses and manual disconnects or switches.
- **Scenario 2**- Reliability assessment of the pilot feeder was conducted considering automation devices in the current positions as provided in system diagram illustrated in Figure 3. The

automation devices were assumed to 100 % reliable such that when a fault occurs downstream the device will clear the fault first without disturbing the entire network. The system outage time (r_s) presumed to be 10 minutes (0.17 hours).

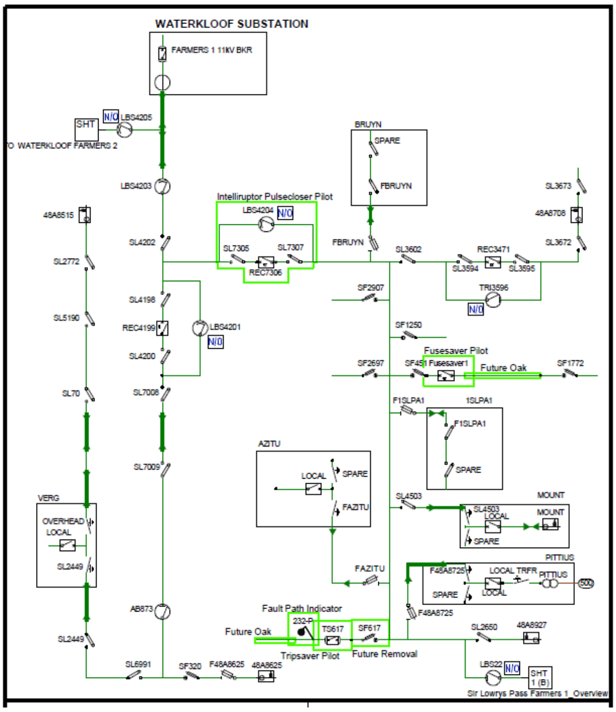

Figure 3: Waterkloof Farmers-1 11 kV Overview [14]

- **Scenario 3** - This scenario involves the application of Analytical and evolutionary Algorithm approaches to optimally place the automation devices along the Waterkloof Farmers 1 network. The main objective of finding the most suitable location of the devices is to improve the reliability of the network and minimize the customer interruption costs (CIC). To improve the reliability of the overall Waterkloof Farmers-1 distribution system, the FMEA technique was implemented using excel spreadsheets for analytical purposes. This is a brute-force approach which is a trial and error method in the sense that the automation devices are placed and shifted around in sections that are more susceptible to failures then the relevant indices (load point, energy and customer-oriented indices) were computed.

3. PROBLEM FORMULATION MATHEMATICALLY

The radial distribution pilot feeder is illustrated in figure 3 above. When a fault occurs along the feeder the automation device closest to the fault is expected to operate first and faulted section should be isolated without interrupting the main feeder. Basically, the objective function of optimal switch placement is minimizing the system costs which includes customer outage costs, investment and O&M costs of devices and to improve the reliability of the network (reducing SAIDI). The specific objective functions were the ECOST and SAIDI, given by equations (1)and (2) as [15]:

$$system\ ECOST = \sum_{i=1}^{nL} \sum_{j=1}^{nj} \sum_{k=1}^{nk} L_{ik}.C_{ij}(r_j).\lambda_j \qquad (1)$$

$$SAIDI = \sum_{j=1}^{nj} \sum_{k=1}^{nk} \lambda_j.(r_j)\, N_i \ / \ \sum_{l=1}^{nL} N_i \qquad (2)$$

Where:

n_k: Number of load points that are isolated due to a contingency j

L_{ik}: Load at load point k for the ith step of load duration curve at load point k

r_j: Effect of outage time of contingency j for load point k

λ_j: Average failure rate of contingency j

C_{ij}: Outage cost of customer class k due to contingency j with an outage duration of r_j

n_L: Number of load duration curve steps

n_j: Number of contingency in distribution system

N_i: Number of customers on feeder i

The optimisation of the system can be described using general objective function, given by equation (3) and (4) being the total cost and SAIDI respectively:

$$min.\sum_{i=1}^{nL} \sum_{j=1}^{nj} \sum_{k=1}^{nk} L_{ik}.C_{ij}(r_j).\lambda_j + \sum installationCost + \sum MaintenanceCost = \min.Total\ Costs \qquad (3)$$

$$min.(\sum_{j=1}^{nj} \sum_{k=1}^{nk} \lambda_j.(r_j)\, N_i \ / \ \sum_{l=1}^{nL} N_i) = \min.SAIDI \qquad (4)$$

The Voltage magnitude at each node must be maintained within limits and current at each line restricted by capacity ratings. These are the optimization constraints.

The proposed MATLAB GA algorithm prompts the user to select the objective function to minimize, then the switching devices will be placed to suit that function. The GA algorithm is based on the flowchart shown in figure 4.

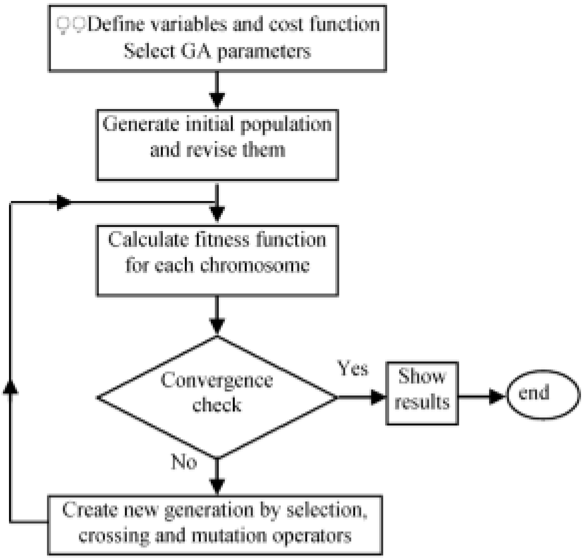

Figure 4: Genetic Algorithm Flowchart [15]

4. RESULTS

This part begins with illustrating the results of the cases analysed in feeder 3 of bus6 of the RBTS where five cases were considered, and the real system scenarios' outcome is compared and analysed.

4.1 Reliability Cost/Worth Assessment F3 RBTS Cases

The load point indices computed through FMEA and Monte Carlo Simulation (MCS) in MATLAB for the base case are shown in Table 2 and Figure 5 below where, A-Analytical and S-Simulation. The MCS algorithm took about 551.716421 seconds.

Table 2: Comparison of Load Point Indices

Load points	Failure rate (A)	Failure rate (S)	Outage time (A)	Outage time (S)	Unavilalabilty (A)	Unavilalabilty (S)
14	0.2485	0.2483	14.497	15.106	3.6025	3.7591
15	0.2433	0.2881	3.5324	2.8991	0.8593	0.8381
16	0.2465	0.2881	4.1846	3.4806	1.0315	1.0062
17	0.2485	0.2482	16.7465	17.2955	4.1615	4.3027

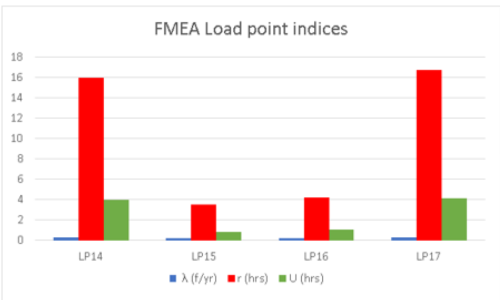

Figure 5: Load Point Indices Graph

The system performance indices calculated analytical and with MCS in MATLAB are shown in table 3 for the test network (base case) where 3 switches were installed. It can be observed from Table 2 and Table 3 that analytical and simulation approaches are very much comparable.

Table 3: Comparison of System Indices Base case

Reliabilty Indices	Analytical (A)	Simulation (S)	% Difference
SAIFI (Int./Cus.yr)	0.2482	0.2519	1.50
SAIDI (hrs/Cus.yr)	3.6150	3.7483	3.69
CAIDI (hrs/Cus.Int)	14.5667	14.8528	1.96
ASAI	0.99959	0.9996	0.00
ASUI	0.00041	0.0004	-3.07
ENS (MWh/yr)	5.9866	6.0685	1.37
AENS (kWh/Cus.yr)	272.1178	275.8	1.35
ECOST (k$/yr)	59.9465	58.7529	-1.99
IAER ($/kWh)	38.4340	35.7288	-7.04

Reliability worst/cost indices evaluation results for the five cases is shown in table 4 below;

Table 4: System Indices for the 5 Cases- F3 RBTS

Case	SAIFI	SAIDI	CAIDI	ENS (MWh/yr)	ECOST (k$/yr)	Total switch cost ($)	No. of switches	Locations
base case	0.2482	3.615	14.56674	5.9866	59.9465	9000	3	29,31,33
Case 1	0.2482	3.6399	14.66674	6.7381	69.65532	3000	1	29
Case2	0.2482	3.7184	14.98342	6.2603	63.48319	3000	1	31
Case 3	0.2482	3.7876	15.26201	6.4134	65.46015	3000	1	33
Worst case	0.2482	3.8939	15.6906	7.0007	73.04828	0	0	0

Table 4 illustrates that the best SAIDI does not translate to minimum ECOST when one considers case 1 to case3. The ranking of the cases based on SAIDI and ECOST are demonstrated in Table 5. The total switch costs depicted in Table 4 was based on the assumption that each manually operated switching device costs around $3000 [7]. The outcome demonstrated in these tables proved that both analytical and MCS techniques are very much comparable, which denotes that both approaches can be used to evaluate the reliability of a distribution system. The percentage differences between analytical and simulation approaches shown in table 3 are quite insignificant since they are very small and can be ignored.

Table 5: Cases Ranked in terms of SAIDI and ECOST F3 RBTS

Rank	SAIDI	ECOST
1	Base case	base case
2	Case 1	Case 2
3	Case 2	Case 3
4	Case 3	Case 1
5	Worst case	Worst case

4.2 Waterkloof Farmers-1 11kV Network Results

The reliability assessment of the pilot distribution feeder was conducted for three scenarios as discussed in the previous chapter (section 4.4). Table 7 and Figure 6 underneath recapitulates the system indices for the three different scenarios using the reliability-network-equivalent-approach.

Table 7: Three scenarios system indices

	SAIFI	SAIDI	CAIDI	ASAI	ASUI	ENS	AENS
Scenario 1	4.7741	23.8168	4.9888	0.9973	0.0027	291.5169	3389.7309
Scenario 2	4.7741	10.1658	2.1294	0.9988	0.0012	95.5394	1110.9236
Scenario 3	4.7741	7.7423	1.6217	0.9991	0.0009	70.5418	820.2533

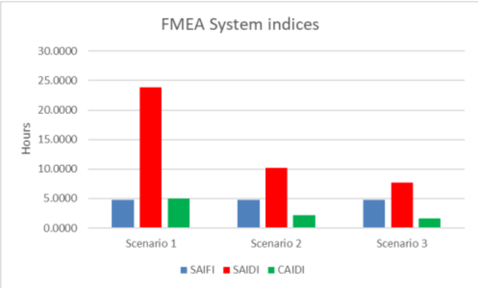

Figure 6: Real System indices for three Scenarios

Results of Customer Interruption Costs

The SAIDI and Customer Interruption Costs for the three cases are demonstrated in figure 7 and figure 8 below and in the next page respectively.

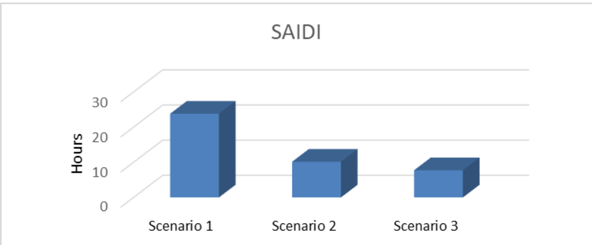

Figure 7: SAIDI for three scenarios

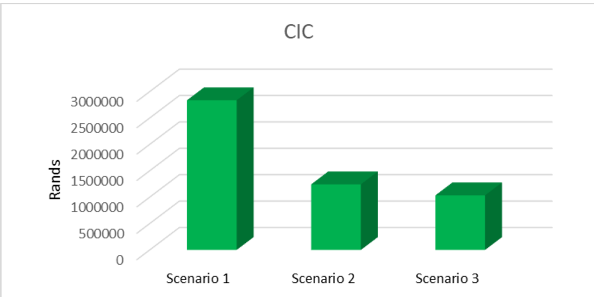

Figure 8: Customer interruption Costs for Three Scenarios

5. CONCLUSIONS

Automation devices play an essential role in the reliability of distribution networks. In this report predictive analytical and simulation (MCS) approaches for reliability assessments of a test system and the Waterkloof Farmers-1 feeder are presented. From the results obtained through the analytical processes and MATLAB simulation codes were very much similar which validated the hypothesis studied and discussed in the literature review. The reliability-network-equivalent-approach method proved to be superior over the conventional FMEA since the lengthy arithmetic processes could be easily made easier hence reducing the probability of being prone to errors. Selecting the adequate and suitable location of sectionalizing switches is a very intricate task faced by distribution system engineers and researchers are working around the clock to find a long-lasting solution.

6. REFERENCES

[1] R. Billinton and S. Jonnavithula, "Optimal switching device placement in radial distribution systems," *IEEE Trans. Power Deliv.*, vol. 11, no. 3, pp. 1646–1651, 1996.

[2] A. Abiri-Jahromi, M. Fotuhi-Firuzabad, M. Parvania, and M. Mosleh, "Optimized sectionalizing switch placement strategy in distribution systems," *IEEE Trans. Power Deliv.*, vol. 27, no. 1, pp. 362–370, 2012.

[3] O. Shavuka, K. O. Awodele, S. P. Chowdhury, and S. Chowdhury, "Application of Predictive Reliability Analysis Techniques in Distribution Networks," *UPEC2010*, pp. 3–8, 2010.

[4] R. E. Brown, *Electric Power Distribution Reliability*, 2nd ed. Raleigh, North Carolina: CRC Press 2009.

[5] O. K. P. Mokoka and K. O. Awodele, "Reliability evaluation of distribution networks using NEPLAN & DIgSILENT power factory," *IEEE AFRICON Conf.*, pp. 1–5, 2013.

[6] J. H. Teng and C. N. Lu, "Feeder-switch relocation for customer interruption cost minimization," *IEEE Trans. Power Deliv.*, vol. 17, no. 1, pp. 254–259, 2002.

[7] M. Lixin, L. Xinhui, W. Shouzheng, and M. Hiromi, "Optimal Switch Placement in Distribution Networks under Different Conditions Using Improved GA," 2010 Second International Conference on Computational Intelligence and Natural Computing (CINC), no. 1, pp. 236–239, 2010.

[8] D. Groot, R. Joannes, and W. De Groot, *Optimal placement and operation of novel grid technologies in distribution grids Optimal placement and operation of novel grid technologies in distribution grids*. 2017.

[9] S. Ray, S. Bhattacharjee, and A. Bhattacharya, "Optimal allocation of remote control switches in radial distribution network for reliability improvement," *Ain Shams Eng. J.*, 2016.

[10] M. S. Stojanovic, D. S. Tasic, and A. T. Ristic, "Optimal allocation of distribution automation

devices in medium voltage network," *Elektron. is Elektrotechnika*, vol. 19, no. 4, pp. 9–14, 2013.

[11] R. Billinton, "A test system for teaching overall power system reliability assessment," *IEEE Trans. Power Syst.*, vol. 11, no. 4, pp. 1670–1676, 1996.

[12] R. N. Allan, R. Billinton, I. Sjarielf, L. Goel, and K. S. So, "A RELIABILITY TEST SYSTEM FOR EDUCATIONAL PURPOSES - BASIC DISTRIBUTION SYSTEM DATA AND RESULTS," IEE Transactions on Power Systems, Vo1.6, no. 2, pp. 813–820, 1991.

[13] R. Billinton and P. Wang, "Reliability-network-equivalent approach to distribution -system - reliability evaluation," IEE Proc.-Cener. Transm. Distrih., vol. 145, no. 2, pp. 149–153, 1998.

[14] Z. Khan, "Improving the reliability performance of medium voltage networks," 2013.

[15] J. N. Ahour, M. Rostami, V. T. Majd, M. Rashidbeygi, and H. Moazen, "Optimal switch placement with revised genetic algorithm in distribution system," *21st Electr. Power Distrib. Netw. Conf. EPDC 2016*, no. May, pp. 54–59, 2016.

The HEPSSA Project – A Catalyst for Capacity Building at Durban University of Technology

Innocent Davidson
Dept of Electrical Power Enginering
Durban University of Technology
Durban, South Africa
innocentD@dut.ac.za

***Abstract*—The Higher Education Partnerships in Sub Saharan Africa project is funded by the British Royal Academy of Engineering, and runs for 2 years from April 2017 to March 2019. It is a network of engineering faculties and schools in some Eastern and Southern African universities linked to a UK university with the aim of enhancing quality of engineering education and training. The project objective is to enhance the quality of engineering education and training through: academic staff secondment to industry; invitation of industry experts to university as guest lecturers; collaborative research with industry, industry supported curriculum review and knowledge sharing workshops. This paper presents the activities at Durban University of Technology and our efforts to enhance engineering training of technical staff through short-term industry internships and postgraduate studies. The goal is to produce graduate engineers and technicians: who possesses relevant skills, meet the expectations of modern industry and engineering professional bodies; graduates who are employable nationally and regionally. It is also expected to produce academic staff with enhanced practical experience and better teaching skills, which will enrich the relevant engineering curriculum at universities.**

Keywords*—*HEPSSA, RAEng, UoN, UNAM, DUT, AAU, Cambridge University, engineering education.

I. Background and Project Focus

The Higher Education Partnerships in Sub Saharan Africa (HEPSSA) project establishes academia-industry partner-ships between University of Namibia (UNAM) Faculty of Engineering & Information Technology (Hub University) with the University of Cambridge (UK Partner), as well as three other universities, namely Addis Ababa University (AAU), Ethiopia, University of Nairobi (UoN), Kenya and Durban University of Technology (DUT), South Africa (the Spoke Universities), together with some selected local industries. The objective is to enhance the quality of engineering education and training through joint research, staff secondment to industry, industry-initiated research and secondment of industrial experts to universities. This is to enable participating universities to produce versatile, well-informed and marketable graduate engineers who meet the expectations of modern industry and professional bodies and are employable nationally and regionally.

The Hub University and Spoke Universities second their staff members to selected local industry during vacation time and invite industry experts to the universities to share their experiences through Guest Lectures and contribute to the development of new or existing engineering curricula. In the case of Durban University of Technology, two firms, and Eskom (South Africa's Electric Utility) participated in the project. Professional Development and Knowledge Sharing Workshops were held by the Hub University to ensure that participating universities and industry have a forum to present their experiences and share information relating to research and practical experience. The selection of suitable Industrial Partners is necessary to ensure that industry-initiated research is undertaken with financial support from the industry. Where an MSc or PhD student is identified for such research project the UK Partner will endeavour to identify suitable co-supervisors. The UK Partner has considerable experience in academia-industry collaboration and share experiences with the participating universities based on the success of University Technology Centres (UTC) in the UK. Joint Research activities in the development of superalloys will be undertaken between University of Cambridge and UNAM. It is envisaged that Spoke universities will identify research topics that could jointly be undertaken within this network.

II. Activities at DUT

The activities undertaken at Durban University of Technology include the following:

- Deployment of Staff to Industry.
- Industry Participation.
- DUT Collaborative Research
- Invited Industry Guest Lectures
- MOU between UNAM and DUT

A. Deployment of Staff to Industry

A fulltime academic staff, two fulltime technical staff, and two postgraduate students participated in this program. Four of these were studying towards the MEng degree. The last candidate is a postgrad student studying towards the Doctor of Engineering degree program. In addition to acquiring valuable engineering and technical experience, staff members also used this avenue to acquire relevant experience towards professional registration with the Engineering Council of South Africa (ECSA), working under registered professionals.

The following industries served as partners for DUT staff secondment and postgrad student industrial placement:

- Global Armatures Pty Ltd (South Africa) – traction motors – electrical machines
- Solaray System (Pty) Ltd
- Eskom - through its Tertiary Education Support Program (TESP) supported financially projects in smart micro-grids and energy storage systems

978-1-7281-0368-6/19/$31.00 ©2019 IEEE

Fig. 1: Global Armatures – Traction motor repairs

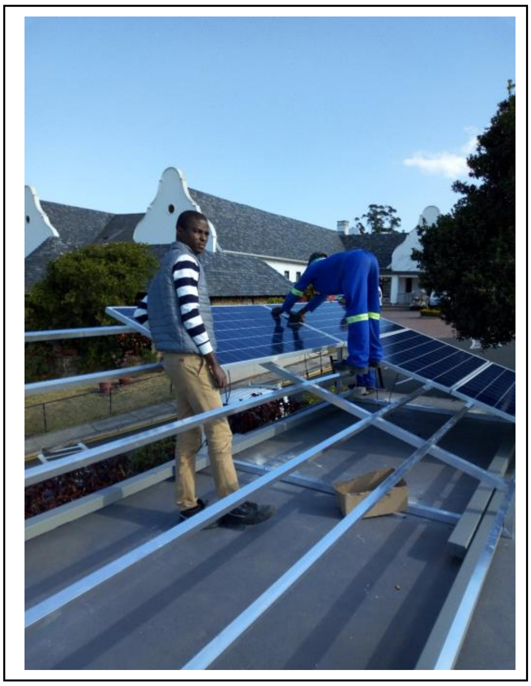

Fig. 2: Solary Systems providing turnkey Solar PV and Solar Thermal Installations for commercial and industrial clients

B. *Collaborative Research Projects*

The following research projects are on progress:

- “Evaluation of grid-scale battery energy storage system as an enabler for large-scale renewable energy integration”. This activity is undertaken in collaboration with Eskom Smart Grids towards a MEng degree.
- “Modelling and performance analysis of a universal motor fed from a renewable energy Nano-Grid”. This activity shares infrastructure in load modelling, solar-PV, energy storage and undertaken towards a MEng degree.
- “Performance analysis of singe-phase induction motor fed from a photovoltaic renewable energy System.” This activity also shares infrastructure with grid-tied inverter for reactive power support. It is also undertaken towards a MEng degree.
- “Development of a multi-level converter-based D-STATCOM / Battery energy storage system (BESS) for power quality enhancement in high RES penetrated microgrid”. This project is been undertaken towards a DEng degree.

III. MOU Between UNAM and DUT

To facilitate inter-varsity collaboration and staff/student exchange, a memorandum of understanding (MOU) has been established between the University of Namibia and Durban University of Technology. This MOU also encompasses all partner universities under this HEPPSSA project. Through this project/MOU, UNAM will support DUT academics and technical staff to attend a Knowledge Sharing Workshop in Namibia in March 2019.

IV. MOU and Collaborative Research

The critical collaborative research project is: Energy Systems for Smart and Intelligent Cities. The research focus is undertaken with partner universities under the following sub-themes and areas:

A. *Smart Grids - modernization of electrical power systems*

- Smart grid design and engineering
- Smart micro-grid modelling and simulation.
- Electrical grids merging bi-directional power flow with information flow to monitor changes in usage and supply electricity.
- Utilizing digital communications technology to detect and react to the usage of the electrical supply and integration into the power grid.
- Smart grids are also 'self-healing' and can repair faults and reduce outages, since they can detect fluctuations and disturbances to the grid and isolate parts of it.
- Technical and non-technical loss minimization in delivery systems.

B. *Smart Cities Infrastructure and Innovation*

- Smart materials and nanotechnology.
- Innovative new infrastructure: electric vehicles, battery electric vehicle, ?plug-in electric vehicle, hybrid electric vehicle, charging stations for electric cars.
- Smart transportation systems, vehicle-to-grid (V2G) infrastructure, energy-saving & green IoT applications; home- and industry automation.
- Energy storage and utilization in Cities: UGHPS schemes, district energy systems; electrical/thermal energy, energy sustainability/conservation and recapture, mitigating GHG emissions, carbon neutrality, grid energy storage.

C. *Smart Buildings*

- Smart building materials.
- Design of integrated & autonomous energy systems for buildings.

- Hybrid & integrated energy systems: micro-turbines, co-generation.
- Advance solar PV materials, solar PV energy systems, fuel cells.

D. Smart Health Care and Smart Water

- DC electroporation - non-contact delivery of medicine using DC power.
- Smart water systems design and analysis.

E. Smart Education and Smart Technologies

- Super-learning and innovative teaching technologies.
- DC renewable energy to consumer homes and businesses.
- Generating RE in DC: renewable IPP generators; LV-DC grids.
- Technical loss minimization to achieve substantial savings in decreasing voltage transformations achieved by direct DC generation.

F. Smart Business Enterprises/Entrepreneurship

V. Some Results

Over the period of this research project, the following have been achieved at DUT as a Spokes University in the Higher Education Partnerships in Sub Saharan Africa project funded by the British Royal Academy of Engineering,:

- Graduated 3 PhDs & 3 MSc students in Electrical Engineering in 2018.
- Published 8 accredited journal papers [1], [2], [3], [4], [5], [6], [7], [8] and 11 peer-reviewed conference proceedings.
- Research funding from Royal Academy of Engineering, UK. (2017-2019)
- More staff registered with the Engineering Council of South Africa.

Other partner universities have utilized this opportunity to advance other areas of their academic programs and professional development. For example, the University of Nairobi, College of Architecture and Engineering, School of Engineering, Department of Mechanical and Manufacturing Engineering, developed new "Regulations and Syllabus for the Degree of Doctor of Philosophy (PhD) in Mechanical Engineering, supported with course work.

The Department of Mechanical and Manufacturing Engineering has been offering the PhD degree by thesis only after research since the 1970's. However, in 2014, the Commission for University Education (CUE) issued fresh guidelines that required all PhD programs to have coursework content consisting at most one third of the total content. It is this requirement that has necessitated the development of this new program with a Stakeholder's workshop sponsored by the Royal Academy of Engineering Grant.

University of Namibia had several lecturers in Mining Engineering and Metallurgical Engineering undertake short-term internships at Navachab Gold Mine, Namport, Nam-Water and Namibia Tantalite.

At Addis Ababa University as a Spokes University, the focus is Technology Transfer, Entrepreneurial Development and Commercialization of Research Outputs through the University Business Incubation Centre. The University-Industry Linkage and Technology Transfer Office of Addis Ababa University is trying to solve the industry problems through: Industry-sponsored (contract) research, consultancy, patent licensing, student internship, technology business incubation, and University-industry cooperative research. A newly developed technology created by AAU Researchers regarding the removal of fluoride from drinking water using natural zeolites is the first case of a technology transferred to a company currently in process.

Acknowledgment

The author acknowledges the financial support of the Royal Academy of Engineering, UK and Eskom TESP. The author also acknowledges the following experts from partner universities, namely: Professor Catherine Rae, Coordinator, University of Cambridge; Professor George Rading, Coordinator, UoN; Professor Frank Kavishe, Coordinator, UNAM; Dr. Kabede, Coordinator, University of Addis Ababa; and our partner industries in Namibia, Kenya and South Africa, namely: Solary Systems (PTY) Ltd, Global Armatures (PTY) Ltd, for their technical contributions.

References

[1] E Buraimoh, F. K. Ariyo, M. O. Omoigui ad I.E. Davidson, "Investigation of Combined SVC and TCSC versus IPFC in Enhancing Power System Static Security", Paper accepted or publication in the *International Journal of Engineering Research in Africa*, 2018.

[2] P. T Ogunboyo, R. Tiako, I. E. Davidson, "Effectiveness of Dynamic Voltage Restorer for Unbalanced Voltage Mitigation and Voltage Profile Improvement in Secondary Distribution System," in *Canadian Journal of Electrical and Computer Engineering*, vol.42, no. 2, pp. 105-115, Spring 2018. doi: 10.1109/CJECE.2018.2858841.

[3] C. G. Monyei, S. Viriri, A. O. Adewumi, I. E. Davidson and D. Akinyele, "A Smart Grid Framework for Optimally Integrating Supply-side, Demand-side and Transmission Line Management Systems". *Energies 2018, 11, 1038; doi:10.3390/en11051038*.

[4] P. T. Ogunboyo, R. Tiako, I.E Davidson, "Investigation of Voltage Unbalance Profile in Low Voltage Electrical Distribution Network with Normal Mode Operation Using MATLAB", *International Journal of Engineering Research in Africa*, Vol. 35, pp. 60-76, 2018.

[5] Dayahalen Chetty, Mobolaji Bello and Innocent E Davidson, "Performance Evaluation of Traction and Utility Network Interface: Fault Location and Protection Coordination". *Electric Power Systems Research Journal*., Vol 156, pp.44-53, 2018.

[6] P. T Ogunboyo, R. Tiako, I. E. Davidson, "Voltage Unbalance Mitigation and Voltage Profile Enhancement in Secondary Distribution System Using Dynamic Voltage Restorer", *International Journal of Engineering Research in Africa*, Vol. 34, pp. 88-101, 2018.

[7] P. T Ogunboyo, R. Tiako, I.E Davidson, "Application of Dynamic Voltage Restorer for Power Quality Improvement in Low Voltage Electrical Power Distribution Network: An Overview", *International Journal of Engineering Research in Africa*, Vol. 28, pp. 142-156, 2017.

[8] Ester Hamatwi, Innocent Davidson and Michael Gitau, "Rotor Speed Control of a Direct-driven Permanent Magnet Synchronous Generator-based Wind Turbine using Phase-lag Compensators to Optimize Wind-Power Extraction", *Journal of Control Science and Engineering*, Vol. 2017, Article ID 6375680. https://doi.org/10.1155/2017/6375680.

Artisan Development and Training - An analysis of the Apprentice, Learnership and ARPL Trade Test Results of Candidates Tested at TEK-MATION Training Institute

Therasinamurthie P. Govender
DaVinci Institute
Modderfontein
Lethabong, 1609, South Africa
DaveG@tekmation.co.za

Innocent E. Davidson
Dept. of Electrical Power Engineering
Durban University fo Technology
Durban, 4000, South Africa
innocentD@dut.ac.za

***Abstract*—The artisan work force is the lifeblood of the engineering and technology sectors and is the key factor in driving the economic growth and development of any country. Presently South Africa is experiencing a shortage of skilled artisans who can maintain the various state-owned entities (SOE's) and other processing and manufacturing plants in the industrial sectors. In the last 20 years different initiatives and interventions have being put in place by government in order to overcome the shortage of scare and critical skills [17]. The purpose of this paper is to present the artisan training and development model practiced at TEK-MATION Training Institute and to share the best practices and shortcomings of the model.**

Keywords—component, formatting, style, styling, insert (**key words**)

I. Background to the Problem of Skills Training and Development

The shortage of skilled artisans in South Africa is a major problem directly affecting artisan training and development. The previous government had a good artisan training and development system in place for the training and development of a skilled blue collar workforce [10]. Parastatals such as TELKOM, ISCOR, ESKOM, SASOL, SAR&H, the mining industry and the armed forces played an important role in providing the post 1994 Republic of South Africa with the relevant technical and practical skills needs in engineering [21]. One of the hallmarks of this era was that each of these entities each had a fully equipped and

resourced training centre.

The period of indenture varied from 2 to 4 years depending on the related trade. The apprentice was required to attend a technical college and obtain at least a National Technical Certificate (NTC) at the NTC 2 level with four related trade subjects. The NTC 2 with four subjects was considered the minimum requirements for an apprentice to attempt a trade test assessment at the Central Organisation for Trade Testing (COTT) situated at Olifantsfontein, Gauteng. The technical colleges were geared up for a three block–release program. An apprentice could successfully complete The NTC 1, 2 and 3 at the end of a three year training program. He or she had to complete 96 weeks of practical on the job training under the guidance of a qualified artisan. Once all the pre –requisites were fulfilled then only would the apprentice be allowed to attempt a trade test at the Central Organisation Trade Testing (COTT) situated at Olifantsfontein, Gauteng. [17]

of practical on the job training under the guidance of a qualified artisan. Once all the pre –requisites were fulfilled then only would the apprentice be allowed to attempt a trade test at COTT [17].

The socioeconomic policies under the era heavily benefited the privileged white apprentices. Non-white apprentice indenture only started in the mid to late 1970's. Training and indenture of Apprentices completely stopped in the late 1980's, this was due to socio-economic challenges faced by the government and the parastatals involved in training [21]. Training and Development was deemed not

Artisan Development	***Apprentice Training Programme***
Inducted Apprentice	***Duration**: 2-4 years* ***Min Pre-requisite**:* *Age – 15 years.* ***Academic**: Std. 7.* *Depending on the requirements of industry per trade*
Workplace Practical	*96 weeks*
Technical College	*Three Semester- 3 Months each*
Trade Test	*2 days*

Figure. 1. Apprentice Training Programme (Manpower Training Act, 1981)

core to the business and was seen to be an expense to the company and because of that reason the mining industry was battling with skills crisis [24].

II. Outcome of the Research

An integrated learning system that will contribute to enhancing the skills sets in artisan training and development in South Africa.

- Re-establishing a relevant, current and suitable curriculum content that can be a pragmatic approach to the present and the future artisan training and development;
- To create advanced training programmes for technician training; and

978-1-7281-0368-6/19/$31.00 ©2019 IEEE

- To adhere to the quality assurance and policy of the Quality Council for Trades and Occupations (QCTO) in relation to skills development and trade assessments.

This study addresses current artisan learning programmes interventions at TEK-MATION Training Institution.

A. Institutional Component

These include:

(i.) Skill programmes

(ii.) Unit standard based programmes;

(iii.) Qualifications in Learnerships programmes; and

(iv.) Artisan programmes incorporating phase training modules for apprentice.

B. Practical Component

These include:

(i.) Structured task-based learning.

(ii.) Practical training integrated with the theory of the trade.

(iii.) Tasks practised on industry specified equipment.

(iv.) Compilation of a Portfolio of Evidence (PoE) of learning outcomes.

III. Factors Impacting on Artisan Development in South Africa Prior to 1994

These factors include:

(i.) Started in the mid 1950's and stopped in 1980. The training and indenturing of apprentices stopped in 1980.

(ii.) The Apprentice system was developed primarily for the upliftment of the white populace. Indians and Colored apprentices were indentured by companies in the late 1970's.

(iii.) Inequality in the different education systems leading up to secondary schooling.

(iv.) Inadequately developed secondary school curricula;

(v.) Underqualified teachers;

(vi.) Experienced teachers leaving the schooling system when severance packages were offered;

(vii.) Under resourced school laboratories; and

(viii.) The introduction of Mathematic Literacy.

A. Evolution of present Artisan development system

The genesis of the current system is as follows:

(a.) Introduction of the Sector Education Training Authorities (SETA's);

(b.) Introduction of South African Qualification Authority (SAQA) National Qualification Framework (NQF) based on learnerships in 1994;

(c.) Qualification curriculums were developed by the relevant SETA's by tapping into the knowledge and experience of Subject Matter Experts (SME's). The SME's were sourced from a wide range of different industrial role players related to a specific discipline of occupation. The selected SME's were then registered at the SETA as a Standards Generating Body (SGB).

(d.) The Qualifications ranged from NQF 1 to NQF 4. It consisted of three components i.e. Core, Elective and Fundamentals with a total credit value of approximately 120 credits per qualification.

(e.) Structured learning programs for the various industry and manufacturing sectors were introduced. The program.

(f.) Introduction of a unit standard based skills programmes culminating in a certificate and credits on the National Learner Records Database (NLRD);

(g.) National Skills Development Strategy (NSDS 1), NSDS 2 , NSDS3 and the eventually the National Skills Development Plan (NSDP) up to year 2030;

(h.) The reintroduced of the Apprentice Artisan Development programme in 2008;

(i.) SETA approved Skills Development Providers;

(j.) SETA approved Decentralized Trade Test Centre (DTTC);

(k.) The implementation of the Workplace Skills Plan (WSP) for employee training.

B. Problem areas identified in the NQF Learnership programmes

- The Learnerships were not fully accepted and understood by industry;
- Qualified learners had no job title;

  There was no trade test certificate; there was no nationally recognised trade test certificate i.e. Red Seal as under the Manpower Training;

- Learner were treated as an unqualified artisan by industry;
- Training gaps between the Learnership qualifications and Apprenticeship trade qualifications were evident;
- The trade qualifications developed by the various Standards Generating Bodies (SGB's) of the specific Seta and were sector specific; and
- An ineffective Quality Assurance system enforcement by some SETA's.

The technical colleges operated on a trimester program of three months each that allowed for successful apprentices to complete and NTC 3 at the end of a three year training program. He or she had to complete 96 weeks of practical on the job training under the guidance of a qualified artisan. Once all the pre –requisites were fulfilled then only would the apprentice be allowed to attempt a trade test at COTT [17].

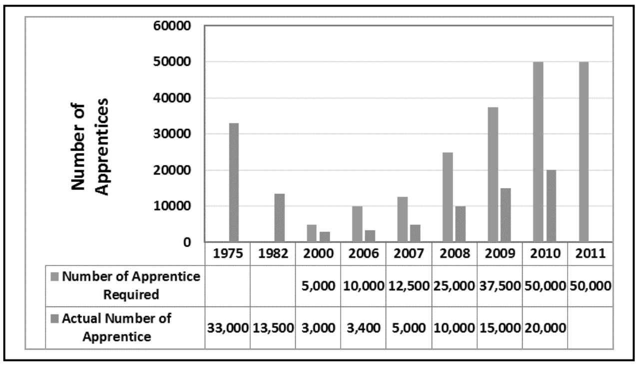

	1975	1982	2000	2006	2007	2008	2009	2010	2011
Number of Apprentice Required			5,000	10,000	12,500	25,000	37,500	50,000	50,000
Actual Number of Apprentice	33,000	13,500	3,000	3,400	5,000	10,000	15,000	20,000	

Figure 2. Shortage of Technical Skills in South Africa (Sandvik, 2012)

The statistics in Figure 2 shows that the actual number of Apprentices enrolled in SA from the year 2000-2010 were not meeting the demand of the labour market.

Based on the 2008 National Scarce Skills, there was a 9% increase from the previous year. In the year 2008 the skills deficit in South Africa was regarded as a national. South Africa had only 10% of the artisans that it had 20 years ago, the country had a 40% shortage of artisans [21].

International trends also suggest that skills shortage is a cause for serious concern globally. LaRocque [12] states that the issues of skills shortage in New Zealand have been at the forefront of discussion in the business sector, national press and in government policy for some time now. Like New Zealand, Australia also suffers from a severe shortage of skilled labour [14].

Breier and Erasmus [1] blame the massive shortage of artisans largely on a decline in apprenticeship systems and the failure of substitute interventions, which include training via learnerships and further education and training colleges to eliminate the backlog.

Artisan development was mainly hindered by the decline of apprenticeship systems and lack of interventions from the providers of education and training [15]. Most learners attained qualifications in the engineering field but they remain unemployed because they lack the sufficient and necessary skills required in the industry [12].

Meyer and Botha [15] believed that the current problem relating to skills development in the industry can be summarised as follows:

- There is a high level of unskilled workers who lack the basic skills needed for meaningful employment. Most skill occupations have a significant proportion of workers who do not any form of formal qualifications.
- Productivity levels are low as a result of poor or inadequate training due to low levels of training investment in training workers. There is a need for all skills training to be developed continually to meet the skill requirements in the workplace arising from new technologies [9].
- While apprenticeships are a major source of skills in the traditional skilled trades, there has been an increase in other pathways involving vocational education outside of the apprenticeship system.

C. *Economic Implications of Skills Shortage*

It is clear that the development of the economy and the creation of wealth is greatly affected by the supply of skills in South Africa and it is crucial for the country to have sufficient artisans to fill that gap [16].

Various studies and researchers have come to the conclusion that skills shortages in South Africa are one of the main reasons the economic is unstable. According to the World Economic Forum [11], skills development has been recognised as a key component of South Africa's transformation and economic growth. It affects the level of economic productivity and reduces the country's capacity to develop a knowledgeable society. This, in turn, affects the country's functioning in the global economy [7].

Despite the fact that it is crucial to have sufficient artisans in South Africa to enable infrastructure development, economic growth and wealth creation, many studies, [3]; continue to show evidence that the country faces a severe shortage of artisans. This hinders the government's ability to sustain the kind of development and economic growth that is needed for the eradication of [25.

IV. TEK-MATION TRAINING INSTITUTE APPROACHES, PROGRAMMES AND TRAINING SYSTEMS

TEK-MATION (PTY) Ltd t/a TEK-MATION Training Intuition was established in the year 2002 as a provider of engineering training and skills development. The Institution is a multi-SETA accredited organisation and is also provisionally registered as a private Technical Vocational Education and Training College. (TVETC).

TEK-MATION Training Institute has fully operational and functional technical training workshops in the Electrical, Instrumentation, Welding and Mechanical trades. The institution offers various programmes, however, this research is limited to Learnerships, Apprenticeships and the Artisan Recognition of Prior Learning (ARPL) programme.

The Institute is accredited and registered with the Quality Council for Trades and Occupations (QCTO), Department of Higher Education and Training (DHET), UMALUSI and the various SETA's. The following six engineering trades:

- Instruments
- Fitting and Turning
- Fitting
- Welding
- Refrigeration and Air-conditioning
- Electrical

V. The Tek-Mation Training Intervention

A sample population of 40 learners were selected for this study at TEK-MATION Training The trade test results for the selected sample was analysed and presented below. The selected sample was made up of 16 Apprentices, 16 Learnerships and 8 ARPL learners.

A. Interventions for the ARPL Program at TEKMATION

These include:

- Portfolio of Evidence (POE)
- Pre-assessment with theory and practical component
- Evaluation
- Training intervention
  - Upskill
  - Reskill
  - Integrate Theory and Practice
  - Monitoring and Evaluation by facilitator of training
  - Schedule a training plan and adherence to it.
  - Retrain till competency is attained.

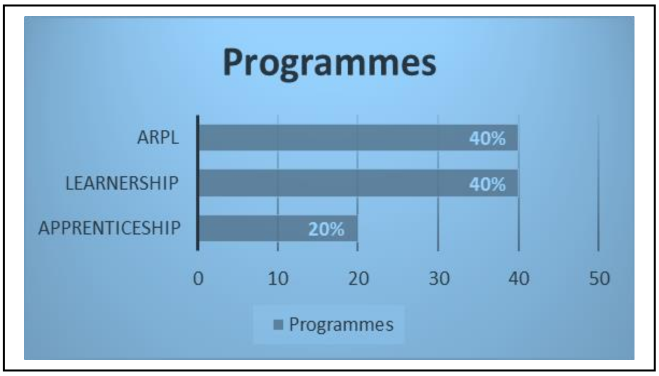

Figure 3. Distribution of sample population.

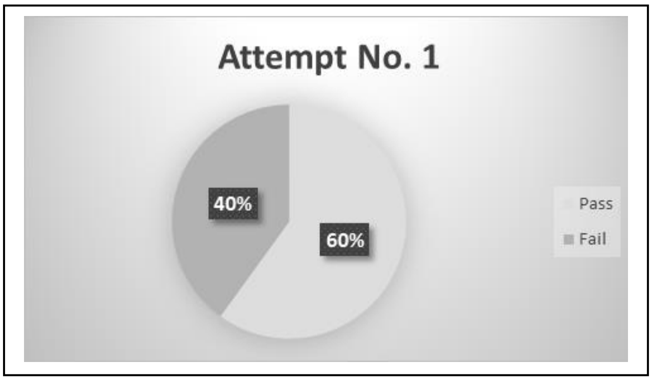

Figure 4. Learners passed or fail at first attempt.

Figure 4 shows the first attempted trade test and indicate that 60% of the learners under review passed and attained their trade test qualification during their first attempt. However, 40% of the learners failed and proceeded to their second

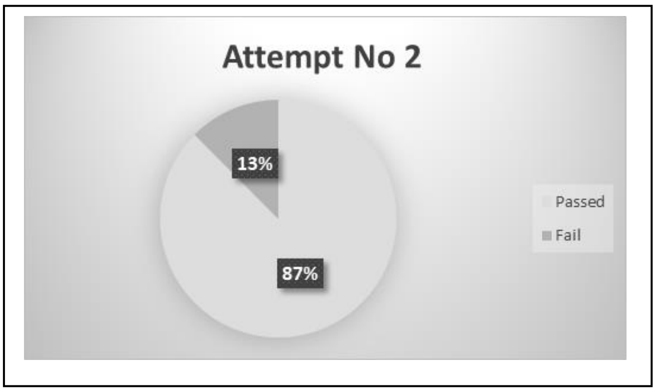

attempt.

Figure 5 Second Attempt Trade Test

Amongst the learners who failed and proceeded to second attempt, Fig. 5 reveals that 87% passed, whilst 13% failed.

B. Overall Analysis of the Trade Test Result

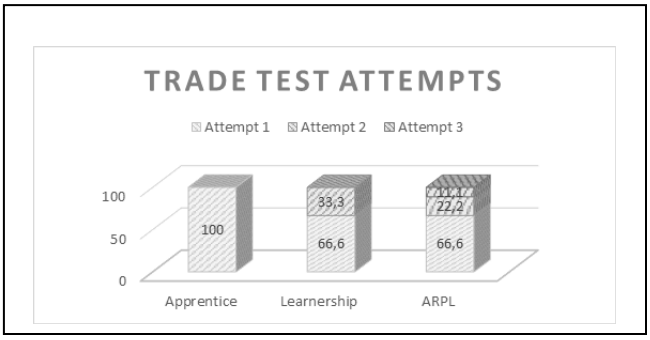

Figure 6 Overall Analysis of the Trade Test Result.

Fig. 6 shows that the majority of the learners passed and attained the trade test certificate at first attempt, despite being enrolled under different programmes. This is probably due to the fact that TEK-MATION has qualified facilitators who not only facilitates but mentors each learner who registers for the programme.

The theoretical and practical training is essential for students to be well equipped with knowledge as well as the necessary transferable skills required by the industry. The training provides students with both specific learning outcomes in each field of study and with the general skills that are required by all engineers, artisans and technicians in the industry. These outcomes are extremely specific and provide the students with the opportunity to practice and apply the fundamentals in an actual workplace.

VI. Skills Development Interventions

In 2013, South Africa's National Development Plan (NDP) stated that the country should produce more than 30 000 qualified artisans a year in order to meet its skilled labour demands [23]. In squaring up to this challenge, the government had identified Further Education and Training (FET) colleges as a key part of the solution [23].

VII. CONCLUSION

Skills shortage has been part of the skills development debate in South Africa for some time, and it is central to South Africa's socio-economic development. This paper has discussed the causes and economic implications of skills shortage in South Africa. In order to overcome this challenge, an educational integrated learning system that will contribute to enhancing the skills sets in artisan training and development in South Africa is required.

This paper concludes by presenting the artisan training, approaches, programmes and training practised at TEK-MATION Training Institute and shared the best practices and shortcomings of the model. This will no doubt improve the education system which is still trying to overcome neglect and dysfunction suffered under Apartheid. This can be done by equipping learners with the latest training methodology, technology and innovation to ensure that the training conforms to the highest and most demanding quality assurance standards.

REFERENCES

[1] Breier, M. and Erasmus, J. Skills Shortages in South Africa: Case Study of Key Professions. Cape Town: HSRC, South Africa, 2009.

[2] Breier, M., The Shortage of Medical Doctors in South Africa. Case Study Forming Part of the HSRC Study: A Multiple Identification and Verification of Scarce and Critical Skills in the South African Labour Market. Cape Town: HSRC, South Africa, 2007.

[3] Centre for Development and Enterprise, The Skills Revolution: Are we Making Progress? Pretoria: CDE, 2007

[4] Department of Public Works, Skills for Infrastructure Delivery in South Africa: The Challenge of Restoring the Skills Pipeline. Pretoria: Department of Public Works, 2007.

[5] Du Toit, R. and Roodt, J., Engineering professionals: crucial key to development and growth in South Africa. Human Sciences Research Council, South Africa, Development Policy Research Unit (DPRU) University of Cape Town, Sociology of Work Unit, Research Consortium, 15(1), pp 20-30, 2008.

[6] Engineering Council of South Africa (ECSA), Annual report 2008–2009. Available from: www.ecsa.co.za/documents/080309n6_2006_2007_Annual_Report.pdf [Retrieved 14 July 2017].

[7] Glass, H. and Choy, W. K., Brain Drain or Brain Exchange? Treasury Working Papers 01/22, 2001.

[8] Auckland, G J. and Potvin, Y. , Technical Skills – a Major Strategic Issue. Journal of the Southern African Institute of Mining and Metallurgy, 108(1), pp.775-782, 2008.

[9] Van Rooyen, L.; du Toit, D. H., Botha, E., and Rothmann, S., Artisan Retention in an organisation in South Africa. SA Journal of Human Resource Management, 8(1), p 8., 2010.

[10] Hofmeyer, J., All you ever wanted to know about SETA, and were Afraid to ask. Cutting Edge, 3(1) pp7-14, 2000.

[11] Joint Initiative on Priority Skills Acquisition, Report on activities March to December 2006, 2007.

[12] Kruger, N., Forum, World Economic. South Africa has a Skills Shortage. How do we fix it? [Online], Available from: https://www.weforum.org/agenda/2016/05/south-africa-skills-shortage-how-do-we-fix-it/ Accessed 14 October 2016.

[13] LaRocque, N., Skill Development and Skill Shortages in New Zealand. New Zealand: Education Forum., 2007

[14] Manpower Training Act 56 of 1981., [Online] Available at: http://www.labour.gov.za/DOL/legislation/acts/skills-development/manpower-training-act-1981 [Accessed 11 November 2016]., 1981

[15] Mateus, A. D.; Allen-Ile, C. and Iwu, C. G., Skills Shortage in South Africa: Interrogating the Repertoire of Discussions. Mediterranean Journal of Social Sciences, 5(6) (April 2014), pp. 63-73, 2014.

[16] Meyer, M. and Botha, E., Organisation Development and Transformation in South Africa. 2nd Edition. LexisNexis Butterworths, 2004.

[17] Momberg, E., Brain Drain: We are in Denial. The Sunday Independent, 31 August 2008.

[18] Mining Qualifications Authority, Final Sector Skills Plan for the Mining and Minerals Sector. MQA, Johannesburg, 2012..

[19] Rasool, F.; Botha, C. J., and Bisschoff, C. A., Push and Pull Factors in Relation to Skills Shortages in South Africa. Journal of Social Sciences, 30(1), pp.11-20, 2012.

[20] Richardson, S., What is Skills Shortage? NCVER: Adelaide, Australia, 2007.

[21] Service Publication., Lack of Skills Hampers Service Delivery, Canada, 2010.

[22] Sandvik Mining. Market Area EMEA Project: Retention of Critical Skills. Doorsamy, J., Prinsloo, J., Salifu, N., Mubita, R., and Rweikza, D. (eds). Aug. 2012

[23] South African News Agency, SA faces critical artisan shortage. [Online] Available at: http://www.engineeringnews.co.za/article/sa-facescritical- artisan-shortage-2005-12-16 [Accessed 11 November 2016], 2013.

[24] South African News Agency, Summit Places Spotlight on Artisan Development [Online] Available at: http://www.sanews.gov.za/south-africa/summit-places-spotlight- artisan-development [Accessed 15 November 2016], 2014.

[25] Stacey, T.R. H; Adjig Eorg Iou, J., and Potvin, Y., Technical Skills – a Major Strategic Issue. Journal of the Southern African Institute of Mining and Metallurgy, 108(1), pp.775-782, 2008.

[26] Van Rooyen, L.; du Toit, D. H., Botha, E., and Rothmann, S., Artisan Retention in an organisation in South Africa. SA Journal of Human Resource Management, 8(1), p 8., 2010.

2019 SAUPEC/RobMech/PRASA Conference
Bloemfontein, South Africa, January 28-30, 2019

Bringing Back the Synchronous Compensator for the South Africa Power Network—Simulation and Compensator Technology

Christopher Africa
Department of Electrical and Electronic Engineering
Stellenbosch University
Stellenbosch, South Africa
17248310@sun.ac.za

Udochukwu B. Akuru
Department of Electrical and Electronic Engineering
Stellenbosch University
Stellenbosch, South Africa
udochukwu.akuru@unn.edu.ng

Maarten J. Kamper
Department of Electrical and Electronic Engineering
Stellenbosch University
Stellenbosch, South Africa
kamper@sun.ac.za

***Abstract*—With an increased penetration of renewable energy sources such as solar and wind in the South African power network, maintaining power system stability during network disturbance poses a major challenge. This paper is used to describe how synchronous compensators generally help to boost grid inertia and improve network dynamics in the event of a disturbance. The paper is also used to describe the functioning of a new type of synchronous compensator—the wound-field flux switching compensator (WF-FSC). Experimental tests conducted on a prototype shows that the WF-FSC does not only provide a more reliable technology, but it can also extend the reactive power range by operating without any field current due to saliency.**

Keywords—South Africa power network, synchronous compensator, synchronous generator, wound-field flux switching compensator (WF-FSC)

I. Introduction

South Africa is experiencing a changing mix of energy generation, specifically in renewable sources such as wind and solar [1]. Electricity generated from wind and solar resources closely follows the nation's electricity demand profile, meaning the country generates power at the time of day it is most needed. When wind and solar generation are combined, the net effect is a significant contribution to baseload power [2].

As South Africa is steadily crossing over to a higher penetration of renewables and less traditional thermal generation from coal in the near future, there are instances in the power grid where low short-circuit strength and even low system inertia may pose a challenge. The reason for this is that renewable energy sources are inherently variable and they lack the capability to support or tolerate faults that may occur on the grid [3]. The variable nature can also introduce stresses on power systems, making the need for grid management much more challenging. Furthermore, optimal locations for renewable power generation are often remote to the load centres where the power is needed, which puts a burden on the transmission system.

In light of the above, a solution can be found in the use of synchronous compensators. Synchronous compensators are used to adjust conditions on the electric power transmission grid. Its excitation is controlled in such a manner as to provide or absorb purely reactive power. Synchronous compensators also have high spinning inertia, which means they are able to stabilize the grid's network frequency and increase its stability during faults.

In this paper, a classical power system is modelled and investigated in terms of switching and balanced and unbalanced power system faults recovery. To this end, the effect of connecting a synchronous compensator on the switching and sudden dynamic fault instability of the power system is then illustrated. In the other part of this paper, a new synchronous compensator technology is investigated.

II. Power System under Study

The tendency of a power system to develop restoring forces equal to or greater than the disturbing forces, to maintain a state of equilibrium, is known as stability. If the forces that tend to hold machines in synchronism with one another are sufficient to overcome the disturbing forces, the system is said to remain stable [4]. In order to appraise the stability within a power system in the event of a disturbance, a synchronous compensator is applied to study the effect of the changing load angle on an interconnected synchronous generator in this section.

The power system under study consists of a synchronous generator connected to an infinite bus through a double transmission line circuit as shown in Fig. 1, both without and with a compensator. The infinite bus represents a bus-bar of constant voltage, which can deliver or absorb active and reactive power without any limitations. The generator is modelled as a 50 MVA, 30 kV, 0.8 lagging power factor synchronous machine, having a reactance of 9 Ω (0.5 p.u.), while the armature resistance is negligible. Other important machine parameters of the synchronous generator are given in Table I. Similarly, the synchronous compensator is assumed to have the same ratings as that of the synchronous generator. When operational, the governor of the compensator is spinning without any attached load and as such, its mechanical torque is approximately zero.

TABLE I PARAMETERS OF 50 MVA SYNCHRNOUS GENERATOR

Inertia constant	2 MJ/MVA
Frequency	50 Hz
Damping constant	20.19
Mechanical input power	0.8 p.u.

978-1-7281-0368-6/19/$31.00 ©2019 IEEE

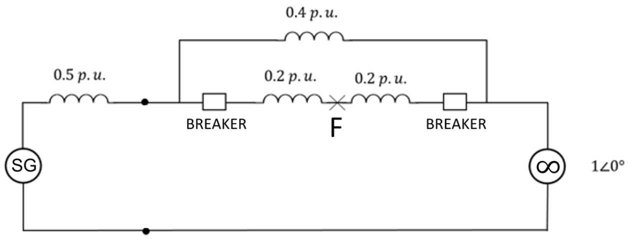

(a)

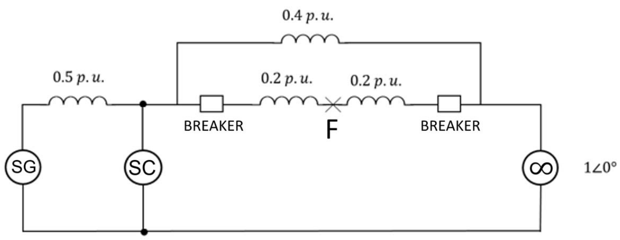

(b)

Fig. 1: Single-line diagram of the studied system: (a) without synchronous compensator, and (b) with synchronous compensator.

III. Switching and System Faults' Stability

To determine the dynamic behaviour of the power system under different disturbances, two case studies were investigated using the SIMSCAPE tool in MATLAB®, which is based on the power system model presented in Fig. 1. The simulations demonstrate the voltage, current, as well as load angle stabilisation ability of the synchronous generator under certain prescribed transient power system conditions, without and with the synchronous compensator connected. Note that, a three-phase high-value resistance is connected in parallel to the synchronous generator to make it operational in the MATLAB simulation.

In the first case, the power system, without the synchronous compensator connected, experiences a disturbance after opening a set of breakers. A synchronous compensator is then installed close to the generator to see its stabilisation response on the currents and voltages of the interconnected synchronous generator. The second case is initiated to study the effects of symmetrical and asymmetrical faults on the interconnected transmission lines, when the compensator inactive and active.

A. Breakers Opening

The result of the disturbance on the electrical power flow when opening the breakers shown in Fig 1 is plotted as shown in Fig. 2. One curve represents the power system without the compensator installed while the other curve represents the power system with the compensator installed. Clearly, the transient on the synchronous generator output power has less damping and more oscillations for the system without the compensator compared to that with one. The higher magnitude oscillation in the system without a compensator occurs because the drop in internal voltage inside the generator leaves the voltage at the terminals low enough such that it delivers less power. This results in an imbalance between the electrical output power and mechanical input power. The resulting imbalance stores kinetic energy in the machine's rotor and causes it to accelerate [5], [6].

Next, the effect of the disturbance on the synchronous generator's load angle is investigated. The breakers open at $t =$ 0.5 s which results in a "swing" in the generator's load angle at that instant as shown in Fig. 3. Again, it can be seen that a higher steady state magnitude with less transient vibration occurs in the system with the compensator activated, both before and after the breakers are opened. The less oscillation implies that an additional mechanical inertia provided by the compensator subdues the transient of the generator's load angle at a faster rate. It has been shown that the higher the compensator's inertia, the slower the rate of change of the load angle [6].

When operated without the synchronous compensator, the new steady state value of the load angle of the synchronous generator relative to the infinite bus when the breakers are opened can be calculated from the power transfer equation as follows:

$$P_e = \frac{|V_\infty||E|}{X_{eq}} sin\delta, \quad (1)$$

$$0.8 = \frac{1(1.419)}{0.5+0.4} sin\delta, \quad (2)$$

$$\delta = 30.43°, \quad (3)$$

where P_e is the electrical power delivered from the synchronous generator, V_∞ is the voltage at the infinite bus, E is the internal generated voltage of the synchronous generator, X_{eq} is the sum of the synchronous reactance and the transmission line reac-

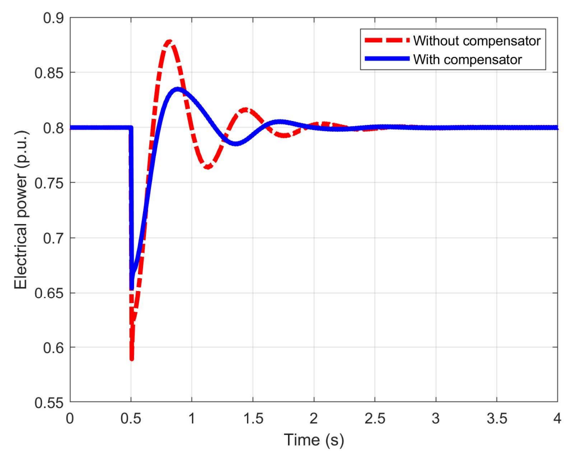

Fig. 2: Synchronous generator electrical power delivered to infinite bus.

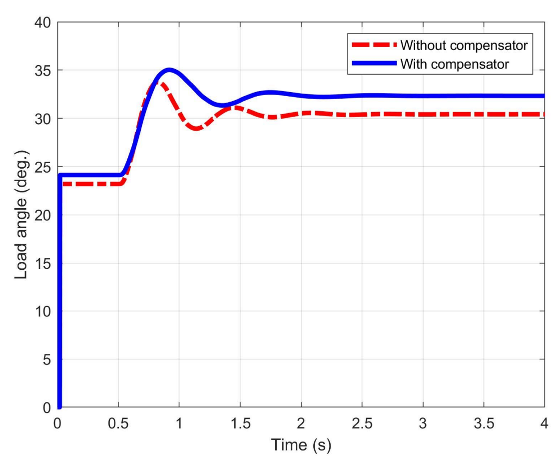

Fig. 3: Synchronous generator load angle with open breakers.

TABLE II PARAMETERS OF LOAD ANGLE AFTER OPENING BREAKERS (H = 2 MJ/MVA)

	With Compensator	Without compensator
δ	32.33°	30.42°
V_t	1.08 p.u.	1.14 p.u.
X_{eq}	1.36 p.u.	1.37 p.u.

tance, and δ is the load angle of the generator relative to the infinite bus. Table II indicates the final steady state values as evaluated from Figs. 2 and 3. Table II also shows the steady state terminal voltages in per unit as having higher flat voltage profile when the compensator is active. Moreover, the sharp difference observed in the values estimated for V_t (voltage at the synchronous generator terminals) is responsible for the similarity of the initial and final steady state values in Fig. 2.

B. Symmetrical and Asymmetrical Faults

1) Symmetrical Fault: A balanced (symmetrical) three-phase short-circuit fault is first introduced in the centre of the transmission line at the points marked **F** in Fig. 1. The system operating wihout a synchronous compensator is considered first. The fault is suddenly applied at time $t = 0.1$ s and removed at time $t = 0.72$ s. After introducing the fault, a swing in the electrical power of the generator occurs, giving the rotor extra kinetic energy. As the rotor accelerates, an inrush of line current starts to flow through the operating line as indicated between the interval of the fault as shown in Fig. 4. The increase

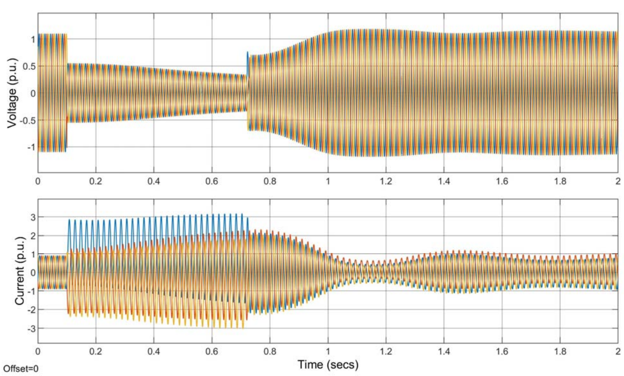

Fig. 4: Line voltages and current after balanced three-phase short-circuit fault (without synchronous compensator).

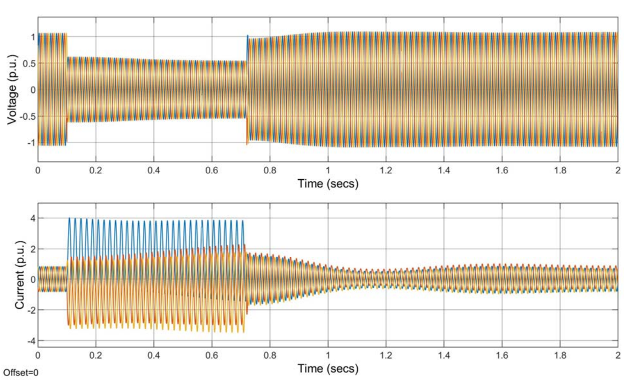

Fig. 5: Line voltages and current after balanced three-phase short-circuit fault (with synchronous compensator).

TABLE III STEADY-STATE VALUES OF SYNCHRONOUS GENERATOR VOLTAGE AND CURRENT AFTER THREE-PHASE FAULT

	With Compensator		Without compensator	
	Initial	Final	Initial	Final
Voltage	1.064 p.u.	1.081 p.u.	1.099 p.u.	1.145 p.u.
Current	0.831 p.u.	0.794 p.u.	0.908 p.u.	0.835 p.u.

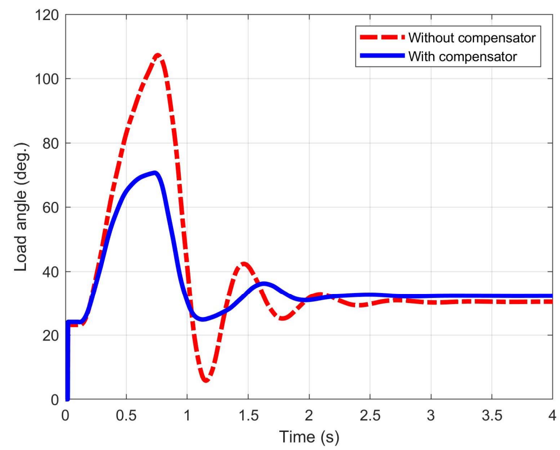

Fig. 6: Synchronous generator load angle under three-phase short-circuit to ground fault.

in line current results in decrease in the terminal voltage due to the voltage drop across the generator's synchronous reactance.

The case of the synchronous compensator connected to the power system is considered next. The resulting terminal voltages and line currents before, during and after the fault is shown in Fig. 5. When compared with the first case in Fig. 4 without compensator, one can see a remarkable improvement in the steady-state voltage and current dynamics. Note that, the higher magnitude of the line currents in Fig. 5 is due to the reactive power component afforded by the presence of the compensator. The initial and final steady state values are summarised in Table III. It is also seen that the per unit voltage and current values become more stable almost immediately after the fault is cleared, when the compensator active.

In both cases, the generator therefore exports the same amount of electrical power as it receives from the mechanical input power. To this end, the load angle variation is further compared in Fig. 6 under the balanced three-phase short-circuits whereby the system with synchronous compensator displays higher steady state amplitude with lesser oscillation at a quicker recovery time.

2) Asymmetrical Faults: Two cases of unbalanced faults are implemented in terms of single phase-to-ground and line-to-line faults, without and with the compensator connected to the power system. The results are reported in Figs. 7-12. Once again, flattened steady state voltage profiles and reduced currents are achieved on the systems with compensator immediately after full recovery from the asymmetrical faults. Also, the steady-state load angles are higher while lesser oscillations and faster time to stability occurs when the compensator online. This clearly shows that the synchronous compensator will exhibit the same characteristics towards grid stability after fault irrespective of whether the occurrence of the faulty system is symmetrical or not.

IV. Flux Switching Synchronous Compensator Technology

From the foregoing, we have shown that synchronous compensators can provide reactive power, while offering inertia and short-circuit comfort during balanced and unbalanced sudden power system dynamics. Generally and conventionally, rotating synchronous compensators are designed from wound-rotor synchronous machines, which more or less give the ability for voltage regulation and reactive power compensation, among others.

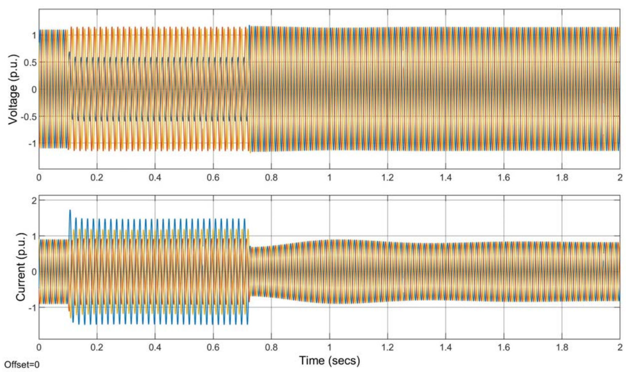

Fig. 7: Line voltages and current after a single phase-to-ground fault (without synchronous compensator).

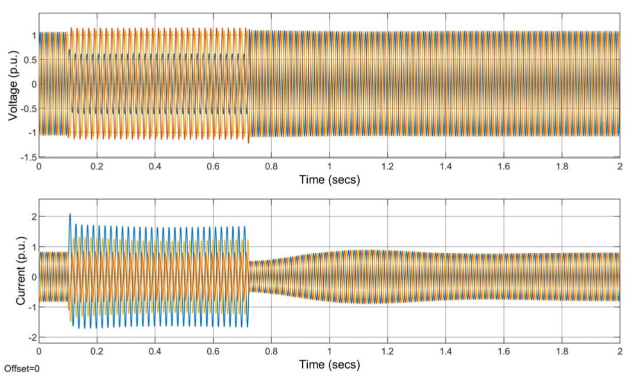

Fig. 8: Line voltages and current after a single phase-to-ground fault (with synchronous compensator).

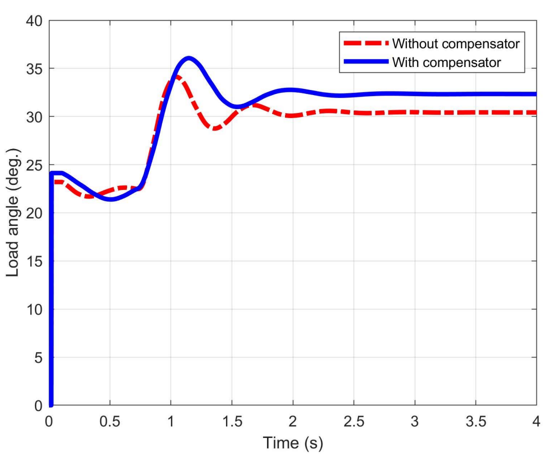

Fig. 9: Synchronous generator load angle under single line-to-ground fault.

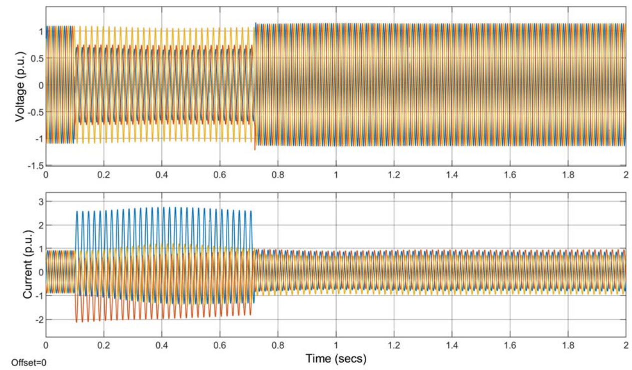

Fig. 10: Line voltages and current after a double line-to-line fault (without synchronous compensator).

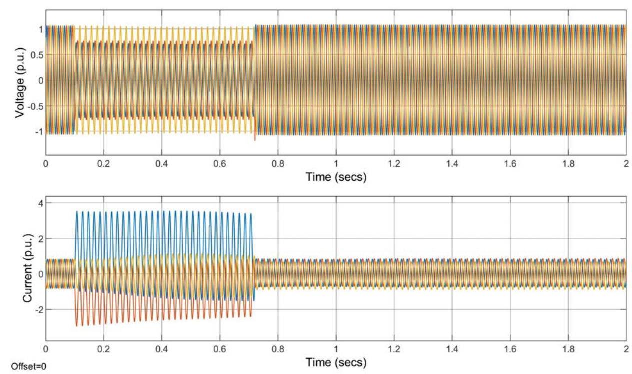

Fig. 11: Line voltages and current after a double line-to-line fault (with synchronous compensator).

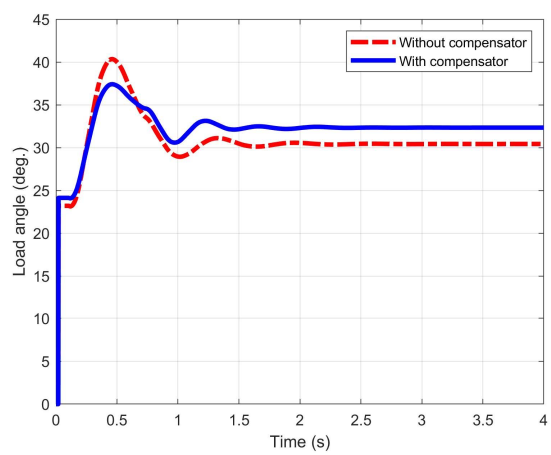

Fig. 12: Synchronous generator load angle under double line-to-line fault.

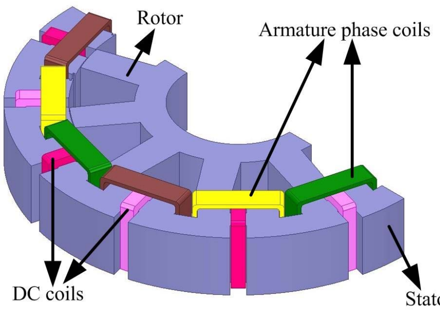

Fig. 13: 3-D cut-out of a three-phase 12-staor/10-rotor WF-FSC.

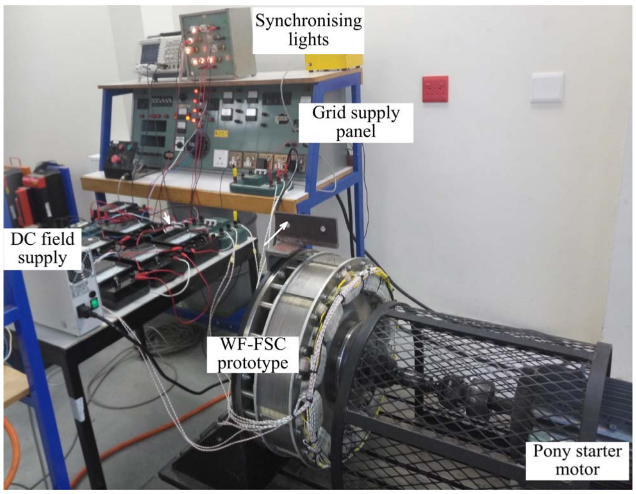

Fig. 14: Experimental test bench of grid-connected WF-FSC prototype.

In the second part of this paper, we present a novel alternative synchronous machine technology, the so-called wound-field flux switching synchronous compensator (WF-FSC) for the South African electrical power grid. Our proposal is based on successful experimental demonstration based on a prototype designed for small-scale power applications [7].

The flux switching machine is a non-conventional stator-mounted double salient synchronous machine which operates on the principle of change in permeance due to high magnetic reluctance difference of its rotor teeth [8]. The main advantages of the flux switching machine are given as high power density, high efficiency, robust rotor topology and easy thermal management. When designed with wound-field coils as being proposed here, there is no need for brushes and slip rings as all the active coils are solely mounted unto the stator, making it intrinsically brushless! Also, the mechanical fidelity of its unencumbered rotor implies that it can provide high inertia needed for fast dynamic response in power system compensators. The highlight of the proposed synchronous compensator technology for the South African power network utility is that the machine can be fully manufactured locally without incurring any overseas expenses. A structural proof of the WF-FSC technology is presented as shown in Fig. 13.

A. Experimental Setup and Initial Tests

The experimental bench is set-up as shown in Fig. 14. The first stage of the experiments involved conducting no-load and

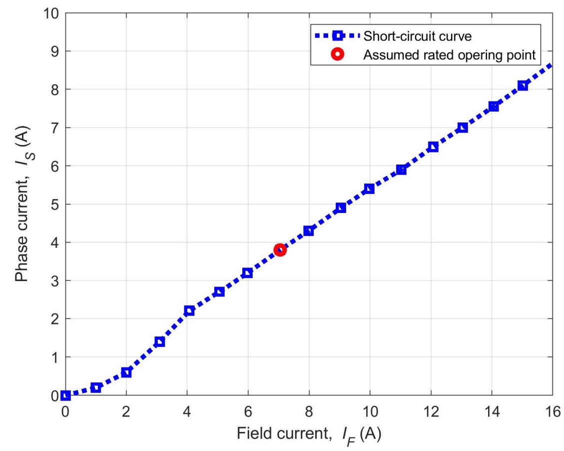

Fig. 15: Short-circuit characteristics of the WF-FSC prototype.

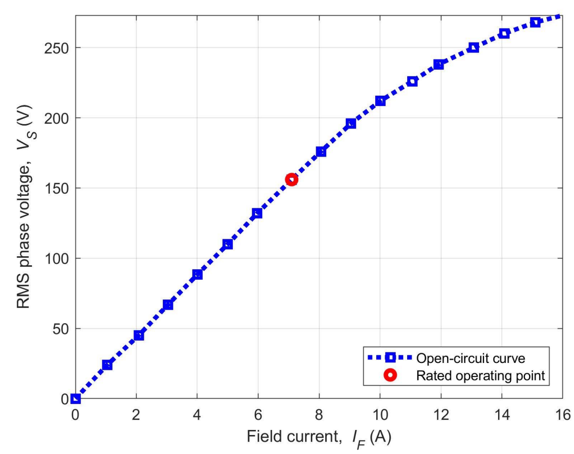

Fig. 16: Open-circuit characteristics of the WF-FSC prototype.

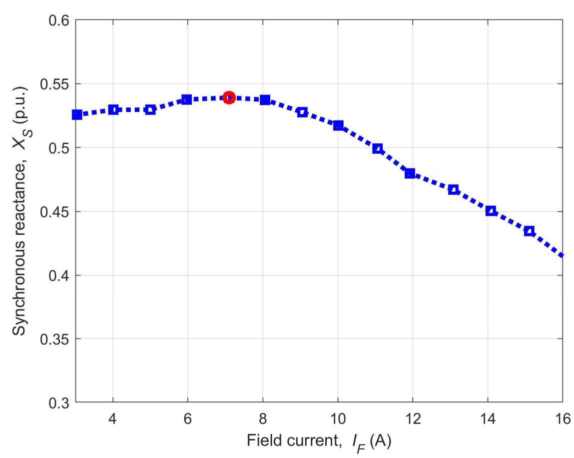

Fig. 17: Approximated unsaturated and saturated per unit synchronous reactance of the WF-FSC prototype.

short-circuits tests to establish the approximate base values for the assumed operating point. Although the machine was designed for 10 kW power when operating at 795 V (line voltage),

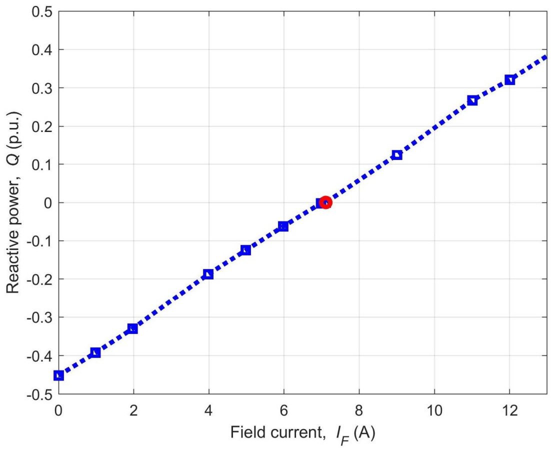

Fig. 18: Reactive power compensation capability.

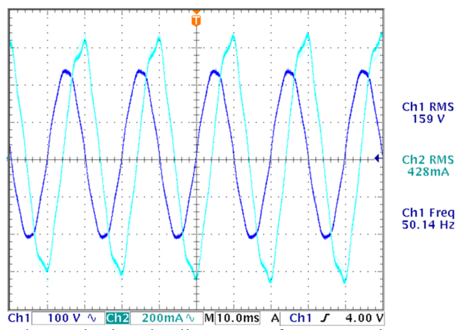

Fig. 19: Under-excitation: leading power factor, reactive power supplied.

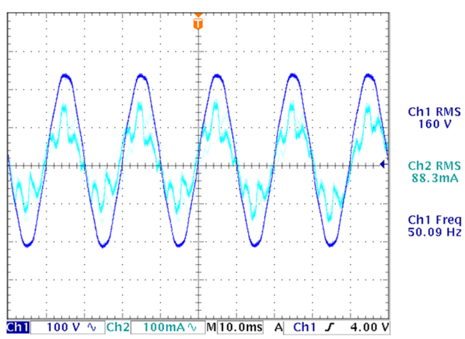

Fig. 20: Unity power factor, zero net reactive power.

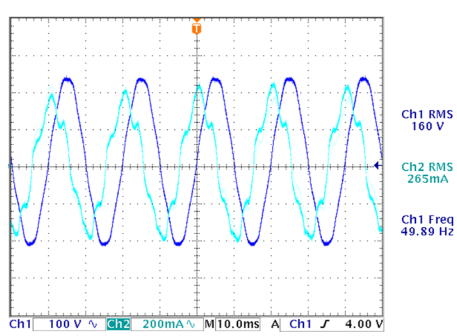

Fig. 21: Over-excitation: lagging power factor, reactive power absorbed.

60 Hz, but because of the grid code requirement in South Africa which constrains the power network supply to 50 Hz, we had to assume a grid integration operating point of 280 V (rated line voltage) at the rated field current. From the short-circuit tests and open-circuit characteristics shown in Figs. 15 and 16, the per unit synchronous reactance characteristics, which clearly show the per unit unsaturated ($I_F \leq 8$ A) and saturated ($I_F > 8$ A) reactance values, is determined as shown in Fig. 16.

B. Grid-Connected Tests

Upon successful synchronisation to the grid and the switching off of the starter motor which satisfies the operation of the WF-FSC as a true compensator ($P_e \approx 0$), the field current values are controlled up and down from the assumed rated operating point to measure the reactive power capability of the WF-FSC. As shown in Fig. 18, the WF-FSC is able to both supply and absorb reactive power when the field current is under-excited and overexcited, respectively. At unity power factor, only a small fraction of real power is being absorbed by the WF-FSC as the net reactive power is zero. As a matter of fact, even when the field supply is completely switched off, the WF-FSC remain in synchronism to the grid due to the rotor saliency while eminently supplying reactive power. This revelation further deepens the reliability of the WF-FSC, which is now behaving as a pseudo synchronous reluctance machine. Figs. 19-21 simply show the voltage and current characteristics at different power factor stages as captured during the tests. Note that, the current probe of the oscilloscope reading has a multiplier factor of approximately 3.5. The concern on the observed harmonics indicated in the current waveforms of the proposed WF-FSC is likely to be addressed by improved design considerations.

V. Conclusion

In the paper, it is shown that the synchronous compensator can add much stability to the power system grid. These compensators can be installed and connected to the South African power grid to boost network stability in answer to higher penetration of renewable energy sources for power generation. While it is a viable solution to implement them by using South Africa's abandoned but functional old synchronous generator plants [3], we have been able to show the feasibility of a new attractive, low-maintenance compensator technology—the wound-field flux switching synchronous compensator (WF-FSC). Interestingly, it can even run without field current due to inherent saliency, which increases its reliability and reactive power range, but it remains to be seen how much its saliency characteristics differ from conventional salient pole synchronous machines. Based on an experimented prototype, a synchronous reactance of $X_s \approx 0.55$ p.u. is obtained at the considered power range. The concern of the harmonics observed in the measured currents waveforms can be overcome by redesign.

Acknowledgment

The authors wish to acknowledge Kenan Cloete, Andrew Loubser and staff of the Electrical Machines Workshop, Stellenbosch University, for their assistance in the experiments.

References

[1] DRAFT IRP-2018: INTEG RATED RESOURCE PLAN – Department of Energy, Republic of South Africa, August 2018. Accessed online on 2018/10/16 at: http://www.energy.gov.za/IRP/irp-update-draft-report2018/IRP-Update-2018-Draft-for-Comments.pdf

[2] LOREISFONTEIN WIND FARM, Analysis shows South Africa's wind and solar power generation matches demand profile. Accessed online on

2018/09/27 at: https://loeriesfonteinwind.co.za/analysis-shows-south-africas-wind-and-solar-power-generation-matches-demand-profile/

[3] C. Szabo, Synchronous condensers: An old tool rediscovered to address grid challenges. *Power Engineering International*, December 2017.

[4] D. P. Kothari *Modern power system analysis.* New Delhi: Tata McGraw-Hill, 2011.

[5] Y. Katsuya, Y. Mitani and K. Tsuji, "Power system stabilization by synchronous condenser with fast excitation control," Proc. Int. Conf. Power Syst. Technol., Perth, Australia, vol. 3, pp. 1563–1568, Dec. 4–7, 2000.

[6] C. Africa, *Synchronous compensators and new synchronous machine technology*, BEng Technical Report, Stellenbosch University, South Africa, October 2018.

[7] U. B. Akuru and M. J. Kamper, "Novel Experimentation of a 10 kW Geared Medium-Speed Wound-Field Flux Switching Wind Generator Drive," 2018 IEEE Energy Conversion Congress and Exposition, Portland, Oregon, pp. 6492-6498, September 23-27, 2018.

[8] M. Cheng, W. Hua, J. Zhang, and W. Zhao, "Overview of stator–permanent magnet brushless machines," *IEEE Transactions on Industrial Electronics*, 58(11), pp. 5087–5101, 2011.

Monitoring of the service cable PEN conductor to assure bonding using a smart split meter

David Scheepers, Johan Beukes
Dept. of Electrical and Electronics Engineering
Stellenbosch University
Stellenbosch, South Africa
davidjjs@me.com, jbeukes@sun.ac.za

***Abstract*—This paper investigates a method for monitoring the service cable PEN conductor on a smart grid to provide information regarding deteriorating infrastructure. The consequences of leaving a deteriorated or broken service cable PEN conductor is examined for the TN-C-S earthing scheme using smart split meters. The feasibility of implementing a monitoring method is evaluated through system modelling and simulation as well as implementation on a physical setup. Simulation and experimental results indicated that it would indeed be able to approximate the service cable PEN conductor value but require more investigation regarding the behaviour of the incidental earthing impedance.**

***Index Terms*—smart meter, smart grid, PEN conductor failure, safety**

I. Introduction

Broken conductors introduce various hazardous conditions leading to fatalities each year. Detecting these various hazards is therefore of the utmost importance. A common hazard that occurs is overvoltage on conductive parts of appliances due to a broken protected earth (PE) and neutral (N) conductor. These PEN conductors could be either overhead low-voltage feeder PEN conductors, thus leading to a larger area being exposed to the hazard, or service cable PEN conductors, localizing the hazard.

The capability to investigate various characteristics of the distribution network has been introduced by newly developed smart grid technologies. These smart grids implement smart meters to take measurements at various locations to monitor power quality [1], improve network awareness [2] and prevent electricity theft [3]. The ability for smart meters to communicate with a centralised data concentrator allows for accurate fault location identification. This makes identifying and resolving such faults easier for the power utility.

A method for monitoring the LV feeder impedance using a smart meter [4] has been developed which provides a basis on which capabilities can be expanded. This method is capable of detecting when an overhead LV feeder PEN conductor is deteriorating or broken resolving the first possible case of deteriorated or broken PEN conductors. This method, however, does not monitor the service cable PEN conductor as it is not included in the closed loop feeder impedance being monitored upstream from the smart split meter.

The objective of this paper is to demonstrate how the service cable PEN conductor can be continuously monitored downstream from a smart split meter at a customer's pole top box. The method was mathematically modelled, implementing system analysis on a single customer installation. This mathematical model was then implemented on a microcontroller to test the developed method on an experimental system model. The service cable PEN conductor impedance was then approximated using current measurements. The results were investigated using different types of proposed analysis methods.

II. Implications Introduced by PEN Conductors

The terra neutral combined-seperate (TN-C-S) earthing system is the earthing scheme that is investigated for this paper. The TN-C-S earthing scheme is one of two LV distribution earthing systems that is prescribed by the South African National Standard (SANS) 10292 [5].

The TN-C-S system makes use of combined protected earth and neutral conductors to reduce the overall cost. TN-C-S therefore has the risk of losing the protective earthing as well as the earthing provided by the source side if the PEN conductor breaks, as can be seen from Fig. 1.

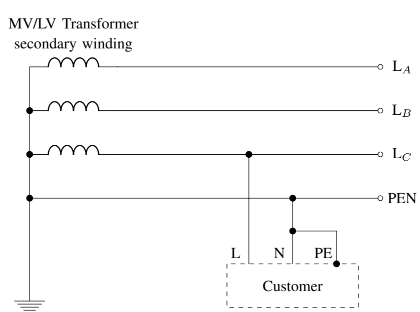

Fig. 1: Single-phase connection from a three-phase feeder implementing TN-C-S earthing system

Loss of the earth bonding will lead to a hazardous condition during which all the appliances' conductive parts reach phase voltage, even when they are not switched on [6]. If a person were to come into contact with any of the exposed conductive parts they will provide an alternative path to ground causing them to be electrocuted. This problem would not be detected as currently implemented protective devices such as the residual-

978-1-7281-0368-6/19/$31.00 ©2019 IEEE

current devices (RCDs) would not be able to prevent such a fault as the currents will remain balanced.

A deteriorating service cable PEN conductor creates a similar hazardous condition with the exception that appliances' chassis do not instantly reach phase voltage due to a high impedance break. A service cable could already be considered to be deteriorated when it reaches an impedance of several ohms. From Fig. 2 it can be seen that both the service cable PEN conductor (Z_{PEN}) and the incidental earthing impedances (Z_{IE}) influence the size of the current that will flow through the incidental earthing.

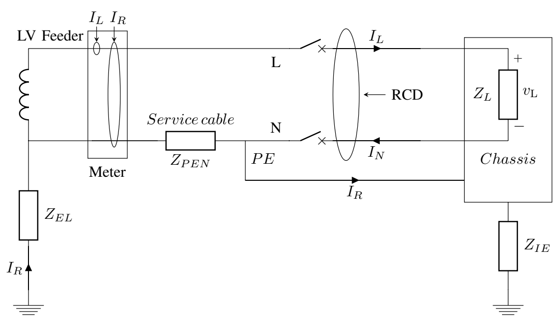

Fig. 2: Model of a LV system implementing a TN-C-S system with a single-phase connection to a customers installation

Being able to approximate when the service cable PEN conductor is severely deteriorated, thus being able to replace it before it breaks, would improve safety. This would allow for the prevention of fatalities and reduce the risk of fire hazards due to heating caused by current flowing through appliances' chassis [7]. As the PEN conductor is expected to slowly deteriorate, unless breakage is caused by external circumstances, monitoring the cable will have great benefits.

III. Service Cable PEN Conductor Monitoring Strategy

The method developed in [4] made use of changes in voltage and current to measure the line impedance. This method could also have been implemented to measure the service cable PEN conductor if measurements could be taken from the pole top box and inside the customers installation. This would, however, not be an acceptable method as a customer interface unit (CIU) is the only hardware that the customer should be able to interface with [8].

The suggested method for monitoring the service cable PEN conductor is to measure the live (I_L) and neutral current (I_N) at the smart split meter. These currents will then be used to calculate the residual current (I_R), as seen by the smart meter. Using the relationship between the live and residual current an approximation of the PEN conductor impedance could be made. This approximation will require prior knowledge of the behaviour of the incidental earthing as well as a deteriorating PEN conductor.

The PEN conductor is expected to slowly deteriorate over time or suddenly break, therefore the impedance value will increase and never decrease, unless the service cable is replaced. When the PEN conductor breaks it will immediately be detectable by the split meter as the residual current will be equal to the live current from that instance onwards.

The behaviour of the incidental earthing is however more random as various external factors influence its behaviour. In most rural settings generally very few appliances are implemented and it would be expected that these appliances would remain connected therefore keeping the incidental earthing fairly constant.

Environmental factors such as temperature, humidity and ground dampness also influence the incidental earthing value [9] but were considered to be insignificant for the purposes of this paper. The behaviour of the incidental earthing would however be better understood if it is monitored over time, such as proposed in section IV-C.

Instead of taking voltage measurements, that would only be able to identify the upstream impedance, this method will measure current changes that occur. By applying Ohm's law on the basic load diagram in Fig. 3, at a time instance k, Eq. (1), the equivalent impedance, can be deduced combining the earth conductor impedance (Z_{EL}) with the incidental earthing (Z_{IE}) to obtain a single earthing impedance ($Z_E = Z_{IE} + Z_{EL}$).

$$Z_{eq} = Z_L + Z_{PEN} \,||\, Z_E \tag{1}$$

Eq. (1) could then be used to calculate the live current drawn by the load at time instance k, as seen in Eq. (2).

$$i_L(k) = \frac{V_s}{Z_{eq}} \tag{2}$$

Implementing Kirchhoff's current law the current that is directed towards the PEN conductor (Z_{PEN}) and earthing impedance (Z_E) could be deduced using the current division principle. Eq. (3) and (4) indicates this current division.

$$i_1(k) = \frac{Z_E}{Z_E + Z_{PEN}} \times i_L(k) \tag{3}$$

$$i_2(k) = \frac{Z_{PEN}}{Z_E + Z_{PEN}} \times i_L(k) \tag{4}$$

Using Eq. (1), (2) and (4) yields

$$Z_{PEN} = \frac{i_2(k)}{i_L(k) - i_2(k)} \times Z_E \tag{5}$$

which has $i_2(k)$ representing the residual current (i_R) that flows through the incidental earthing impedance. Subtracting time instance k-1 from time instance k using the same values for Z_E and Z_{PEN} would result in Eq. (6).

$$Z_{PEN} = \frac{\Delta i_R}{\Delta i_L - \Delta i_R} \times Z_E \tag{6}$$

This proves that the PEN conductor impedance can be approximated using step changes in the residual and live currents measured at the smart meter.

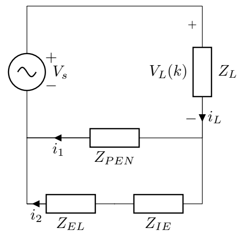

Fig. 3: Simplified system model used to illustrate current division principle

As smart meters implement RMS values calculated over periods of one-second, this would lead to the inclusion of RMS values in the formula stated in Eq. (6). To avoid unnecessary calculations, which would lead to inaccurate approximations, a threshold value is applied to ignore small changes in the measured live current.

In the process of implementing the RMS value a distinguish difference occurred. This can be seen in Fig. 4 illustrating how the instantaneous current change can occur during an RMS sampling time frame.

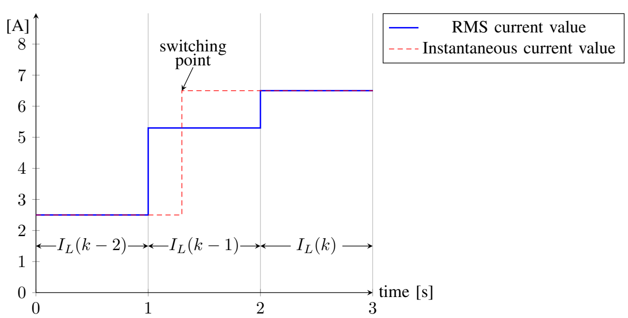

Fig. 4: Representation of RMS and instantaneous delta current changes

Using the RMS value that is calculated during the switching time frame would result in large errors, as seen in Fig. 4. The method therefore had to be adapted to ignore the step RMS current measurement. This lead to the delta values being calculated as follows:

$$\Delta I_L(k) = I_L(k) - I_L(k-2) \tag{7}$$

$$\Delta I_R(k) = I_R(k) - I_R(k-2) \tag{8}$$

This, however, does not change the implementation of the formula as stated in Eq. (6). Using RMS current changes rather than instantaneous current changes is merely introduced.

IV. Possible Analysis Methods to Account for Variability of the Incidental Earthing Impedance

It should be noted that the incidental earthing and PEN conductor value are both unknown variables in the proposed solution stated in Eq. (6). From this equation it would not be possible to approximate both the incidental earthing and the PEN conductor value. As mentioned in Section III the known characteristics are investigated to establish the expected behaviour of these unknown variables.

Various methods could be implemented to monitor the behaviour of the incidental earthing impedance and analyse the data to approximate the PEN conductor value. The first method that is proposed implements boundaries to limit the approximation value of the PEN conductor. The second method implements statistical analysis, distributing the data and obtaining a statistical approximation of the PEN conductor value implementing a fixed incidental earthing impedance value. The third introduced method mainly focuses on obtaining the characteristics of the incidental earthing. This is done using the same approximation approach as for the PEN conductor but implementing a fixed value for the PEN conductor instead of the incidental earthing impedance.

Implementing a random incidental earthing impedance value (Z_{IE}) Fig. 3 could then be modelled in MATLAB. Using the proposed mathematical models this system could then be used to test the different analysis methods. MATLAB's simscape library was used and provided sufficient tools to evaluate all these methods.

A. Ranged Method

This method implements the principle of implementing a maximum and a minimum value for the incidental earthing impedance. It would therefore be possible to monitor the value of the PEN conductor between the established ranges. The value of the PEN conductor will not be able to fall below a previously established minimum value or a future established maximum value, due to its expected behaviour to only increase linearly. This provides a better approximation range over time decreasing the uncertainty regarding the exact value of the PEN conductor.

This method would, however, produce erratic results if the incidental earthing value could change drastically (with a few kilo-ohm range). This is considered to be a problem if various loads are implemented and frequently connected and disconnected from the installation. The results for a small range, seen in Fig. 5 relative to a large range, seen in Fig. 6, clearly indicate the accuracy limitation caused by these ranges. The trend graph is designed to abide by the restrictions of the lower and upper boundaries mentioned above.

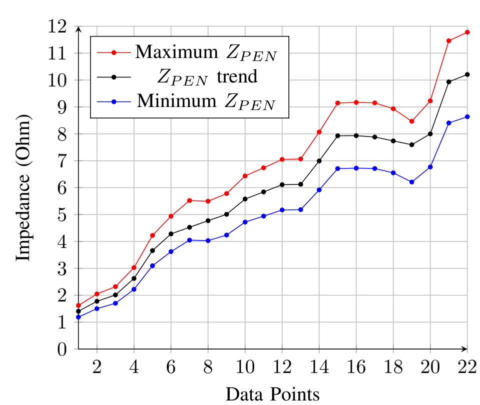

Fig. 5: Ranged approximation with a small incidental earthing range (1000 Ω to 1500 Ω)

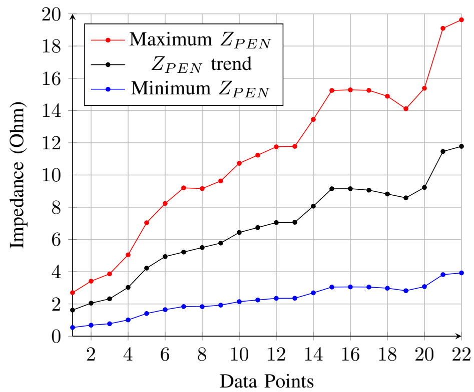

Fig. 6: Ranged approximation with a large incidental earthing range (500 Ω to 2500 Ω)

For a small incidental earthing range the results would vary by an insignificant amount 0.22 Ω to 1.6 Ω. The large incidental earthing range, however, has a variation range of 1.1 Ω to 7.9 Ω. It would therefore be more difficult to accurately estimate the exact value of the PEN conductor. This method could therefore only be implemented if the incidental earthing does not vary significantly, as is commonly expected.

B. Statistical Analysis Method

A superior method was also developed that implements statistical analysis of the data points to identify outliers as well as indicating the distribution. Over time a median value could be identified that would closely represent the true value of the PEN conductor.

This method is advantageous when a constant value is monitored as it allows for greater insight into the distribution of the approximated values. This method could be implemented using a fixed (mean) incidental earthing value such as 1 kΩ, which was selected for the experimental investigation. In the MATLAB simulation this produced the results indicated in Fig. 7 for two random PEN conductor impedance values.

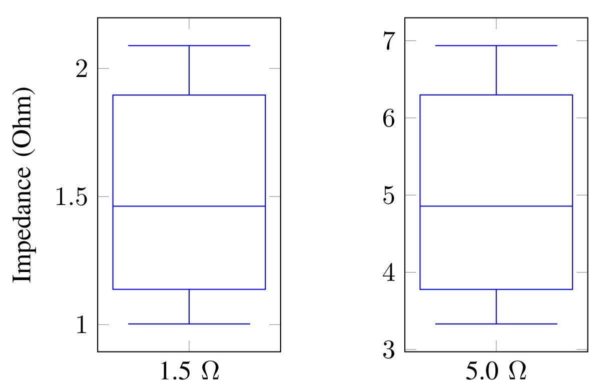

Fig. 7: Box plot distribution of data for constant PEN conductor values of 1.5 Ω and 5.0 Ω implementing a random incidental earthing impedance

From the box plots it can be concluded that the data points are normally distributed. It is also noted that the actual PEN conductor value falls within the interquartile range (IQR), the range between the 25^{th} percentile and the 75^{th} percentile. Having these analysis tools available illustrates how the box plot method of displaying the data is rather sensible.

C. Variable Initialisation Method

A final method was developed that implements a completely different approach to establishing the incidental earthing. This method implements analyses over an extended period of time during which the PEN conductor is expected to remain constant. Since the PEN conductor will naturally deteriorate at a slow rate the value of a new conductor, of approximately 0.5 Ω [10], could be implemented. It would therefore be possible to establish the behaviour of the incidental earthing using an adjusted version of Eq. (6) seen in Eq. (9).

$$Z_E = \frac{\Delta i_L - \Delta i_R}{\Delta i_R} \times Z_{PEN} \tag{9}$$

The main principle of this method is to determine the rate to which the a specific installation's incidental earthing impedance would vary. This information could then be implemented along with the statistical method to analyse the data further. A brief period of a few days would be required to establish an accurate profile of the incidental earthing impedance value. This method could thereafter be implemented in monthly intervals to account for the changing condition of the installation. The previous established value for the PEN conductor will then be kept constant during these re-evaluation periods.

V. Experimental Model

To evaluate the proposed method for monitoring the service cable PEN conductor using current measurements a physical system, representing what a typical system would look like, was built. This experimental model is illustrated in the diagram seen in Fig. 8.

This experimental setup implements two variable resistors, to acquire the desired values for the PEN conductor and the incidental earthing impedance, two current transducers to measure the live and residual current and three appliances that could be switched on and off independently. This method was originally intended to be implemented on the Texas Instruments (EVM430-F6779) E-meter which has all the required capabilities [11] to be implemented in this experiment.

The incidental earthing impedance was kept constant (at 1 kΩ) for this experimental setup. It would however be sensible to implement a method that would be able to identify the behaviour of the incidental earthing therefore expanding from using a constant value to a behaviour related variable. The method that was suggested in Section IV-C could therefore be implemented to address the unknown variability but was not implemented in this test setup.

Three typical household appliances were implemented in this experimental setup including loads with power ratings of 1500W, 1200W and 750W. The incidental earthing is typically introduced by any physical connection appliances make with earth, examples are through pipes running into the ground and a refrigerator standing on a damp floor. These connections to ground provide an alternative path back to the transformer and could be estimated to be around 1 kΩ at a customer's installation.

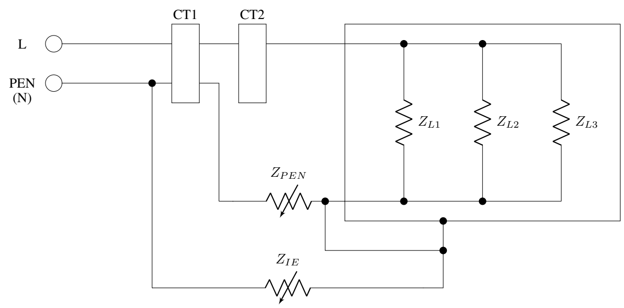

Fig. 8: Basic diagram of experimental setup

Two types of tests were conducted using this experimental setup. The first test utilised a single load being switched on and off, only implementing the two largest loads. The second test involved switching all three the loads randomly. The results were then documented through a serial communication port connected to a computer. These tests were conducted implementing a basic microcontroller.

VI. Experimental Results

The documented experimental results that were captured through the serial communication port can be seen in Fig. 9 - 11 for the various test conditions.

A. Single Switched Load with Increasing PEN Impedance

The results obtained in Fig. 9 - 10 are from switching two single loads, represented by Z_{L1} and Z_{L2} in Fig. 8. Values were only obtained when a load was switched therefore not implementing time as the x-axis label but rather the data points obtained at random instances.

The value of the PEN conductor was incrementally increase from 1 Ω to 10 Ω (using increments of 1 Ω) to test the method over a wide range of values. A threshold that would require a substantial current change to occur (larger than 1 A) was implemented to reduce inaccuracies from being introduced.

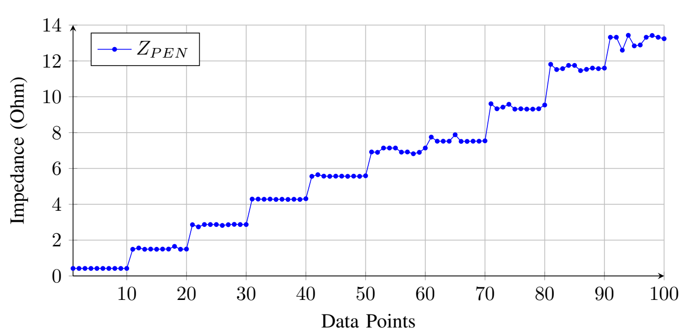

Fig. 9: PEN conductor impedance with Z_{L1} switched on and off with an average load draw of 4.3 A

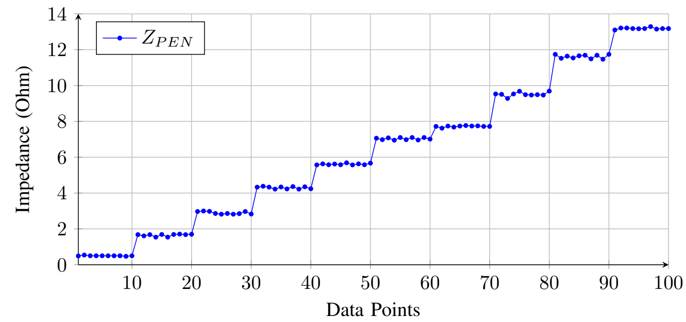

Fig. 10: PEN conductor impedance with Z_{L2} switched on and off with an average load draw of 5.4 A

From the results in Fig. 9 - 10 it could be concluded that the approximation method is able to track a change in the PEN conductor impedance value. The accuracy does however vary more significantly with higher impedance values.

B. Multiple Switched Loads with Increasing PEN Impedance

Multiple loads being switched at random represents the actual behaviour that would be expected from a typical installation and would result in larger overall current changes. This was tested using the three appliances, Z_{L1}, Z_{L2} and Z_{L3}, and switching them on and off in random combinations, thus having greater variability in current changes.

This test was conducted on four randomly set values for the PEN conductor impedance. These values were measured, after testing, using a multimeter and was found to be 2.8 Ω, 4.9 Ω, 7.2 Ω and 10.1 Ω. This would be the different indication stages of a deteriorating PEN conductor with a new conductor of course being at 0.5 Ω and a severely deteriorated PEN conductor reaching a value as great as 10 Ω.

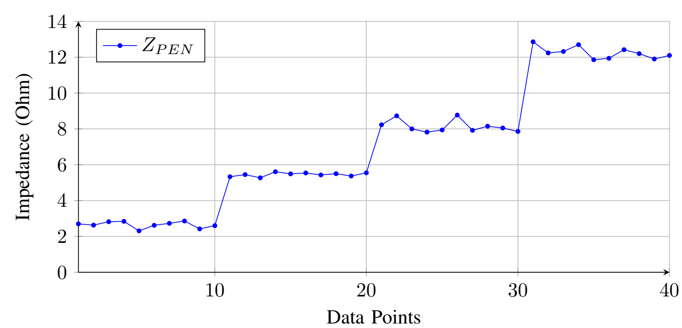

Fig. 11: PEN conductor impedance of randomly selected values (2.8 Ω, 4.9 Ω, 7.2 Ω and 10.1 Ω) with multiple loads (Z_{L1}, Z_{L2} and Z_{L3}) switched on and off randomly

This test identified that the accuracy of the method is dependent on the overall current change that occurs. In Fig. 11 this is visualised as the approximated values have a slightly smaller error relative to the single load switching test.

The inaccuracies are still realised and could have been introduced by inaccurate readings produced by the microcontroller processing the input, as a smart meter with significantly greater capabilities and accuracy was not implemented. The results, however, still proved to be significant in detecting a deteriorating conductor. As the exact value of the PEN conductor is not of great importance but only having an indication of the state of the conductor.

When the approximation method therefore reaches a range during which it experiences increased accuracy errors maintenance needs to be conducted to prevent any possible injuries or fatalities from occurring.

Analysing the results from Fig. 11 using the proposed statistical method to identify the minimum value, 25^{th} percentile, median, 75^{th} percentile and maximum value. This would give a better understanding of the distribution of the obtained data and indicate the IQR in which the true value is most likely to be approximated. This box plots of Fig. 11 can be seen in Fig. 12.

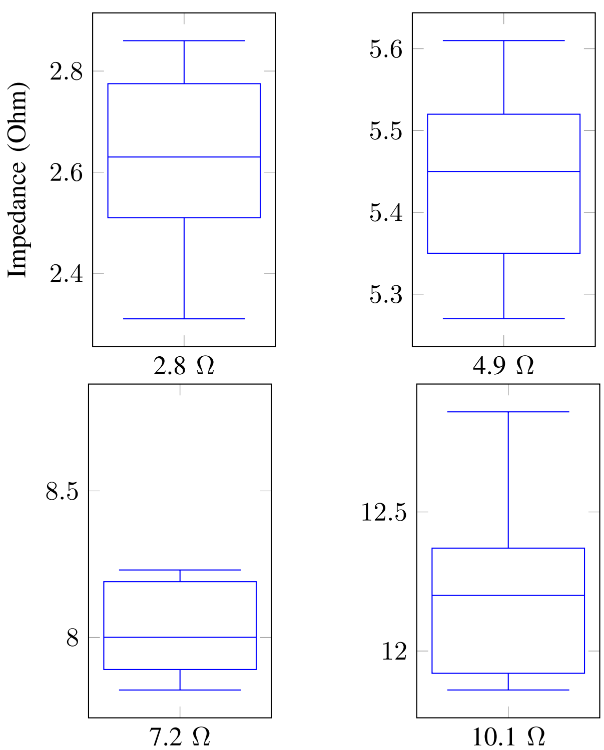

Fig. 12: Box plots of various randomly implemented PEN conductor values

The median value was found to differ with as little as 6.25% for small values to as much as 21% for larger values.

VII. Conclusion

This paper presents a proposed method for monitoring the service cable PEN conductor using a smart meter. This was found to be necessary due to the safety hazards that are associated with broken PEN conductors.

The proposed method made use of a current division principle making use of changes in the live and residual current which could be measured by a smart meter located at the pole top box. The equation that was derived mathematically also implemented changes in RMS current readings as it is common practise for smart meters. The PEN conductor impedance could therefore be approximated and statistically analysed to acquire a better approximation over time.

An experimental investigation concluded that the proposed method would work significantly well if an indication of whether the PEN conductor is reaching a high impedance value is required. After having done a single load and a multiple load test it was also concluded that the approximation method would also be dependent on the size and way the currents changed. Smaller errors were introduced when switching multiple loads which is the case expected from most typical installations.

This method could therefore be implemented on a more advanced smart meter which would produce more accurate readings and would be implementable in a smart grid.

References

[1] P. Uys, “Power quality using smart meters with communication,” Stellenbosch University, Final year project, 2017.

[2] J. Wattel, “Enabling low voltage grid visibility to detect safety hazards,” Master’s thesis, Stellenbosch University, 2017.

[3] A. Kilian and S. Herbst, “Eskom rolls out new smart meter technology to fight electricity theft,” http://www.engineeringnews.co.za/article/eskom-rolls-out-new-smart-meter-technology-to-fight-electricity-theft-2017-06-27, June 2017, (Accessed on 08/09/2018).

[4] J. Wattel, M. Tomlinson, J. Beukes, and T. Mouton, “Continuous line impedance assessment of lv feeders using smart meters,” in IEEE ISGT conf. rec., 2018.

[5] South Africa National Standards, “Earthing of low-voltage (lv) distributino systems,” Pretoria: SANS, Tech. Rep., March 2013.

[6] V. Cohen, “Loss of Neutral in Low Voltage Distribution Systems - Consequences and Solutions,” https://cbi-lowvoltage.co.za/sites/default/files/downloads/TechPapers/Loss%20of%20Neutral.pdf, July 2001, (Accessed on 10/08/2018).

[7] M. A. G. Mitolo, *Electrical Safety of LV Systems,*. New York: McGraw Hill, 2009.

[8] Eskom, “Meter tampering,” http://www.eskom.co.za/AboutElectricity/PubSafety/Pages/Meter.aspx, February 2016, (Accessed on 08/22/2018).

[9] Megger, “Getting down to earth,” http://www.weschler.com/_upload/sitepdfs/techref/gettingdowntoearth.pdf, February 2010, (Accessed on 10/08/2018).

[10] A. Cables, “airdac-sne-cable.pdf,” http://www.l-osales.co.za/download-catalogue/electric-cables/electrodac/airdac-sne-cable.pdf, August 2008, (Accessed on 10/27/2018).

[11] M. Mesganaw and K. Venkat, “Implementation of a three-phase electronic watt-hour meter using msp430f677x(a) (rev. g),” http://www.ti.com/lit/an/slaa577g/slaa577g.pdf, January 2013, (Accessed on 12/08/2018).

2019 SAUPEC/RobMech/PRASA Conference
Bloemfontein, South Africa, January 28-30, 2019

Power Tapping from HVDC Link: Utilization of Tap Point Information and Voltage Margin to Ascertain Proximity to Voltage Collapse

Agha Francis Nnachi
Electrical Engineering Department
Tshwane University of Technology
Witbank Campus, South Africa
nnachiaf@tut.ac.za

Josiah Lange Munda
Electrical Engineering Department
Tshwane University of Technology
Pretoria South Africa
mundajl@tut.ac.za

***Abstract*— Long distance point-to-point HVDC link which traverse rural dwelling places can be utilized for tapping power to feed those areas. However, the extent of power tapped if not curtailed can lead to voltage collapse of the system. In this paper, analysis of Voltage stability index (VSI) to ascertain the nearness of HVDC link to voltage collapse is presented. However, this VSI method needs constantly measuring the tap voltage and current to ascertain nearness to voltage collapse. Therefore, power tap limit as a function of tap point information such as the length of the link, tap point distance from the main converter station and voltage margin at any point along the HVDC link and optimum tap limit is proposed. Simulation of the proposed technique is carried out in Matlab/Simulink environment with a case study of Namibia/Zambia Caprivi link VSC HVDC system. The simulation results depict that when power tapped is above the derived limit, the DC-link bus voltage collapses. More so, Small and large disturbance voltage stability was also studied. Results also show that when power tapping is below tap limit, small and large disturbances do not have effect on the DC-link voltages, however, when power tapped is above limit, the disturbances lead to voltage instability.**

Keywords*— *HVDC, Power tapping, Voltage source converter, Voltage stability, voltage collapse

I. INTRODUCTION

High Voltage Direct Current (HVDC) transmission systems offer attractive applications such as long-distance bulk power delivery, asynchronous interconnection of two AC networks and voltage stabilization etc. [2]. Furthermore, research has shown the need for utilization of this HVDC link for voltage profile improvement in heavily loaded network [1], power taping to feed rural areas situated at the vicinity of this HVDC-link transmission corridor [3-10]. However, power tapping from existing HVDC link, if not controlled can lead to voltage instability of the system. Voltage stability has been a major issue in power system. Numerous works [11-13] have been done on voltage instability, voltage collapse and their corrective control techniques. Some other literatures, have developed several methods to envisage voltage collapse incidence on AC power system. Some of the methods are voltage collapse prediction indices such as power margin [15, 16], voltage collapse prediction index [18], impedance stability index [15], line index [17], bifurcation theory [14] and a voltage collapse index (VCI) technique [19].

The VCI, a method used to ascertain the proximity to voltage collapse proposed in [19] is adopted in this paper to determine the nearness of HVDC link operating towards voltage collapse. The technique utilizes local bus voltage and current magnitude. However, it requires continuous current and voltage measurement at the tap point.

Therefore, in this work, a technique is proposed using tap point information voltage margin to determine how close a HVDC link under power tapping is to voltage collapse.

II. VOLTAGE STABILITY INDEX ANALYSIS OF HVDC LINK DURING POWER TAPPING

As power system network operates, several disturbances can affect bus voltages and the system's ability to maintain steady acceptable voltages after such disturbances is termed voltage stability [20, 21]. These disturbances can be classified as large (faults, loss of generation, or circuit's contingencies) and small disturbances (incremental changes in system load) [20, 24]. If the power system loses the ability to maintain acceptable voltages, the network will experience severe drop in the bus voltage profile and if care is not taken, can lead to voltage collapse [22]. Voltage collapse which is a shutdown of a power system may be partial or total blackout [23].

For a HVDC system, the inverter control is used to regulate the DC-link voltage. Power tap-off along the transmission corridor therefore should have a limit not to mar the controllability of the converter link leading system voltage collapse. In order to analyse the voltage stability of a point-to-point HVDC with power tapping station along the DC-link, Fig 1 is used for this study. Power tapped at point *i* along the link can be determined using the equation:

$$P_{Tap\_i} = I_{Tap\_i} V_i \tag{1}$$

where
I_{Tap_i} is the tapped current tapped at point *i*
V_i is the voltage at tap point *i*

From (1), tap point voltage V_i will degrease when the current tapped $I_{Tap\ i}$ increase and vice versa whereas V_i decreases. If Taylor's theorem is applied in (1), incremental changes in P_{Tap} with respect to the incremental changes in $I_{Tap\ i}$ and V_i can be written as:

$$\Delta P_{Tap\_i} = \frac{\partial P_{Tap\_i}}{\partial I_{Tap\ i}} \Delta I_{Tap\_i} + \frac{\partial P_{Tap\_i}}{\partial V_i} \Delta V_i + higher\ order\ terms \tag{2}$$

Neglecting the higher order terms, (2) can be written as:

$$\Delta P_{Tap\ i} = V_i \Delta I_{Tap\ i} + I_{Tap\ i} \Delta V_i \tag{3}$$

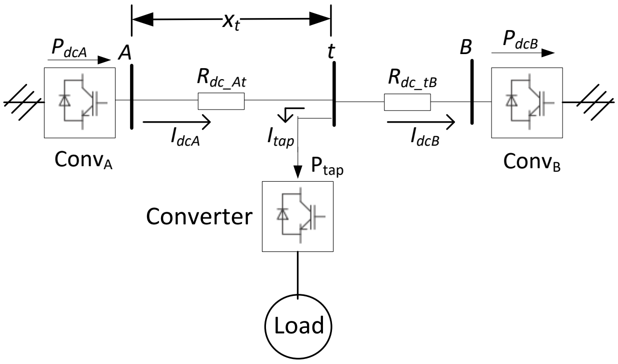

Fig. 1. Two-terminal HVDC with tapping station on the dc-link transmission

Equation (3) is a key to determine stability and will always remain positive when power tapped is within the voltage stability limit or voltage stability index (VSI). Therefore, to ensure DC-link voltage stability and avoiding voltage collapse, any change in power tapped should be such that

$$\Delta P_{Tap\ i} = V_i \Delta I_{Tap\ i} + I_{Tap\ i} \Delta V_i \geq 0 \tag{4}$$

To determine voltage stability index (VSI), equation (4) can divided by $V_i \Delta I_{Tap\ i}$ to get:

$$VSI = 1 + \frac{I_{Tap\_i} \Delta V_i}{V_i \Delta I_{Tap\ i}} \geq 0 \tag{5}$$

This VSI equation can therefore be used to give indication on how far the DC-link is from voltage collapse during power tapping. When there is no power tapped ($I_{Tap\ i} = 0$), *VSI* is unity and as power tapped increases, VSI deceases and becomes zero at voltage collapse point.

This technique is very simple as it requires only measurement of tapping current $I_{Tap\ i}$ and bus voltage V_i at two different points. However, this technique requires a cautious and continuous measurement and processing of the tapped current and voltage data to get VSI.

III. PROPOSED POWER TAP LIMIT DETRMINATION

From Fig. 1, if there is no power tapped, *PdcA* flows into bus-B and gives rise to a voltage drop between bus-A and bus-B. As power tapped at bus-t begins to increase, more voltage drop will begin to increase at the tapping point. If the power tapped continues to increase, a point will be reached when converter B can lose its DC voltage control. When this happens, the tap bus voltage can drop noticeably in such a way that the direction of power flow PdcB could begin to reverse. At this point when voltage begins to reverse is therefore used as the criterion for tapping limit determination. In [29], the proposed power tapping limit, utilising principle of uniform loading [25], [26], [27], [28], is analytically derived as:

$$-P_{tapx_t\_\text{limit}} = \frac{V_{dc\min}\left(V_{dc\min} - V_{dcref}\right)}{r x_t} + \frac{x_t}{2L} P_{dcA} \tag{6}$$

Where

$P_{tap\,x_t\_limit}$ is limit of power that can be tapped at point x_t (MW)

The negative signifies power tapping

P_{dcA} is the main VSC_A HVDC converter the reference power (MW)

V_{dcmin} is the control specified lower voltage regulation limit

V_{dcref} is the reference voltage,

$V_{dcmin} - V_{dcref}$ is K (the voltage margin)

$r = R/L$ = resistance per unit length of the DC-link;

x_t is tapping station distance from bus-*A*;

L = Total length of the DC-link;

From (6), the limit of the power that can be tapped depends on the control parameter settings of the main HVDC, point of tap-off and length of the transmission line and can be simplified as:

$$-P_{tapx_t\_\text{limit}} = \frac{V_{dc\min} K}{\frac{R}{L} x_t} + \frac{x_t}{2L} P_{dcA} \tag{7}$$

Taking $\frac{V_{dc\min}}{R} = P_{dcA}$ (base power)

then,

$$-P_{tapx_t\_\text{limit}} = \frac{P_{dcA} K L}{x_t} + \frac{x_t}{2L} P_{dcA} \tag{8}$$

With P_{dcA} as the base power, the per unit power-tap limit ε_{tap} at any point x_t is:

$$\varepsilon_{tap} = -\frac{P_{tapx_t\_\text{limit}}}{P_{dcA}} = \frac{KL}{x_t} + \frac{x_t}{2L} \tag{9}$$

Therefore, at any point on the DC-link, the tap limit is a function of the DC-link length, tap point and acceptable voltage margin. If Power is tapped above this established limit, the system will enter voltage instability condition and subsequently leads to voltage collapse. This equation (9) is therefore used to establish the proximity to voltage collapse of the HVDC under power tapping.

The optimum point of power tapping can be determined using the equation:

$$\frac{d\varepsilon_{tap}}{dx_t} = 0 \tag{10}$$

Hence, applying (10) to (9) gives:

$$\frac{d\varepsilon_{tap}}{dx_t} = \frac{-KL}{x_t^2} + \frac{1}{2L} \tag{11}$$

Therefore,

$$\frac{KL}{x_t^2} = \frac{1}{2L};\tag{12}$$

$$x_t = L\sqrt{2K}\tag{13}$$

Substituting (13) in (9), the optimum power that can be tapping at optimum point x_t is:

$$-\varepsilon_{tap\_optimum} = \frac{KL}{L\sqrt{2K}} + \frac{L\sqrt{2K}}{2L} = \frac{K\sqrt{2K}}{2K} + \frac{L\sqrt{2K}}{2L} = \sqrt{2K}\tag{14}$$

For a voltage margin K = 0.05, optimum power tapping,

$$\varepsilon_{tap\_optimum} = \sqrt{2\times 0.05} = 0.3162 p.u = 31.62\,\%\tag{15}$$

IV. SIMULATION CASE STUDY OF NAMIBIA/ZAMBIA CAPRIVI LINK VSC HVDC

To verify the proposed theoretical power tapping limit and voltage collaspe analysis, Namibia/Zambia Caprivi Link VSC HVDC is used as a case study. VSC HVDC is modelled in Matlab/Simulink environment with parameters of the Caprivi link [30], [31] shown in table 1 and converter vector classical control [32] applied. In the model, power tapping station located at the middle of the link. The performance of the HVDC under tapping power below and above limit is therefore demonstrated.

TABLE 1
SIMULATION PARAMETERS OF NAMIBIA/ZAMBIA CAPRIVI LINK VSC HVDC

Data	Parameters
HVDC link Power rating	300 MW
Namibia AC side voltage	400 kV
Zambia AC side Voltage	330 kV
DC link voltage	350 kV
Coupling transformer rating on both sides	315 MVA
Length of DC-link	950 km
Converter Switching frequency	1150 kHz

A. *Power tapped versus tap point*

Using equation (9), the per power tap limit at any point x_t on the DC-link is plotted as shown in Fig. 2. The per unit optimum power tapped ($\varepsilon_{tap\ optimum}$) which is 0.316 p.u occurs at 300 km from the main VSC_A converter. This per unit optimum power tapped will be different in other networks where there is a different voltage margin.

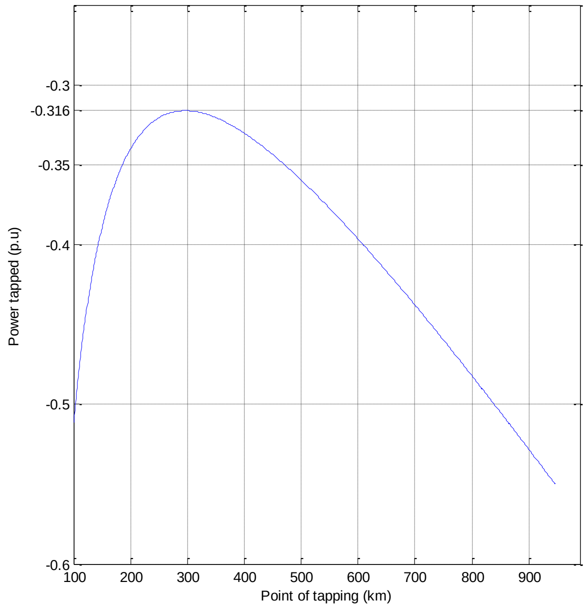

Fig. 2. Power tapped versus tap point xt

B. *Voltage stability index(VSI) versus power tapped*

In this case, the power tapped is increased uniformly by a load multiplier factor λ starting from 50 MW. The VSI is calculated accordingly and plotted against the load multiplier factor as shown in Fig. 3. As load factor increases, the index decreases and eventually approaches zero at voltage collapse point.

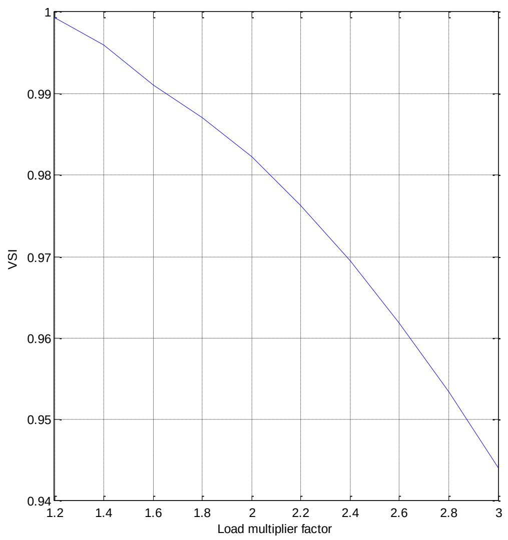

Fig. 3. Variation of VSI against power tapped

C. *System response at increasing power tapping*

Fig. 4 shows the responses of the power flow of the main VSC_A and VSC_B as the power tapped increases and Fig. 5 shows the responses of VSC_A, VSC_B and tap point bus voltages.

Secondly, the same scenario (small and large disturbances) is repeated but with power tapped more than tap limit. Fig. 7 is system DC bus voltages and power response which show severe oscillations and voltage instability.

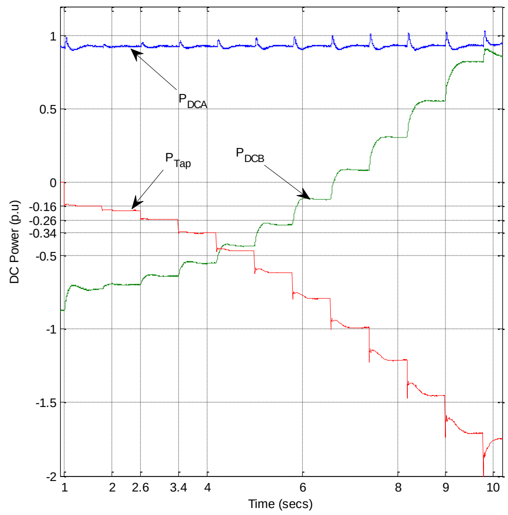

Fig. 4. DC bus power at increasing power tapping

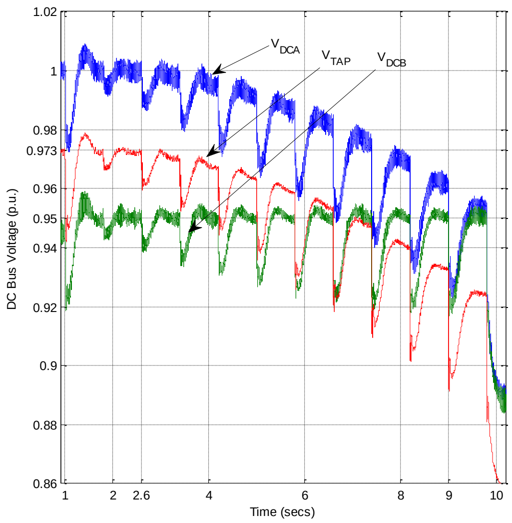

Fig. 5. Response of DC bus voltage at increasing power tapping

From Fig. 5, as the power tapped increases but below tap limit, the DC-bus voltage remained uninterrupted. This is due to the voltage regulation capability of the VSC_B converter. However, as the power tapped is close to tap limit at about 3.4 secs, V_{DCA} and V_{Tap} bus voltages begin to change hence entering state of voltage instability (a progressive and uncontrollable decline in voltage) [33,34] leading to voltage collapse.

D. Small and Large disturbance voltage stability

Firstly, the tap-station was initially off and at 1 sec it was switched in (small disturbance) with tapping power less than tap limit. At 1.89 secs, a fault (large disturbance) was applied. Fig. 6 shows the DC-bus power and voltage responses and both the small and large disturbances did not have much effect on the main system voltages and each bus power settled fast to their steady after the disturbances.

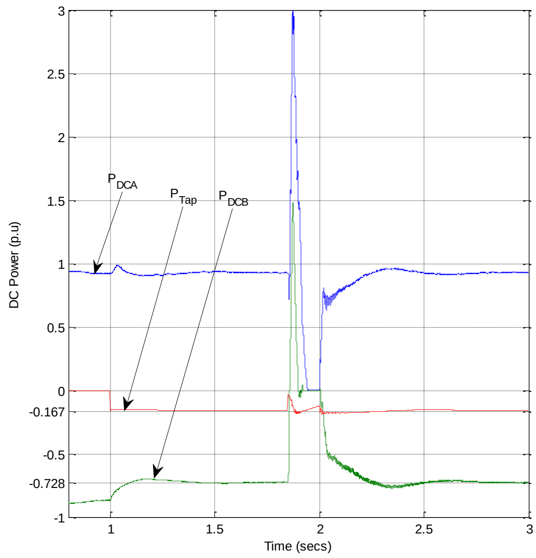

(a)

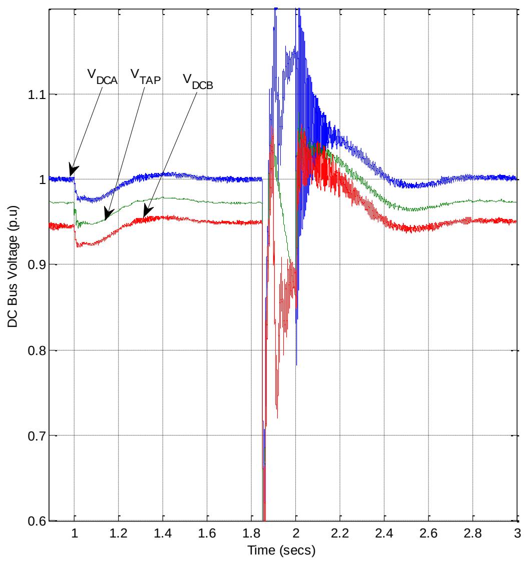

(b)

Fig. 6. System response when power tapping is below limit: (a) DC –Bus power (b) DC-bus voltages

carried out in Matlab/Simulink environment with Namibia/Zambia Caprivi HVDC link.

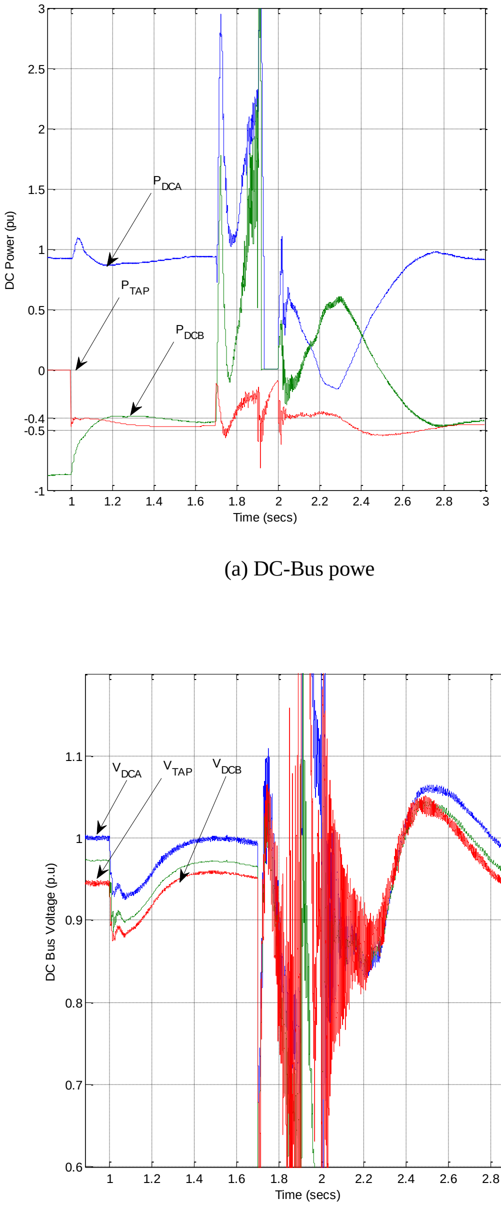

(a) DC-Bus powe

(b)

Fig. 7. System response when power tapping is above limit: (a) DC-Bus power (b) DC-Bus voltages

V. CONCLUSION

In this work, analysis of voltage stability and voltage collapse of an HVDC system with power tap-station on the DC-link is presented. The paper presents the utilization of voltage stability index (VSI) to determine distance to voltage collapse as power being tapped increases. Due to the challenges of continuous measurement to establish the index, an analytical technique of determining this distance to voltage collapse is proposed. This technique involves only the knowledge of tap point information such as length of DC-link, distance of Tap-station from main HVDC station and acceptable voltage voltage margin of the main HVDC control. The effectiveness of the proposed method is carried out in Matlab/Simulink environment with Namibia/Zambia Caprivi HVDC link.

VI. REFERENCES

[1] L. Yingpei, L. Ran, A novel control method for a VSC-HVDC system in a grid-connected wind farm. Turk J Elec Eng & Comp Sci 2015; 23:1558 - 1570.

[2] M.P. Bahrman, K. B. Johnson, The ABCs of HVDC transmission technologies. In: IEEE 2007 Power and Energy, March 2007; 5. pp. 32 - 44.

[3] A.F. Nnachi, J Munda, D.V. Nicolae, AM Mpanda, Transient stability analysis of VSC HVDC transmission with power injection on the DC-link. Turk J Elec Eng & Comp Sci 2015;23: 1834 - 1852.

[4] N. Ijumba, L. Chetty, Rural electrification using overhead HVDC transmission lines. J Energy Southern Africa 2012; 23: 45 - 50.

[5] L. Chetty, N. Ijumba, A. Britten, Parallel-Cascaded tapping station. In: Proceeding of IEEE International conference of Power System Technology, 21 -24 November 2004; Singapore.

[6] D. Jovcic, Bidirectional High-power DC Transformer. IEEE T Power Deliver 2009;24: 2276 - 2283.

[7] H. Rahman, B. Khan, Possibility of Power Tapping from Composite AC-DC Power Transmission Lines. IEEE T Power Deliver 2008; 23:1464 - 1471, 2008.

[8] B. Collet, J. Taisne, V. Arcidiacono, F. Mazzoldi, The Corsican Tapping: from design to Commission Test of the third Terminal of the Sardinia-Corsica-Ity HVDC Link. IEEE T Power Deliver 1989; 4: 794 - 799.

[9] J. Dohahaue, D. Fisher, B. Railing, P. Tatro, Performance testing of the Sandy Pond HVDC Converter. IEEE T Power Deliver 1993; 8:422 - 428.

[10] M. Bahrman, M Baker, J. Bowles, R. Bunch, J. Lemay, W. Long, J. McConnach, R. Menzies, J. Reeve, M. Szechtman, Integration of small taps into (existing) HVDC links. IEEE T Power Deliver 1995; 10:1699 - 1706.

[11] G. Huang, H. Zhang, Dynamic voltage stability reserve studies for deregulated environment. In Proceedings IEEE/PES Summer Meeting, 2001; Canada.

[12] R.A. Schlueter, A Voltage stability security assesment method. IEEE T Power Systems; 13:1423 - 1438, 1998.

[13] G.M. Huang, N.C. Nair, Voltage stability constraint load curtailment procedure to evaluate power system reliability measures. In: IEEE/PES Winter Meeting 2002, NewYork.

[14] J. Heydeman, S.C. Tripathy, G.C. Paap, L. Sluis, Digital and experimental study of voltage collapse and instability in power system. Int J Elec Power 2000; 22:303 -311.

[15] M. Bergovic, B. Milosevic, D. Novosel, A novel method for voltage instability. In: Proceedings of 35th Hawaii international conference on system science, 2002.

[16] D.E. Julian, R.P. Schultz, K.T. Vu, Quantance WH, Bhatt NB, Novosel D. Quantifying proximity to voltage collapse using the voltage instability predictor (VIP). In: Proceedings of IEEE PES summer Meeting, Seatle WA, 2000.

[17] M.H. Garng, NC Nirmal-Kumar, Detection of Dynamic Voltage Collapse. In: Power system engineering research centre, Winter Meeting, 2001.

[18] V. Balamourougan, T.S. Sidhu, M.S. Sachdev, Technique for online prediction of voltage collapse. In: IEE Proceedings-Genereration, Transmision and Distribution; 11 July 2004: pp.453-460.

[19] H.M. Haque, Use of local information to determine the distance to voltage collapse. Int J Emerg Elect Power 2008;9.

[20] P. Kundur, Power System Stability and Control. McGraw-Hill, 1994.

[21] C.T Van, C Vournas, Voltage stability of electric power systems. 1998.

[22] I. Kumaraswamy, W.V. Jahnavi, T. Devaraju, P. Ramesh, An optimal power flow (OPF) method with improved voltage stability analysis. In: Proceedings of the World Congress on Engineering, London, UK, 2012.

[23] D.P. Kothari, I.J. Nagrath, Modern power system analysis, McGraw-Hill, 2003.

[24] K. Prabha, P. John, A. Venkat, A. Goran, B. Anjan, C. Claudio, H. Nikos, H. David, S. Alex, T. Carson, V.C. Thierry, V. Vijay, Definition and classification of Power System Stability. IEEE T Power 2004; 19:1387 - 1401.

[25] B. Arijit, M. Arindam, H. Mark, S.E. Joe, Determination of allowable penetration levels of distributed generation resources based on harmonic limit considerations. IEEE T Power 2003; 18:619-624.

[26] M.N. Bandyopadhyay, Electrical power systems: theory and practice, PHI Learning Pvt. Ltd., 2006.

[27] C.L. Wadhwa, Generation, Distribution and Utilization of Electrical Energy, New Age International, 1989.

[28] S.N. Singh, Power generation: transmission and distribution, Prentice Hall India Pvt., Limited, 2008.

[29] A.F. Nnachi, J.L. Munda., D.V. Nicolae, M.A. Mpanda, Small power tapping limit on dc-link of VSC HVDC. In: IECON 2013 - The 39th Annual Conference of the IEEE Industrial Electronics Society, 10 – 13 November 2013; Vienna, Austria. IEEE. pp 2173 - 2177.

[30] T.G. Magg, M. Machen, E. Krige, H.D. Mutschler, J. Waborg, Caprivi Link HVDC Interconnector: The first VSC HVDC power transmission with overhead lines. In CIGRE SCB4 Meeting and Colloquium, 21, rue d'Artois, F-75008 PARIS, October 2011.

[31] C. Lennart, HVDC A Firewall against disturbances in high-voltage grid.

[32] P. Jiuping, N. Renaldo, T. Le, H. Per, VSC-HVDC Control and application in meshed AC network. In: IEEE-PES 2008 General meeting, 20 - 24 July 2008, Pittsburgh Pennsylvania, PA, USA.

[33] G. Murthy, B. Sivanarayana, R. Hanumantha. Voltage stability analysis of radial ditribution networks with distributed generation. Int J Elec Eng and Inform 2014;6: 195 - 204.

[34] M. El-Sadek, Power system voltage stability and power quality. Assuit Egypt: Mukhtar Press, 2002.

2019 SAUPEC/RobMech/PRASA Conference
Bloemfontein, South Africa, January 28-30, 2019

Battery Monitoring and Energy Forecasting for an Off-Grid Solar Photovoltaic Installation

William Becerra Gonzalez, James Braid, Sailen Nair

School of Electrical and Information Engineering, University of the Witwatersrand, Johannesburg

***Abstract*—This document details the design and implementation for an off-grid PV energy management system with key objectives being battery monitoring and energy forecasting. Coulomb counting is used to estimate the state of charge of a 24 V, 100 Ah lead-acid battery bank. An ACS712 hall effect current sensor module is used to implement the coulomb counter. A random forest regression model is used to predict solar irradiance with a root mean square error of 15.4%, when comparing actual Johannesburg irradiance data to predicted data. Energy forecasting is successfully done with a root mean square error of 6.2% for a three-day continuous test. It is concluded that the proposed solution successfully demonstrates a working principle for an energy management system, however, further improvements are needed to make the forecast model as accurate as possible.**

***Index Terms*—State of Charge, Energy Forecasting, Random Forest Regression**

I. Introduction

Solar power is one of the main sources of renewable energy across the world. It is especially appealing in South Africa due to the large amounts of solar irradiance that it receives (an average of 4.5 to 6.5 kWh/m^2 per day [1]), thus making photovoltaic (PV) off-grid solutions an attractive alternative. Using solar energy requires an energy storage solution with lead-acid batteries being a popular choice. Lead-acid batteries require proper monitoring and management to avoid issues such as gassing and sulfation that can severely damage the batteries. Having an off-grid system shifts energy management from corporations and public enterprises to the individual. The individual is often not aware of the capability of their off-grid energy system in sustaining the energy consumption for the foreseeable future.

This document aims to detail a working principle for an energy management solution that is not only able to monitor current energy levels but can also forecast energy for an off-grid system 24 hours in advance. Success is primarily based on the solutions ability to monitor live energy changes as well as forecasting the energy levels of the battery bank at hourly intervals throughout the day. The solution is intended to be used in regular households moving to an off-grid PV system and therefore practicality is also a measure of success.

One of the constraints of the project are the available batteries: since there is a finite number of cycles. This makes it difficult to assess the true health of the batteries and it is therefore assumed that the batteries' SoH are 100% at the start of the investigation and thus their capacity is assumed to be that of the manufacture's rated capacity. The SoC algorithm used is assumed to produce an accurate estimate of the current SoC of the battery bank.

II. Background

The key components of the Home Energy Management System (HEMS) can be broken down into the estimation of solar irradiance, the estimation of the SoC of a battery bank, and finally the integration of the various devices to form a complete HEMS.

A. Solar Irradiance

Prediction of solar irradiance is vital for the forecasting of energy within a battery bank. There are many methods to do this with most of the methods using some form of machine learning model. Bae *et al* [2] compares three different machine learning models to predict solar irradiance. Namley an Artificial Neural Network (ANN), a Non-linear Autoregressive Network (NAN) and a Support Vector Machine (SVM). The SVM model performed the best in that particular experiment.

Non-neural network machine learning models have been used successfully to predict solar irradiance. These models include SVM models as previously mentioned and Random Forest Regression models (RFR). Papers [3]–[5] use RFR models to forecast solar irradaince. Jain *et al* [4] compares the RFR model to five other machine learning models, with the random forest model performing the second best. It is seen that the performance differences between neural networks and non-neural network machine learning models, in predicting solar irradiance, are marginal. Therefore the machine learning model for the proposed HEMS follows an RFR model trained on historical data.

B. Battery Monitoring

Monitoring a battery consists primarily of monitoring the energy flow to accurately estimate the State of Charge (SoC) of the battery. This can be achieved by modelling the lead-acid battery's characteristics. Factors such as temperature, internal resistance, capacity, aging, efficiency and discharge rate need to be considered. These factors do not remain constant and their value is functionally dependent on the other factors, thus making it challenging to accurately model a battery. For example, the value of efficiency is dependent on the temperature as well as the aging of the battery. Similarly, the capacity of the battery is dependent on aging as well as the discharge rate.

The estimation of SoC of the battery bank plays a pivotal role in the forecasting of energy for 24 hours. An accurate model is needed to estimate the current SoC of the battery bank. Three main methods exist for this estimation:

978-1-7281-0368-6/19/$31.00 ©2019 IEEE

measuring the Open Circuit Voltage (OCV) of the battery bank, measuring the specific gravity of the solution of each battery, and coulomb counting.

Paper [6] provides a method to estimate the state of charge of lead-acid batteries based on their OCV and measuring the specific gravity of the electrolyte solution. One of the main drawbacks of these two methods is that they can not be implemented in an active system (system that is in a continuous charge / discharge state). The OCV method requires that the batteries be at rest for several hours before an accurate measurement can be observed.

Coulomb counting is a method to estimate the SoC of a battery bank in an active system; it measures the amount of energy going into the battery bank versus the amount of energy leaving the battery bank over a period of time. This method has been used in the HEMS constructed. Papers [7] and [8] make use of coulomb counting to estimate the state of charge of an active system. Kumar *et al* [7] uses a current integration method over a specified time interval to compute the number of coulombs that have either left the battery or entered the battery. It is observed that the SoC estimation algorithm needs to be recalibrated throughout the lifespan of the battery bank, due to its decline in health (SoH) with time and use. In order to calibrate a coulomb counting system, the float charging current of a lead-acid battery can be used. Floyd *et al* [9] determined that by measuring the float current of a battery, an SoC of 100% could be evaluated accurately.

III. System overview

A functional block diagram of the entire system is shown in Figure 1. The flow of control as well as the flow of power is shown along with the different points of current measurement.

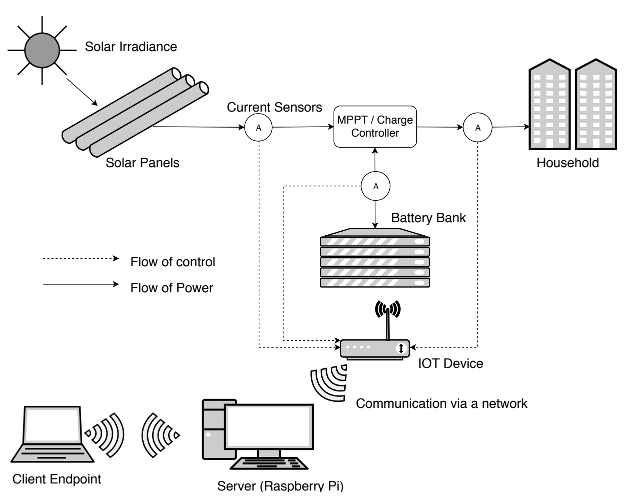

Fig. 1. Complete system overview showing flow of control and power.

A. System Specifications

The system comprises of the following components:

- Initially two 90 W solar panels were used; later during the investigation two 260 W solar panels were used. The panels were placed flat on the roof.
- Two 12 V, 100 Ah Sealed Lead-Acid (SLA) batteries connected in series.
- A Steca Solarix MPPT charge controller.
- One Siemens SIMATIC IoT2020 device.
- One Raspberry Pi 3B (Server).
- Three hall effect current sensors.

B. Estimation of Batteries State of Charge

The estimation of the battery bank SoC is a vital part of the system. As mentioned in Section II, conventional methods of measuring SoC such as OCV and specific gravity can not be implemented within an active system. Coulomb counting is therefore chosen to estimate the SoC. Coulomb counting consists of monitoring the charge flow into and out of the battery bank and can be defined by Equation (1) [8], where $SoC_{(t)}$ is the current state of charge of the battery bank, $SoC_{(t+1)}$ is the state of charge of the battery bank at the next time interval, C_a is the rated capacity of the battery bank and i is the measured current.

$$SoC_{(t+1)} = SoC_{(t)} + \frac{\frac{i}{3600}}{C_a} * 100 \tag{1}$$

Within the final system the SoC calculation is updated every second. This short time interval allows for any random spikes in current to have a negligible affect on the overall SoC calculation.

To measure the current, ACS712 hall effect current sensors are used. These sensors are accurate with a total output error of 1.5%. The accuracy of coulomb counting depends on the accuracy of the current measurement device as well as a known SoC at the start of the coulomb counting process.

The SoC estimation error of the coulomb counting method is accumulated over time. This error is caused by two main factor: firstly, the error introduced by the current measurement system and secondly the efficiency of the batteries implies that one coulomb into the battery does not translate to one coulomb stored. The actual charge stored is the aggregation of the coulombs into the battery multiplied by its efficiency. Furthermore, this efficiency is varying depending on the operating conditions of the battery as well as the aging effect. The charging efficiency of the battery is known as the Round Trip Efficiency (RTE). The RTE for a lead-acid battery is typically 80%, however, that value can vary depending on various factors such as temperature and discharge rate. For simplicity the RTE of the battery bank is assumed to be 80% during all phases of charging.

The SoC of the battery bank ranges from 0 to 100% where 0% correlates to the 50% Depth of Discharge (DOD) point of the battery bank. This was done to ensure that the lead acid batteries are not put into a deep discharge, which can reduce their lifespan significantly.

C. State of Health of Batteries

The health of a lead-acid battery deteriorates constantly, meaning that their maximum capacity of energy that each battery can hold decreases over each charge / discharge cycle. This leads to inaccurate SoC estimations due to the reference capacity constantly decreases, albeit at a slow rate. However, over time the estimation error can grow significantly. Hence the SoC estimation model needs to be recalibrated to include the latest maximum capacity of the battery bank. The measured capacity of a lead-acid battery compared to the manufactures rated capacity can be used as an indication to the SoH of the battery.

The general metrics used to measure SoH of batteries are the internal resistance and their capacity versus the rated capacity [8]. SoH based on capacity is given by Equation (2), where C_a is the current capacity of the battery and C_r is the rated capacity of the battery. A lead-acid battery is deemed to have reached its end-of-life when the current capacity drops to 80% of its rated capacity. It is recommended that an analysis of the SoH of the batteries be done every 6 to 8 weeks to ensure that the SoC estimation is always as accurate as possible.

$$SoH = \frac{C_a}{C_r} * 100\% \tag{2}$$

The recalibration of the SoC is done by measuring the float-charge current of the lead-acid battery (the third and final stage of charging). During the float-charge state of charging, the lead-acid batteries are at their maximum capacity, hence the SoC can be updated with the latest battery bank capacity. According to IEEE standards [10] the float current is determined by measuring the same float charge current of the battery bank for three consecutive hours. The shutting down of the system for several hours, to allow for the recalibration of SoC and overall estimation of SoH, is a compromise that a user will have to endure. This compromise is to ensure that the estimation of SoC remains as accurate as possible.

D. Solar Irradiance Prediction

One of the key components to forecasting the SoC of the battery bank, is the prediction of the solar irradiance. The solar irradiance predicted is that of Global Horizontal Index (GHI), hence the panels were positioned flat on a rooftop and were not tilted. To predict solar irradiance for 24 hours (at hourly intervals), a RFR machine learning model is used. RFR algorithms are powerful machine learning models that are simple to construct and perform well for most regression / classification tasks. When compared to a SVM model, the RFR model proved to be better. The RFR model builds a set number of decision trees based on the features that the model is trained on. For a regression problem, the outcome of all the decision trees are then averaged to obtain the final predicted value.

1) Training and Testing Dataset: The machine learning model was trained using historical meteorological data for Pretoria. The data used comprised more than three years of weather data (September 2013 to July 2017). Weather data from Pretoria was used as not enough historical data was available for Johannesburg. The model was trained on four features (the input data) and one label (the output data). The features comprised: air temperature, relative humidity, time-of-day and day-of-year and the output feature comprised the GHI. One of the key characteristics of the choice of the RFR algorithm is its low computational needs when compared to neural networks. The final RFR model was trained on a Raspberry Pi 3B and comprised of 150 decision trees.

2) Model Testing: The historical data used to train the model was split: 80% of the data was used to train the model and 20% of the data was used to test it. The performance metrics of the model can be seen in Table I, where R^2 represents a "goodness of fit" metric. The 94% value shows how closely the predicted values lie to the regression line. The high density of data points close to the regression line seen in Figure 2 can confirm this result. Root Mean Square Error (RMSE) and Mean Absolute Error (MAE) are the other chosen error metrics and have units of W/m^2. It is seen that the RMSE value is relatively high, however for the given system, the RMSE of the predicted solar irradiance equates to 15.6 W/M^2 error at the output of the panels.

TABLE I
REGRESSION METRICS FOR THE TRAINED RFR MODEL

Metric	Result
R^2	94%
RMSE	74 W/m^2
MAE	36 W/m^2

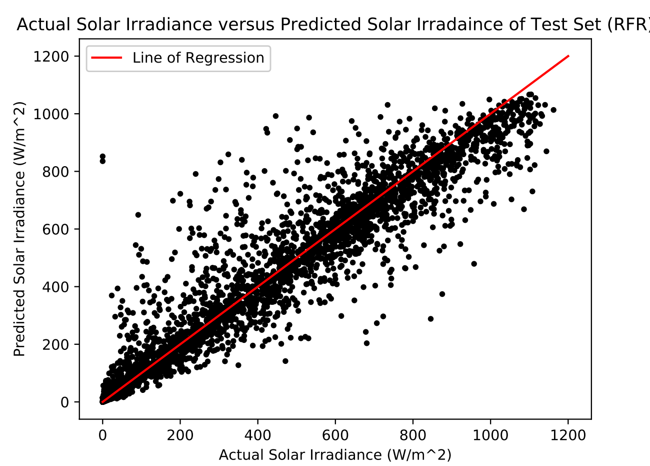

Fig. 2. Actual solar irradiance compared to the predicted solar irradiance for the test dataset. The line of regression signifies perfect match.

3) Testing model on Johannesburg Data: The prediction model was tested against actual solar irradiance data from Johannesburg, which was measured using a pyranometer. The results were taken for several days, with one day's worth of data shown in Figure 3. The graph shows the predicted solar irradiance and the actual solar irradiance. It is seen that the RFR model over predicts the solar irradiance toward the afternoon. The RMSE value between the predicted and the actual irradiance is 15.4%. This is the trend observed over multiple days of tests. Possible reasons for this over prediction could be due to the location difference between Johannesburg and Pretoria, as their latitude differs by 0.47 degrees. Furthermore the RFR model may need to be trained with a larger dataset so as to account for the over prediction.

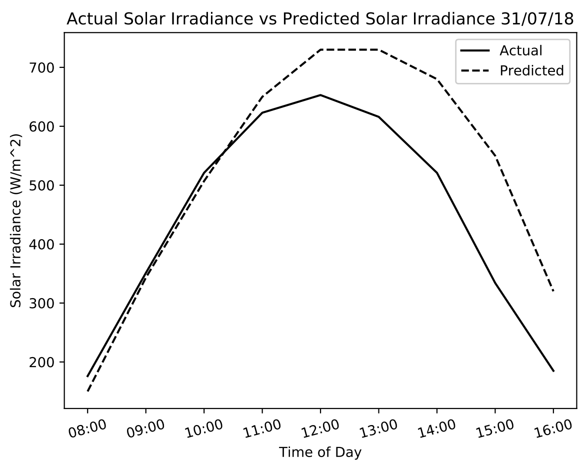

Fig. 3. Actual and predicted solar irradiances for Johannesburg versus time.

E. Power Output of Solar Panels and SoC Estimation

Knowing the solar irradiance that the sun will provide in advance allows for the estimation of the expected power output of the PV array using Equation (3) [11].

$$P_{out} = \eta * I * A * PR \tag{3}$$

Where P_{out} is the output power of the panels, η is the efficiency of the solar panels, I is the solar irradiance, A is the area of the solar panels and PR is the power ratio which takes into account the RTE of the system. The RTE is assumed to be a constant 80% as mentioned in Section III-B. The power output of the panels is assumed to be constant for the entire hour.

Using the 24 hour predicted solar irradiance, the expected power output of the solar panels for 24 hours can be calculated. This array of values is then used in Equation (4) to estimate the battery's stored energy in Wh, where $E_{Bat(t)}$ is the energy within the battery bank at time t, $E_{out(t)}$ is the energy output from the solar panels for an hour and $E_{load(t)}$ is the energy delivered to the load. For simplicity, a load profile is predetermined and is shown in Figure 4. The SoC of the battery bank can then be calculated using Equation (5), where E_{Bat_rated} is the rated capacity of the batteries in Wh.

$$E_{Bat(t+1)} = E_{Bat(t)} + E_{out(t+1)} - E_{load(t+1)} \tag{4}$$

$$SoC = \frac{E_{Bat}}{E_{Bat\_rated}} * 100 \tag{5}$$

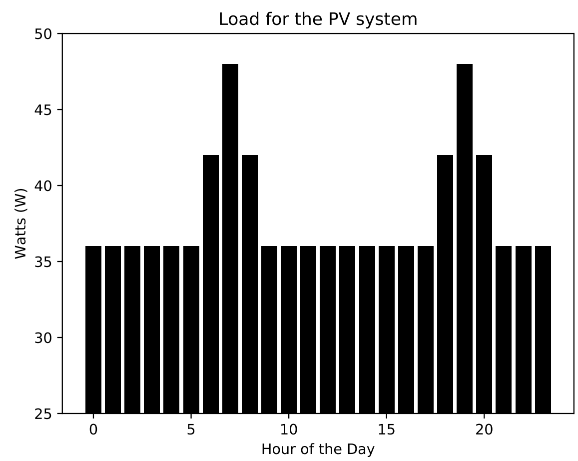

Fig. 4. Predetermined load profile.

F. Data Acquisition and Data Presentation

The main software for the system is executed on the Raspberry Pi server. A high level block diagram of the software system is presented in Figure 5. The software is executed once an hour; this ensures that the SoC predictions are updated every hour. The weather Application Programming Interface (API) of choice is openweathermap.org, from here a 24 hour forecast of temperature as well as relative humidity is retrieved. The forecast is then used as the input data for the RFR model to predict the solar irradiance. Once the solar irradiance is predicted, Equations (3) to (5), are used to estimate the SoC for the next 24 hours.

A Siemens SIMATIC IOT2020 device is used as a data acquisition unit that reads the current sensors' outputs. The current readings are sampled every second and sent to a Raspberry Pi based server using the Message Queuing Telemetry Transport (MQTT) network protocol. The server runs the Mosca MQTT broker; this protocol was chosen for its lightweight properties as it was designed for Internet of Things (IoT) applications. The Raspberry Pi 3B was chosen as the server because it is relatively inexpensive and powerful enough to train the machine learning algorithm, run the prediction model, and display the front-end Graphical User Interface (GUI).

A Node-Red server application is used to present the

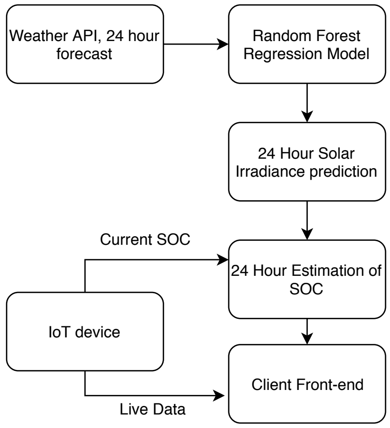

Fig. 5. Block diagram illustrating the software implementation.

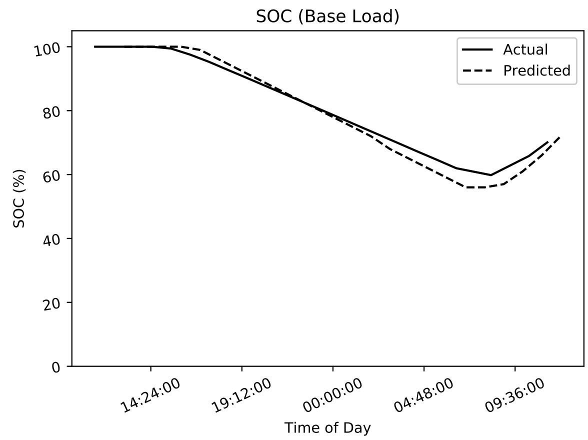

Fig. 6. Predicted SoC and Actual SoC over a 24 hour period.

information to the end user. The interface is accessible through the IP address of the Raspberry Pi server. Node-Red is lightweight and simple to use with most IoT functionality pre-implemented. The Node-Red server receives the measured current data sent from the SIMATIC IOT2020 unit. This data is used to perform coulomb counting and calculate the current SoC. The current SoC is used to perform energy forecasting as previously discussed.

IV. Results

The complete system was tested over several days with different loads and solar panel configurations. The results from the two tests conducted are shown in Table II, where the calculated RMSE value is used as an indicator of accuracy. The maximum deviation is defined as the highest error that can be detected between the predicted curve and actual value curve.

TABLE II
Table of results

Test	Duration (hours)	Panel Wattage (W)	Load Wattage (W)	RMSE	Maximum Deviation
1	24	2 * 90	35	4.72%	11%
2	72	2 * 260	Varying between 35, 41, and 47	6.20%	14%

The first test conducted comprised two 90 W panels with a single known load of 35 W. The system's initial SoC was set to 100%, with the system being run over a 24 hour period. Figure 6 shows the forecasted SoC versus the actual SoC. The RMSE between the actual and predicted SoC is calculated to be 4.72%. This RMSE value corresponds to the SoC percentage. The maximum deviation between the actual and the predicted SoC is 11%.

The second test conducted comprised two 260 W panels configured in parallel with a known variable load shown in Figure 4. The initial SoC of the system was set to 100%. The system was set to run for 72 hours continuously. Figure 7 shows the forecasted SoC as well as the actual SoC. The times at which the forecast was taken are illustrated through the three large dots on the graph. The RMSE of the 3-day forecast is 6.2%, where this percentage relates to an actual SoC percentage. The maximum deviation between the actual and predicted SoC is measured to be roughly 14%. This maximum difference occurs after the 85% SoC mark.

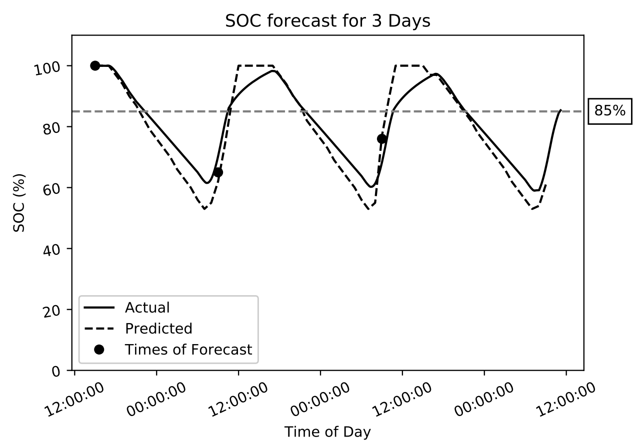

Fig. 7. Predicted SoC and Actual SoC for the 72 hour test.

The trend of the forecasted SoC follows closely to the actual SoC. The largest margin of error for the forecast is seen to be above the 85% SoC mark, which is denoted on the graph by the horizontal dashed line. The forecasted model fails above the 85% mark due to the inability of the model to take into account the non-linearities involved in the last stages of charging (i.e absorption charging and trickle charging). In the final stages of charging, the lead-acid batteries' charge efficiency drops significantly and thus charges at a much slower rate than usual. Therefore there is a large deviation after the 85% SoC point. Below the 85% SoC mark the forecasted model does follow the actual SoC closely, with the forecasted model tending to predict a lower SoC than the actual.

It is key to note that weather conditions throughout all tests remained relatively constant, with no significant cloud cover, wind or rain.

V. Critical Analysis

The forecasting model is seen to forecast the SOC within a RMSE value of 6.2%. This shows that the model can, within some error bounds, forecast SoC for an off-grid solar PV system. This RMSE is for constant weather; the model was not tested in varying weather conditions and thus a complete recommendation to the success of the system cannot be made.

The monitoring of the battery bank state-of-charge was achieved. However, there was no validation performed to confirm how accurately the coulomb counting method modelled the battery banks SoC. Possible methods of validation could have been performed such as comparing the SoC using coulomb counting to OCV. The OCV is determined using the terminal voltage readings and the Thevenin equivalent model of the battery bank. The overall battery model used is simplistic at best as it does not account for factors such as operating temperature, de-rating of the battery bank, effects of discharging rate, and non-linear charging stages (i.e. absorption and trickle charging). A self-calibration method based on float current is discussed, however, it could not be tested. This method requires the battery bank to stabilise on float current and remain unchanged for three hours which is unlikely to occur for a battery under continuous operation.

One of the main weaknesses of the complete system is the solar irradiance prediction model. The model does not perform accurately enough with an RMSE value of 15.4%. This is largely due to the model being trained using Pretoria weather data and not data for Johannesburg. The over prediction of solar irradaince did not seem to affect the tests conducted, however it could affect the SoC predictions during varying weather conditions such as overcast conditions.

Despite the drawbacks of the implementation, the system successfully depicts a working principle of an energy monitoring system that can forecast energy. The practicality of the implementation can be assessed by noting that the energy monitoring system can be installed into already existing off-grid systems as it only requires a data acquisition unit and three key sensing points. The Raspberry Pi server demonstrates the low computational needs of the system. Therefore, the implementation is deemed successful.

VI. Future Improvements

To increase the accuracy of the solar irradiance prediction, historical weather data for the location of the HEMS installation should be used to train the machine learning model. The current HEMS does not actively assess the SoH of the battery bank. The HEMS should actively monitor the SoH of the battery bank, as well as recalibrate the SoC estimation to account for the derating of the battery bank.

The modelling of the final stages of charging of lead-acid batteries should be improved upon so as to increase accuracy above 85% SoC of the battery bank. Finally a machine learning model to learn the load profile of a house should be implemented. This will help to learn and predict load profiles for different days of the week as well as for the different seasons of the year.

VII. Conclusion

This paper has shown the design and implementation of a Home Energy Management System (HEMS). Coulomb counting has been used to estimate the SoC of the battery bank. The machine learning model designed to predict solar irradiance is shown to over predict solar irradiance towards the afternoon for Johannesburg. The entire system is seen to forecast the SoC with an RMSE value of 6.2%. The model does, however, lose accuracy after the 85% SoC mark. The system can be viewed as a viable means to predict SOC, however, improvements are needed to ensure the model is robust and is able to work in all conditions.

References

[1] Renewable Energy, http://www.energy.gov.za/files/esources/renewables/r solar.html, Last Accessed September 2018

[2] K. Y. Bae, H. S. Jang and D. K. Sung, "Hourly Solar Irradiance Prediction Based on Support Vector Machine and Its Error Analysis," in IEEE Transactions on Power Systems, vol. 32, no. 2, pp. 935-945, March 2017.

[3] M. Abuella and B. Chowdhury, "Random forest ensemble of support vector regression models for solar power forecasting," 2017.

[4] D. Jain and M. Lalwani, "A comparative study of prediction of hourly slope irradiation," 2017.

[5] L. Benali, G. Notton, A. Fouilloy, C. Voyant, R. Dizene, Solar Radiation Forecasting using Artificial Neural Network and Random Forest Methods: Application to Normal Beam, Horizontal Diffuse and Global Components, Renewable Energy, 2018

[6] D. J. Deepti and V. Ramanarayanan, "State of charge of lead acid battery," 2006 India International Conference on Power Electronics, Chennai, 2006, pp. 89-93.

[7] K. S. R. Kumar, V. V. Sastry, O. C. Sekhar, D. K. Mohanta, D. Rajesh and M. P. C. Varma, "Design and fabrication of coulomb counter for estimation of SOC of battery," 2016, pp. 1-6.

[8] G. L. Bressanini, T. D. C. Busarello and A. Pres, "Design and implementation of lead-acid battery state-of-health and state-of-charge measurements,", 2017, pp. 1-6.

[9] K. D. Floyd, Z. Noworolski, J. M. Noworolski and W. Sokolski, "Assessment of lead-acid battery state of charge by monitoring float charging current," 1994,

[10] IEEE Recommended Practice for Maintenance, Testing, and Replacement of Vented Lead-Acid Batteries for Stationary Applications," 25 Feb. 2011

[11] J. Braid, "Off-grid domestic water heating from solar and wind power: A feasibility study," AFRICON 2015, Addis Ababa, 2015, pp. 1-5.

2019 SAUPEC/RobMech/PRASA Conference
Bloemfontein, South Africa, January 28-30, 2019

Comparative analysis of life estimation and reliability of power transformers

Thuthukani G.L. Maduna, Agha F. Nnachi, Aloys O. Akumu, Bolanle T. Abe,
Electrical Engineering Department,
Tshwane University of Technology
eMalahleni, South Africa
gmaduna@mpact.co.za, nnachiaf@tut.ac.za, akumuao@tut.ac.za, abebt@tut.ac.za

***Abstract*— Due to large amount of power transformers and the need to reduce process downtime in the paper making mill, a life assessment of these power transformers is necessary to ensure continuity of supply. Several models have used to estimate the life time and reliability of transformers but in this paper, Furan analysis and Weibull distribution method is utilized and compared for ten representative transformers. From the furan analysis, the degree of polymerization (DP) in each of the transformer oil was calculated using Chendong's formula. The results were then used to determine the used life of the transformers. Then Weibull distribution method was used to determine the reliability and service life of each of the transformers. The reliability was then used to calculate the remnant life of the transformers. The Weibull analysis gave reliable results and the discrepancy in the furan analysis method shows that proper maintenance e.g. oil purification can increase the life expectancy of transformer. It is therefore recommended not to use only the Furan method when estimating the life of power transformers.**

Keywords*— *Degree of polymerization, dissolved gas analysis, furan, 2-furfuraldehidyde, reliability, remnant life.

NOMENCLATURE

CDF	Cumulative distribution function
CO	Carbon monoxide (ppm)
CO_2	Carbon dioxide (ppm)
DP	Degree of polymerization
DGA	Dissolved gas analysis
2FAL	2-furfuraldehidyde (μg/kg)
IEEE	Institute of electronics and electrical engineers
PD	Partial discharge
TCS	Transformer Chemistry Services
β	The shape parameter
α	The characteristic life time

I. INTRODUCTION

One of the essential part of electrical reticulation of a paper making mill is power transformers. They are very expensive and therefore require systematic maintenance. Failure of these transformers is one of the frequent causes of long downtime with detrimental impact on the system reliability and loss of revenue [1]. To enhance the reliability of the reticulation system, early detection of all possible causes of failure in any part of the transformer and its remaining life is very important [2]. Special paper and wood are used for insulation and internal structural support of transformer winding [3] and the colour of the paper can give an indication of the remaining life of a power transformer. The discoloration of the paper insulation is caused by the different stresses that the power transformer is subjected to under normal operation.

The oil of a power transformer can give a detailed assessment into the overall condition of the transformer. Therefore, an oil sample is taken once a year and different types of test are conducted to know the health of the power transformer. The test conducted will basically include the following test; Transformer internal condition: Dissolved Gas analysis (DGA), Transformer insulating oil condition, Transformer insulation paper condition and Transformer external condition.

The purpose of this paper is to utilize oil sample test data of ten transformers and analyze and compare their life estimation and reliability using Furan and Weibull distribution technique.

II. AN OVERVIEW AND USEFUL APPLICATION OF FURAN AND WEIBULL DISTRIBUTION IN DETERMINING THE RELIABILITY AND REMNANT LIFE

A. Life estimation using degree of polymerization from furan analysis

Furan compounds are present in transformer oil during insulation aging process. The taking of oil samples can indicate the amount of these compounds in transformer oil thereby giving an indication of the state of insulation paper [4][5][6][7]. The Chendong formula amongst a few has been developed to express the relationship between furans and DP. The DP will aid in calculating and estimating the used and remnant life of a transformer. Formulas (1) (2) and (3) is used for this assessment [5][6][7] as follows:

$$DP = \frac{log_{10}(2FAL) - 1.51}{-0.0035} \tag{1}$$

$$\%Life\ used = \frac{\log_{10}(DP) - 2.903}{-0.006021} \tag{2}$$

$$Elapsed\ life(in\ years) = 20.5 \ln\left(\frac{1100}{DP}\right) \tag{3}$$

Thirty-four oil samples were taken from thirty-four transformers which were analyzed by Transformer Chemistry Services (TCS) for dissolved gas analysis, transformer insulating oil condition, transformer insulating paper condition and transformer external condition.

The advantage of oil sample analysis is that all the tests can be conducted, and life predicted without taking the transformer out of service. Only ten transformers were

978-1-7281-0368-6/19/$31.00 ©2019 IEEE

assessed for this exercise. The tables below show the DGA and Furan test results from the ten transformers' oil samples.

Table I: TE44 oil sample test results

Transformer number: TE44			
Voltage	**6.6kV/550V**	**VA rating**	**1500 kVA**
Vector group	**Dy11**	**Tap changer**	**On load**
Impedance	**5.7**	**Consevator**	**Yes**
Installation date	**1937**	**Oil type**	**Mineral**
Transformer internal condition: Dissolved Gas (DGA) vpm @ NTP			
Hydrogen	H2	14	> 1000
	O2	17479	> 0.5%
	N2	95459	N/A
	CH4	12	> 80
	CO	291	> 1000
	CO2	10344	> 15000
	C2H4	20	> 100
	C2H6	17	> 350*
	C2H2	0	> 70
	C3H8		
Total % Gas		12.36	
Total Gas Combustible		354	*Age compensated
Transformer insulating paper condition			
2FAL		1.7783	
FURAN		2.989	
Water in paper: % Dry Weight			2.0 (max)
Water in paper: Total litres			

Table II: TK25/4 oil sample test results

Transformer number: TK25/4			
Voltage	**525V/400V**	**VA rating**	**100 kVA**
Vector group	**Dyn11**	**Tap changer**	**On load**
Impedance	**4.45**	**Consevator**	**No**
Installation date	**1977**	**Oil type**	**Mineral**
Transformer internal condition: Dissolved Gas (DGA) vpm @ NTP			
Hydrogen	H2	0	> 1000
	O2	11962	> 0.5%
	N2	73961	N/A
	CH4	2	> 80
	CO	52	> 1000
	CO2	3067	> 15000
	C2H4	3	> 100
	C2H6	1	> 350*
	C2H2	0	> 70
	C3H8		
Total % Gas		8.9	
Total Gas Combustible		58	*Age compensated
Transformer insulating paper condition			
2FAL		3	
FURAN		5.199	
Water in paper: % Dry Weight			2.0 (max)
Water in paper: Total litres			

Table III: TE21 oil sample test results

Transformer number: TE21			
Voltage	**6.6kV/550V**	**VA rating**	**2000 kVA**
Vector group	**Dy11**	**Tap changer**	**On load**
Impedance	**5.66**	**Consevator**	**Yes**
Installation date	**1985**	**Oil type**	**Mineral**
Transformer internal condition: Dissolved Gas (DGA) vpm @ NTP			
Hydrogen	H2	26	> 1000
	O2	20299	> 0.5%
	N2	68109	N/A
	CH4	2	> 80
	CO	53	> 1000
	CO2	1936	> 15000
	C2H4	8	> 100
	C2H6	2	> 350*
	C2H2	0	> 70
	C3H8		
Total % Gas		9.04	
Total Gas Combustible		91	*Age compensated
Transformer insulating paper condition			
2FAL		0.676	
FURAN		1.084	
Water in paper: % Dry Weight			2.0 (max)
Water in paper: Total litres			

Table IV: TE23 oil sample test results

Transformer number: TE23			
Voltage	**6.6kV/550V**	**VA rating**	**2000 kVA**
Vector group	**Dy11**	**Tap changer**	**Off load**
Impedance	**5.69**	**Consevator**	**Yes**
Installation date	**1977**	**Oil type**	**Mineral**
Transformer internal condition: Dissolved Gas (DGA) vpm @ NTP			
Hydrogen	H2	13	> 1000
	O2	17074	> 0.5%
	N2	34616	N/A
	CH4	3	> 80
	CO	22	> 1000
	CO2	1953	> 15000
	C2H4	9	> 100
	C2H6	4	> 350*
	C2H2	0	> 70
	C3H8		
Total % Gas		5.37	
Total Gas Combustible		51	*Age compensated
Transformer insulating paper condition			
2FAL		0.2296	
FURAN		0.351	
Water in paper: % Dry Weight			2.0 (max)
Water in paper: Total litres			

Table V: T2 oil sample test results

Transformer number: T2			
Voltage	**88kV/6.6kV**	**VA rating**	**20 MVA**
Vector group	**YNd1**	**Tap changer**	**On load**
Impedance	**11**	**Consevator**	**Yes**
Installation date	**1992**	**Oil type**	**Mineral**
Transformer internal condition: Dissolved Gas (DGA) vpm @ NTP			
Hydrogen	H2	10	> 1000
	O2	19066	> 0.5%
	N2	60073	N/A
	CH4	1	> 80
	CO	40	> 1000
	CO2	594	> 15000
	C2H4	3	> 100
	C2H6	1	> 350*
	C2H2	0	> 70
	C3H8		
Total % Gas		7.98	
Total Gas Combustible		55	*Age compensated
Transformer insulating paper condition			
2FAL		0.1427	
FURAN		0.213	
Water in paper: % Dry Weight			2.0 (max)
Water in paper: Total litres			

Table VI: T1 oil sample test results

Transformer number: T1			
Voltage	**88kV/6.6kV**	**VA rating**	**20 MVA**
Vector group	**YNd1**	**Tap changer**	**On load**
Impedance	**11.6**	**Consevator**	**Yes**
Installation date	**1994**	**Oil type**	**Mineral**
Transformer internal condition: Dissolved Gas (DGA) vpm @ NTP			
Hydrogen	H_2	10	> 1000
	O_2	9674	> 0.5%
	N_2	75517	N/A
	CH_4	10	> 80
	CO	98	> 1000
	CO_2	2603	> 15000
	C_2H_4	5	> 100
	C_2H_6	25	> 350*
	C_2H_2	0	> 70
	C_3H_8		
Total % Gas		8.8	
Total Gas Combustible		157	*Age compensated
Transformer insulating paper condition			
2FAL		0.7753	
FURAN		1.254	
Water in paper: % Dry Weight			2.0 (max)
Water in paper: Total litres			

Table VII: TE40 oil sample test results

Transformer number: TE23			
Voltage	**6.6kV/550V**	**VA rating**	**1500 kVA**
Vector group	**Dy11**	**Tap changer**	**Off load**
Impedance	**5.06**	**Consevator**	**Yes**
Installation date	**1962**	**Oil type**	**Mineral**
Transformer internal condition: Dissolved Gas (DGA) vpm @ NTP			
Hydrogen	H_2	1701	> 1000
	O_2	16801	> 0.5%
	N_2	64462	N/A
	CH_4	45	> 80
	CO	88	> 1000
	CO_2	1904	> 15000
	C_2H_4	2	> 100
	C_2H_6	1	> 350*
	C_2H_2	0	> 70
	C_3H_8		
Total % Gas		8.5	
Total Gas Combustible		1837	*Age compensated
Transformer insulating paper condition			
2FAL		2.3768	
FURAN		4.04	
Water in paper: % Dry Weight			2.0 (max)
Water in paper: Total litres			

Table VIII: TK25/3 oil sample test results

Transformer number: TK25/4			
Voltage	**525V/400V**	**VA rating**	**150 kVA**
Vector group	**Dyn11**	**Tap changer**	**Off load**
Impedance	**5**	**Consevator**	**No**
Installation date	**1960**	**Oil type**	**Mineral**
Transformer internal condition: Dissolved Gas (DGA) vpm @ NTP			
Hydrogen	H_2	10	> 1000
	O_2	19685	> 0.5%
	N_2	90217	N/A
	CH_4	5	> 80
	CO	122	> 1000
	CO_2	4293	> 15000
	C_2H_4	7	> 100
	C_2H_6	5	> 350*
	C_2H_2	0	> 70
	C_3H_8		
Total % Gas		11.43	
Total Gas Combustible		149	*Age compensated
Transformer insulating paper condition			
2FAL		1.6014	
FURAN		2.691	
Water in paper: % Dry Weight			2.0 (max)
Water in paper: Total litres			

Table IX: TE37 oil sample test results

Transformer number: TE37			
Voltage	**6.6kV/550V**	**VA rating**	**4000 kVA**
Vector group	**Dyn11**	**Tap changer**	**On load**
Impedance	**7.705**	**Consevator**	**Yes**
Installation date	**1999**	**Oil type**	**Mineral**
Transformer internal condition: Dissolved Gas (DGA) vpm @ NTP			
Hydrogen	H_2	27	> 1000
	O_2	48866	> 0.5%
	N_2	277637	N/A
	CH_4	89	> 80
	CO	319	> 1000
	CO_2	7294	> 15000
	C_2H_4	423	> 100
	C_2H_6	72	> 350*
	C_2H_2	16	> 70
	C_3H_8		
Total % Gas		33.47	
Total Gas Combustible		946	*Age compensated
Transformer insulating paper condition			
2FAL		1.5136	
FURAN		2.53	
Water in paper: % Dry Weight			2.0 (max)
Water in paper: Total litres			

Table X: TH35 oil sample test results

Transformer number: TH35			
Voltage	**6.6kV/550V**	**VA rating**	**2000 kVA**
Vector group	**Dyn11**	**Tap changer**	**On load**
Impedance	**6.35**	**Consevator**	**Yes**
Installation date	**1996**	**Oil type**	**Mineral**
Transformer internal condition: Dissolved Gas (DGA) vpm @ NTP			
Hydrogen	H_2	13	> 1000
	O_2	14946	> 0.5%
	N_2	64812	N/A
	CH_4	3	> 80
	CO	199	> 1000
	CO_2	4974	> 15000
	C_2H_4	4	> 100
	C_2H_6	2	> 350*
	C_2H_2	0	> 70
	C_3H_8		
Total % Gas		8.5	
Total Gas Combustible		221	*Age compensated
Transformer insulating paper condition			
2FAL		1.5631	
FURAN		2.613	
Water in paper: % Dry Weight			2.0 (max)
Water in paper: Total litres			

Chendong's formula (1) can be used to confirm the outcomes on the test report of TE44 [8]:

$$DP = \frac{\log_{10}(2FAL) - 1.51}{-0.0035}$$

$$DP = \frac{\log_{10}(1.7783) - 1.51}{-0.0035} = 360$$

The DP can then be used to determine the percentage life of the transformer by using formula (2) [28]:

$$\%Life\ used = \frac{\log_{10}(DP) - 2.903}{-0.006021}$$

$$\%Life\ used = \frac{\log_{10}(360) - 2.903}{-0.006021} = 57.6$$

Formula (3) can be used to estimate the used life in years [28]:

$$Used\ life(in\ years) = 20.5 \ln\left(\frac{1100}{DP}\right)$$

$$Used\ life(in\ years) = 20.5 \ln\left(\frac{1100}{360}\right)$$

$$Used\ life(in\ years) = 22.9$$

Applying the same equation to the rest of the transformers, the used life in percentage and in years are determined as shown in table XI. Figure 1 shows the relationship between the DP and used life.

Table XI: Calculated results

	TE44	TK25/4	TE21	TE23	T2	T1	TE40	TK25/3	TE37	TH35
DP	360	295	480	614	673	463	324	373	380	376
Life (%)	57.6	71.9	36.8	19	12.5	39.4	65.2	55	53.7	54.4
Life (yrs)	23	26.9	17	12	10	18	25	22	22	22

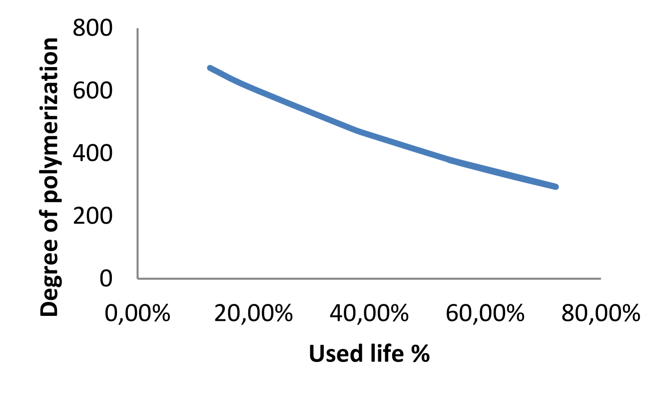

Figure I: DP vs used life

From Table XI, it can be seen that the estimation of lifetime obtained for some of the transformers that have been studied in this paper using the concentration of furanic compounds is not very accurate. This has been caused by the fact that the oil of these transformers has been purified or changed due to the maintenance strategy of the organization.
This method further shows that TK25/3, TE40, TE44 & TE 23 which have been in service for more than 40 years, which is the estimated life of a transformer, have only used just over 20 years of their respective insulating paper's life. It is known that the insulating paper of the transformers has never been replaced, which makes it impossible for this method to accurately measure the remnant life of the transformer.
This method is therefore suitable to identify whether a power transformer is at or near the end of its operation life, types of possible faults and recommendations for future maintenance action.

B. Life estimation and reliability using Weibull distribution method and median rank regression

Weibull distribution which is widely used in reliability and life data analysis, accurately describes the distribution of data on service life of electrical equipment. With few data points, Weibull distribution can provide reasonably accurate analysis and prediction of failures and therefore facilitates cost-effective and efficient component maintenance and testing [8]. To predict cumulative probability of failure up to a specific time t, Weibull cumulative distribution function, F(t), is used as expressed by (4). The probability density function f(t) which is a derivative of the cumulative distribution function, is expressed by formula (5)[9]:

$$\mathrm{F(t)} = 1 - e^{-\left(\frac{t}{\alpha}\right)^{\beta}} \qquad (4)$$

$$\mathrm{f(t)} = \frac{\beta}{\alpha}\left(\frac{t}{\alpha}\right)^{\beta-1} * e^{-\left(\frac{t}{\alpha}\right)^{\beta}} \qquad (5)$$

where:
***t** is* the failure time, expressed as a variable;
α is the scale parameter or termed as the characteristic lifetime;
β is the shape parameter.

This two-parameter Weibull distribution has a very important characteristic whereby the value of the shape parameter corresponds to three regions of the bathtub curves as follow [10]

- Region 1, β < 1, where hazard rate decreases as transformer ages;
- Region 2, β = 1, where hazard rate is independent of the time;
- Region 3, β > 1, representing the relationship that hazard rate increases as transformer ages.

The characteristic lifetime or scale parameter, α, characterizes the time by which 63.2% of the transformers are anticipated to have failed. For the special case that β=1, the value of α is the same as the mean lifetime of the distribution [19].

To estimate the Weibull parameters, median rank regression [11], [12] linearizes the Weibull data and then performs simple linear regression on the transformed data.

$$Median\ rank(t) = \frac{i-0.3}{n+0.4} \qquad (6)$$

The two parameter Weibull was used to determine the reliability and service life of the ten transformers. This is done using excel. This method allows evaluating the technical condition of the transformer and its mean service life [8].
Table XII shows linear regression preparation table which is done on an excel page and table XIII show the results of the linear regression. Figure II shows the result of the linear regression in a graph form.

Table XII: Linear regression preparation

16	Preparing Design A for Weibull Analysis						
17		A	B	C	D	E	F
18	1	Design A hours	Rank	Median Ranks	1/(1-Median Rank)	Ln(Ln(1/(1-Median Rank)))	Ln(Design A hours)
19	2	131400	1	0.067307692	1.072164948	-2.663843085	11.78600139
20	3	192720	2	0.163461538	1.195402299	-1.72326315	12.16899364
21	4	201480	3	0.259615385	1.350649351	-1.202023115	12.2134454
22	5	210240	4	0.355769231	1.552238806	-0.821666515	12.25600501
23	6	227760	5	0.451923077	1.824561404	-0.508595394	12.33604772
24	7	289080	6	0.548076923	2.212765957	-0.230365445	12.57445875
25	8	395160	7	0.644230769	2.810810811	0.032924962	12.88704603
26	9	490560	8	0.740384615	3.851851852	0.299032932	13.10330287
27	10	490560	9	0.836538462	6.117647059	0.593977217	13.10330287
28	11	508080	10	0.932692308	14.85714286	0.992688929	13.13839419

Table XIII: Linear regression results

	A	B	C	D	E	F	G	H	I
1	SUMMARY OUTPUT								
2									
3	*Regression Statistics*								
4	Multiple R	0.954010733							
5	R Square	0.910136479							
6	Adjusted R Square	0.898903539							
7	Standard Error	0.354532393							
8	Observations	10							
9									
10	ANOVA								
11		*df*	*SS*	*MS*	*F*	*Significance F*			
12	Regression	1	10.18415317	10.18415317	81.0238877	1.85111E-05			
13	Residual	8	1.005545743	0.125693218					
14	Total	9	11.18969891						
15									
16		*Coefficients*	*Standard Error*	*t Stat*	*P-value*	*Lower 95%*	*Upper 95%*	*Lower 95.0%*	*Upper 95.0%*
17	Intercept	-28.53377264	3.113855607	-9.16348612	1.62309E-05	-35.71433654	-21.35320873	-35.71433654	-21.35320873
18	Ln(Design A hours)	2.230734177	0.247822813	9.001326997	1.85111E-05	1.659253746	2.802214609	1.659253746	2.802214609
19	**Beta (Shape parameter) =**	**2.230734177**							
20	**Alpha (Life characteristic) =**	**359044.8258**							
21									
22	RESIDUAL OUTPUT								
23									
24	*Observation*	*Predicted Ln(Ln(1/(1-Median Rank)))*	*Residuals*						
25	1	-2.242336533	-0.421506553						
26	2	-1.387982626	-0.335280524						
27	3	-1.28882256	0.086799445						
28	4	-1.193883374	0.372216858						
29	5	-1.01532937	0.506733976						
30	6	-0.483497752	0.253132307						
31	7	0.213801377	-0.180876415						
32	8	0.696212922	-0.39717999						
33	9	0.696212922	-0.102235705						
34	10	0.774492328	0.218196601						
35									

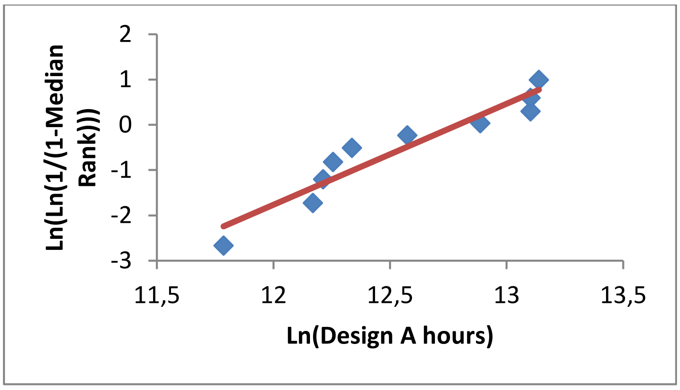

Figure II: Linear regression result in a graph form

From the linear regression results the Weibull calculator is developed and used to calculate the reliability and remnant lives of the transformers. Table XIV shows the developed Weibull calculator.

Table XIV: Weibull calculator

	A	B	C	D	E	F
1	Beta (Shape Parameter) =	2.230734		Hours	Survival Probability	Reliability
2	Alpha (Characteristic life =	359044.8		131400	0.100764257	0.8992357
3				192720	0.22087072	0.7791293
4				201480	0.240879755	0.7591202
5				210240	0.261432035	0.738568
6				227760	0.303914711	0.6960853
7				289080	0.460235757	0.5397642
8				395160	0.710145632	0.2898544
9				490560	0.865493249	0.1345068
10				490560	0.865493249	0.1345068
11				508080	0.88576419	0.1142358
12						
13			Reliability	Hours	Yrs	
14			0.8992357	131400	25	
15			0.7791293	192720	18	
16			0.7591202	201480	17	
17			0.738568	210240	16	
18			0.6960853	227760	14	
19			0.5397642	289080	7	
20			0.2898544	395160	-5.109589041	
21			0.1345068	490560	-16	
22			0.1345068	490560	-16	
23			0.1142358	508080	-18	

The estimated maximum service years of a transformer before failure are 40 years.

$$\text{Estimated Max Hours of Operation} = 8760 * 40 = 350\,400\ hrs$$

Figure III shows that 40% of the transformers will operate beyond the estimated maximum service years of transformers.

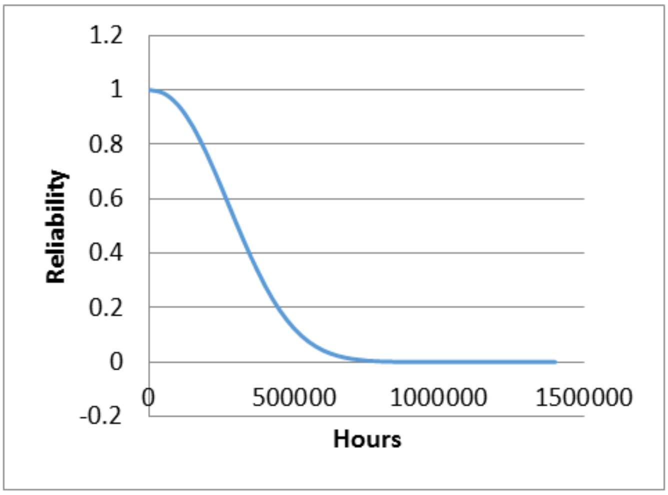

Figure III: Survival data graph

Table XV shows the tabulated results from the Weibull calculator for each of the transformers.

Table XV: Results from Weibull and Median rank regression

	TE44	TK25/4	TE21	TE23	T2	T1	TE40	TK25/3	TE37	TH35
β	2.23	2.23	2.23	2.23	2.23	2.23	2.23	2.23	2.23	2.23
α	359 045	360 045	361 045	362 045	363 045	364 045	365 045	366 045	367 045	368 045
Reliability (%)	13.45	75.91	53.98	28.99	69.61	73.86	13.45	11.42	89.92	77.91
Remnant (yrs)	-16	17	7	-5	14	16	-16	-18	25	18

Table XV shows that for the same β and α values which are 2.23 and 359045 respectively, the transformers give different reliabilities depending on the number of hours that each transformer has been running.

When the transformer has been running for longer hours its survival probability is higher but its reliability is lower. Whereas a transformer that has been running for a shorter period gives a lower survival probability and a higher reliability.

Table XIV shows that four transformers have already surpassed the estimated life of a transformer, TE23 by 5 years, TE40 and TE44 by 16 years and TK25/3 by 18 years.

The remnant life of these four transformers indicates that plans should be made for the replacement of these transformers.

III. Conclusion

This paper presents analysis of life estimation and reliability of ten representative power transformers. In order to evaluate the technical condition of the transformers hence determining their reliability and service life, furan analysis technique of the oil samples was used and subsequently Weibull analysis method was applied. The comparison between the Furan method and Weibull method shows a lot of differences due to a number of factors one being the oil change or purification which washes the furan away thereby leaving insufficient furan to accurately estimate the remnant life of a transformer [8]. The furan analysis result also shows how the lifespan of a transformer can be increased if there is a continuous proper oil maintenance.

IV. Acknowledgement

The author acknowledges Mpact operations, Piet Retief mill for allowing the use of their equipment and information for the experimental work.

V. References

[1] Pradhan, M.K. and Ramu, T.S., 2005. On the estimation of elapsed life of oil-immersed power transformers. *IEEE Transactions on Power Delivery*, *20*(3), pp.1962-1969.

[2] Pandurangaiah, D., Reddy, C.C., Govindan, T.P., Mandlik, M. and Ramu, T.S., 2008, June. Estimation of remaining life of power transformers. In *Electrical Insulation, 2008. ISEI 2008. Conference Record of the 2008 IEEE International Symposium on* (pp. 243-246). IEEE.

[3] Weedy, B.M., 2012. Electric power systems. 5th edition Wiley. ISBN 980-0-470-68268-5

[4] H. Borsi, E. Gochenbach and V. Wasserberg, Life time Extension of Transformers by On-line Drying, in 19th International Power System Conference (PSC 2004) Iran-Tehran.

[5] F. Ortiz, C. Fernández, A. Santisteban, F. Delgado, and A. Ortiz, "Estimating the age of power transformers using the concentration of furans in dielectric oil" International Conference on Renewable Energies and Power Quality (ICREPQ'16) Madrid (Spain), 4th to 6th May, 2016

[6] Mr. K Baburao, Mr. NM Bhangre, Mr.AM Wagle, Mr. A.Venkatasami, Mr. Sushil E Chaudhari, "The experience of DP and Furan in Remnant Life Assessment of Power Transformer" 2008 International Conference on Condition Monitoring and Diagnosis, Beijing, China, April 21-24, 2008

[7] Inderpreet Kaur, Preetinder Singh, "Residual Life assessment with DGA, Furan content in transformer oil and Degree of polymerization of solid insulation" International Journal of Scientific and Research Publications, Volume 6, Issue 7, July 2016

[8] Julija Badune, Sandra Vitolina, Vjaceslav Maskalonok, "Methods for Predicting Remaining Service Life of Power Transformers and Their Components" *Riga Technical University*

[9] Dan Zhou, "Comparison of Two Popular Methods for Transformer Weibull Lifetime Modelling" International Journal of Advanced Research in Electrical, Electronics and Instrumentation Engineering Vol. 2, Issue 4, April 2013

[10] John, Reliability prediction, 2007

[11] Weibull analysis, British Standard Institute (BSI) and International Electrotechnical Commission (IEC) BS EN 61649:2008, 2008.

[12] Abernethy, R., The New Weibull Handbook, 5th ed. Florida: Robert B. Abernethy, 2006.

[13] International Journal of Advanced Research in Electrical, Electronics and Instrumentation Engineering, Vol. 2, Issue 4, April 2013, Comparison of Two Popular Methods for Transformer Weibull Lifetime Modelling.

2019 SAUPEC/RobMech/PRASA Conference
Bloemfontein, South Africa, January 28-30, 2019

Effect of Input Features on the Performance of the ANN-based Wind Power Forecasting

Qin Chen
Department of Electrical Engineering
University of Cape Town
South Africa
chnqin002@myuct.ac.za

Komla Folly
Department of Electrical Engineering
University of Cape Town
South Africa
komla.folly@uct.ac.za

***Abstract*— As the penetration of wind power increases in power system, accurate short-term wind power forecasts will become very crucial for effective grid operation and management. With the availability of a large amount of meteorological data and computational power, artificial neural networks (ANNs) have become a very popular method for forecasting. The purpose of this paper is to provide an inexpensive but reliable ANN model to forecast wind power produced from wind turbines for small wind farms. It is shown that the ANN model with all the input features and large training sample size has the best forecasting results compared to the one with small sample size and input features. The tradeoff between forecasting performance and computational cost is also analyzed in the paper.**

Keywords*— *artificial neural networks, short-term wind power forecasting, input features

I. Introduction

The Renewable Energy Independent Power Producers Procurement Programme (REI4P) of South Africa is an extensive initiative to install 17.8 GW of electricity generation capacity from renewables over the period 2012-2030 [1]. Among all the renewables sources, wind energy is one of the most efficient, available, and affordable renewable energy sources. However, it is difficult to accurately predict the power generated from wind turbines due to the intermittent nature of wind. With the increase of wind power penetration, the accurate forecasting of wind power is required for the reduction of system operating cost and the stability of the power system [2].

Commonly used wind power forecasting methods can be divided into two main groups namely, physical approaches and statistical approaches. In the physical approaches, local wind speed is estimated by using the physical laws governing atmospheric behaviour. In the statistical approaches, the relationship between a set of input variables and the wind speed or the wind power is determined by the statistical approach [3]. Wind speed patterns can be very different between wind farms and are often influenced by many factors that are location-specific. Therefore, there is no single best forecasting algorithm that can be applied to all wind farms [4]. Many authors used artificial neural networks (ANNs) for average wind speed and wind power forecasting [4] [5] [6] [7]. ANNs are mathematical tools originally inspired by the function of the human brain. They can model complex non-linear relationships and approximate any measurable function [8].

This paper is organized as follows. Section 2 presents the methodology of input features and model parameters selection. Section 3 mainly deals with the data collection and forecasting performance evaluation metrics. Section 4 is concerned with the simulations results and discussions. Finally, section 5 outlines the conclusions.

II. Methodology

A. Artificial Neural Network Architectures

There are many different types of artificial neural networks. Seven commonly used ANN types are feedforward multilayer perceptron (MLP), convolutional neural network (CNN), recursive neural network (RNN), recurrent neural network, long short-term memory (LSTM), sequence-to-sequence models, and shallow neural networks. Among all the types of ANN, the feedforward multilayer perceptron is the first and simplest type of artificial neural network devised [9]. The feedforward multilayer perceptron neural network is used in this paper due to its simplicity and popularity.

In a feedforward neural network, connections between nodes do not form a loop. The information moves in the forward direction only, from the input nodes through the hidden nodes and then to the output nodes. The structure of two layers feedforward neural network is shown in Fig. 1.

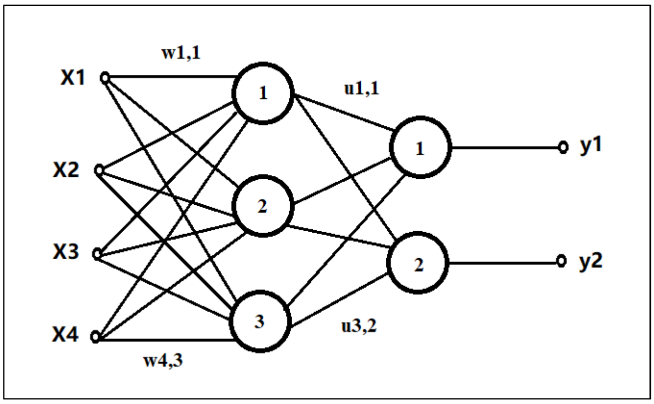

Fig. 1: Structure of two layers feedforward neural network [10]

As can be seen in Fig. 1, the MLP consists of two layers namely, hidden layer, and output layer. Input nodes do not form a layer, as their function is to feed the input variables to the model. Referring to Fig. 1, there are four input nodes (*X1, X2, X3,* and *X4*). Each input node can be represented by different input variables, such as wind speed, wind direction, atmospheric pressure, temperature, and other meteorological variables. The weight matrix W_{1x1} connect the input 1 to the hidden neuron 1. Similarly, u_{1x1} stands for the weight of connection between hidden neuron 1 to output neural 1. The basic unit for ANNs is an artificial neuron, it can be found in hidden layer and output layer. The schematic of an artificial neuron is shown in Fig. 2.

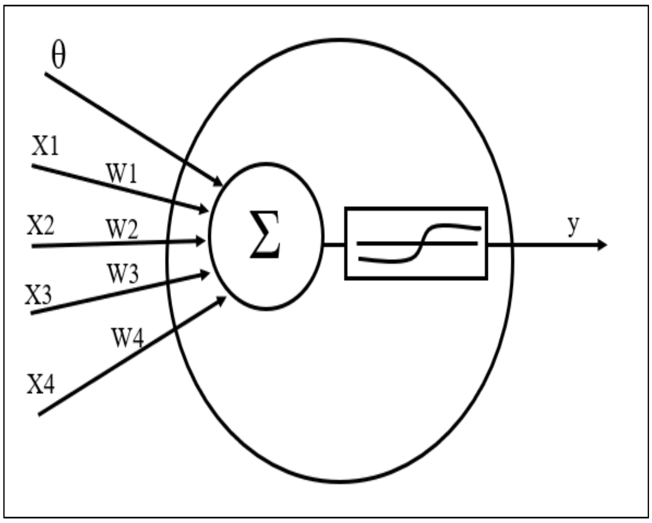

Fig. 2: Schematic of an artificial neuron [10]

There are two stages involved to process the input numerical information to the output layer. In the first stage, the weights W_i are assigned to each input variables before they are linearly combined. The results are then used as the arguments of a non-linear activation function. Each neuron can be defined as [11]:

$$Y = f[\sum(x_1 w_1 + x_2 w_2 + x_3 w_3 + \cdots) + \beta) \qquad (1)$$

where:

$x_1,\ x_2,\ x_3, \ldots$ are the input variables

$w_1, w_2, w_3, \ldots$are the connection weights

β is the bias values

f is the transfer function

B. *Data Pre-processing*

Data pre-processing is a set of techniques implemented prior to the use of raw data. Since raw data will likely be imperfect, containing inconsistencies and redundancies is not directly applicable for training the network. Among all the data pre-processing techniques, normalization is one of the most commonly used data pre-processing techniques.

The maximum value of each input feature is different from each other. For example, wind direction (0-360°) and barometric pressure (973-998 hPa) have larger values compare with wind speed (0.3-20.6 m/s) and air temperature (8.5-41.3 °C). Input features with larger values tend to suppress the influence of the input features with smaller values. Therefore, the min-max normalization technique is used to overcome this problem. The normalization of data is obtained by using the following transformation [12].

$$X_i' = \left(\frac{X_i - X_{min}}{X_{max} - X_{min}}\right)(X_{max}' - X_{min}') + X_{min}' \qquad (2)$$

where:

X_i, X_{min}, X_{max} are the actual input data, minimum and maximum input data

X_i', X_{min}', X_{max}' are the normalized input, minimum and maximum target value.

In this paper, X_{min}' is set to 0 and X_{max}' is set to 1. Therefore, the Eq. 2 becomes Eq. 3.

$$X_i' = \left(\frac{X_i - X_{min}}{X_{max} - X_{min}}\right) \qquad (3)$$

C. *Input Feature and Sample Size Selection*

Input feature selection is "the process of identifying and removing as much irrelevant and redundant information as possible" [13]. The goal of input feature selection is to obtain a subset of features from the original dataset that still appropriately describe it [14].

The data that can be used for inputs are wind speed, wind direction, air temperature gradient, air temperature, barometric pressure, relative humidity, etc. However, not all of the available meteorological data has a significant influence on wind speed forecasting. Due to the large number of variables contained within meteorological data, ANNs may not be able to induct patterns from the data or may over fit the learned model to the data. As a result, the generalizability of the model is reduced [15]. The influence of each input feature on the forecasting accuracy is determined by using one input feature at a time. Combinations of different input features are also tested to find the most accurate model.

The larger training sample size will require stronger computational power and longer training time. Therefore, the goal is to find a suitable number of sample size, which can not only provide good forecasting results but also reduce the computational cost and training time. The approach used in this paper is to start training the network with relatively small sample size (1000 samples), then increase the sample size gradually until the forecasting accuracy stopped improving. The final sample size used in this paper is 20000.

D. *Selection of the Number of Hidden Neurons*

Selection of the number of hidden neurons for ANN is one of the major problems faced by many researchers. The complex model structure might result in an overfitting of a network. Overfitting occurs when the model fits the data so well that some of the error, such as outliers are included in the structure, and then result in a bad performance. Similar to many authors, in this paper, a trial and error method was used to determine the number of hidden neurons [10].

E. *Time-scale Classification*

Soman et al. [16] suggested that time-scale for the operation of the electricity system can be divided into four sections, namely very short-term, short-term, medium-term, and long-term. The forecasting horizon for the very short-term is from few seconds to 30 minutes; and for the short-term, the forecasting horizon is from 30 minutes to 6 hours. The medium-term has the range between 6 hours to 1 day. Forecasting horizon longer than 1 day ahead is classified as the long-term forecasting.

The focus of this paper is to forecast short-term wind power generated from wind turbines. two hours ahead forecasting horizon is used throughout the paper for consistency.

III. WIND DATA AND FORECASTING PERFORMANCE EVALUATION

A. Data Collection

The meteorological data used in this paper are provided by the Wind Atlas of South Africa (WASA). The dataset consists of wind speed measured at different heights, wind direction, temperature, atmospheric pressure, and relative humidity with 10 minutes resolution for the period from Midnight 31 December 2010 to Midnight 1 January 2017. The range and mean of the data are shown in TABLE I.

TABLE I. SUMMARY OF METEOROLOGICAL DATA

No.	Variable Name	Unit	Range	Mean
1	Wind Speed	m/s	0.3-20.6	19.5
2	Wind direction	°TN	0.0-360.0	-0.1
3	Air temperature	°C	8.5-41.3	985.1
4	Air temperature gradient	°C	-2.0-13.6	65.2
5	Barometric pressure	hPa	973.5-997.9	191.3
6	Relative Humidity	%	4.5-97.1	7.5

B. Performance Evaluation Metrics

To compare the performance of each model numerically, evaluation metrics are required. Three most commonly used accuracy measures are the normalized root mean square error (NRMSE), normalized mean absolute error (NMAE), and the mean absolute percentage error (MAPE) [17]. The sensitivity of the NRMSE to outliers is the most common concern with the use of this evaluation method [18]. On the other hand, NMAE is a more natural measure of average error [19]. MAPE is scale-independent and easy to interpret. However, it yields extremely large percentage errors when there are outliers in the data and produce infinite result when the actual value is zero [20]. Each evaluation metric has its advantage and disadvantage. As a result, all above mentioned metrics are used in this paper to determine the performance of the model with different input features and sample sizes. The formulations of the three metrics are shown below:

$$NRMSE = \frac{100\sqrt{\sum_{t=0}^{N}(o_t - f_t)^2}}{\sqrt{N}(o_{max} - o_{min})} \quad (4)$$

$$NMAE = \frac{100}{N}\sum_{t=1}^{N}\frac{|o_t - f_t|}{(o_{max} - o_{min})} \quad (5)$$

$$MAPE = \frac{100}{N}\sum_{t=1}^{N}\frac{|o_t - f_t|}{o_{ave}} \quad (6)$$

where:

N is the number of forecasting periods

o_t is the observation at time t

f_t is the forecasted value at time t

And o_{ave} is given by:

$$o_{ave} = \frac{1}{N}\sum_{t=1}^{N} o_t \quad (7)$$

C. Wind Speed and Wind Power Conversion

Predicted wind speed needs to be converted to wind power by using the following equation:

$$P(v) = \frac{1}{2}\rho(t)Av^3C_p(v) \quad (8)$$

where:

$P(v)$ is wind power generated by the wind turbine

$\rho(t)$ is air density

A is the sweep area of the blades

v is wind speed

$C_p(v)$ is the power coefficient

IV. RESULTS AND DISCUSSION

The ANN model needs to be trained before can be used to forecast the wind speed and wind power. The initial weights are randomly selected by the model, so the model configurations are slightly different from training to training. In this paper, each model is trained, validated and tested 5 times so that the final result is more reliable than the single simulation and the computational time is not too long. The final result is the aggregate of all 5 results.

A. Sample Size Selection

When data sets become large the computational cost and time will rise. The goal is to find an optimal number of input sample size which allows the model to not only produce good forecasting performance but also use the lowest computational cost. For the purpose of comparison, all the variables, such as input features, model architecture, and model configurations stay the same except the sample size. The graph of performance against the number of training samples is shown in Fig. 3.

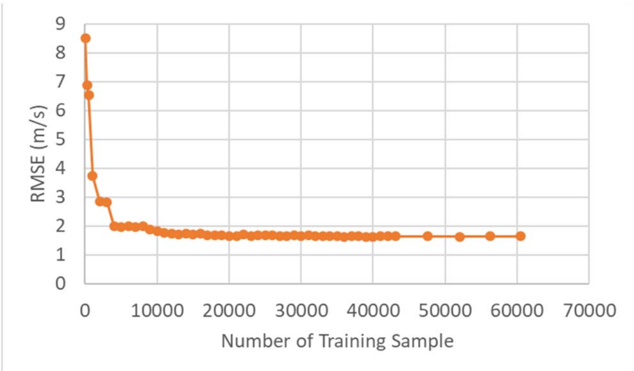

Fig. 1: Graph of performance against the number of training samples

As can be seen in Fig. 3, the forecasting performance improved with the increased number of the training samples. However, the RMSE values stopped improving when the number of training sample is increased above 20000. The graph of model training time against number of training sample is shown in Fig. 4.

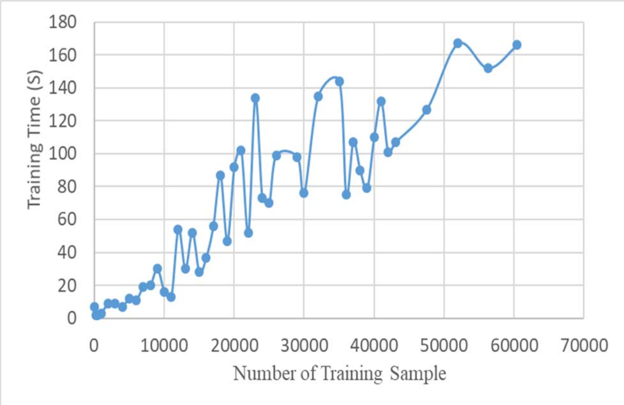

Fig. 2: Graph of training time against number of training sample

As shown in Fig. 4, the training time is increased with the number of training samples. It took 92 seconds to train the model with 20000 input samples and 166 seconds to train the model with 60000 input samples. Based on the Fig. 3, it can be concluded that the RMSE values of the model with 20000 input samples and 60000 input samples are very similar. As a result, 20000 input samples are selected to train the model.

B. *Input Feature Selection*

The correlation coefficients between the target wind speed (2 hours ahead) and input features are calculated and summarized in TABLE II. A correlation coefficient of 1 indicates a perfect positive correlation. This means a positive increase in one variable, there is also a positive increase in the second variable. A correlation coefficient of -1 indicates a negative correlation. This means one variable increases while the other variable decreases.

TABLE II. SUMMARY OF CORRELATION COEFFICIENT

Input feature	Correlation coefficients
Wind Speed	0.75
Wind Direction	0.18
Temperature	0.24
Temperature Gradient	-0.38
Relative Humidity	-0.34
Barometric Pressure	-0.01

The correlation coefficient indicates how strong two variables are related to each other. All the input features shown in TABLE III are measured 2 hours prior to prediction. Based on the results in TABLE II, wind speed and 2 hours ago wind speed has the highest correlation. This is reasonable, as the wind speed has persistence property. The correlation between wind speed and temperature gradient is the second strongest. The results shown that there is barely any correlation between wind speed and 2 hours ago barometric pressure. The importance of each input feature is examined further by evaluating the performance of each model with different input features. The evaluation results of 2 hours ahead wind speed forecasting is shown in TABLE IV.

TABLE V. SUMMARY OF THE PERFORMANCE OF THE MODEL WITH DIFFERENT INPUT FEATURES AND THEIR COMBINATIONS

No.	Input feature	NRMSE	NMAE	MAPE
1	WS	11.2%	9.1%	44.1%
2	WD	13.7%	11.1%	58.5%
3	TG	13.6%	11.2%	59.9%
4	T	16.2%	13.6%	76.1%
5	RH	16.4%	13.7%	75.0%
6	P	17.4%	15.1%	80.8%
7	WS, WD,	10.5%	8.4%	41.9%
8	WS, TG	8.7%	6.9%	33.4%
9	WS, WD, T	9.3%	7.3%	38.3%
10	WS, WD, TG	8.3%	6.5%	33.4%
11	WS, WD, T, TG	8.2%	6.4%	32.9%
12	WS, WD, T, TG, RH	8.1%	6.4%	32.5%
13	WS, WD, T, TG, P, RH	**8.0%**	**6.3%**	**31.8%**

The following are defined for TABLE VI:

WS = wind speed

WD = wind direction

TG = air temperature gradient

T = air temperature

RH = relative humidity

P = barometric pressure

The numbers in the first column of TABLE VII is used to identify the model. For example, number 1 represents the model with wind speed as input feature only. Number 13 represents that the model uses all 6 variables as input features. The first 6 models are used to test the importance of each input feature for the wind speed forecasting accuracy. Different combinations of input features are used from model number 7 to model number 13.

Based on the results shown in TABLE II and TABLE VIII, wind speed is the most important input feature for wind speed forecasting. It has the highest correlation with 2 hours ahead wind speed and the evaluation results are the lowest among six single input features. Air temperature gradient is the second significant input feature. Even though the correlation between wind speed and wind direction is low, the influence of wind direction on wind speed forecasting is high. Based on the evaluation results and correlation coefficient, it can be concluded that 2 hours ago barometric pressure has a lesser influence on the wind speed forecasting performance than the other 5 input features. The model has the best performance when all 6 input features are included for the training. Simulation results of number 10 to number 13 are very similar. It took 63 seconds to train the model number 10 and 92 seconds to train the model number 13. Instead of using all input features, combination of wind speed, wind direction and air temperature gradient can be used as input features if there are computational and time constraints.

The best performing model is used to forecast the potential wind power that can be generated at the Vredendal station (WM03). The reasons to use the data form Vredendal station are that the data are complete, and the station is located in Western Province.

The curves of the forecasted wind power and the calculated wind power is shown in Fig. 5. It can be seen that the ANN model with all 6 input features managed to accurately forecast the wind power between sample 1 to sample 210.

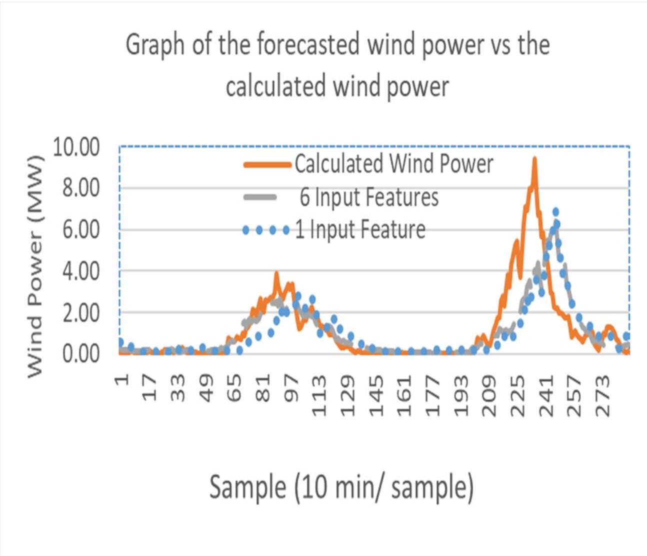

Fig. 3: Graph of the forecasted wind power vs the calculated wind power

Two peaks in Fig. 5 indicate that the wind speed is usually stronger in the afternoon. Graphs between sample 65 and sample 129 indicate that the model with all six input features performs better than the model with wind only speed as input feature. Between sample 209 to sample 257, both models do not perform well because the gradient of the wind speed is big. Both models need to forecast the wind speed more accurately when the wind speed gradient is high. One possible way to solve this problem is to use several small ANN models to forecast wind speed at different periods of the day.

V. Conclusions

An artificial neural network is constructed for short-term (2 hours ahead) wind speed and wind power forecasting. The optimal number of training samples, input features were selected to get the best model. Based on the correlation and evaluation results, the optimal number of samples for training is 20000, and the wind speed and air temperature gradient are the two most important input features. Accurate wind power forecasting allows wind plant operators to reduce imbalance charges and penalties [21]. Therefore, the cost of wind power can be reduced further by improving the performance of the forecasting model. More works need to be done to improve the forecasting accuracy of the model.

References

[1] D. R. Walwyn and A. C. Brent, “Renewable energy gathers steam in South Africa,” *Renewable and Sustainable Energy Reviews,* vol. 41, pp. 390-401, January 2015.

[2] H. Liu , H.-Q. Tian, C. Chen and Y.-f. Li, “A hybrid statistical method to predict wind speed and wind power,” *Renewable Energy,* vol. 35, pp. 1857-1861, February 2010.

[3] I. J. Ramirez-Rosaso, L. A. Fernandez-Jimenez, C. Monteiro, J. Sousa and R. Bessa, “Comparison of two new short-term wind-power forecasting systems,” *Renewable Energy,* vol. 34, pp. 1848-1854, 2009.

[4] Z.-h. Guo, J. Wu, H.-y. Lu and J.-z. Wang, “A case study on a hybrid wind speed forecasting method using BP neural network,” *Knowledge-Based Systems,* vol. 24, pp. 1048-1056, May 2011.

[5] A. M. Foley, P. G. Leahy, A. Marvuglia and J. E. McKeogh, “Current methods and advances in forecasting of wind power generation,” *Renewable Energy ,* vol. 37, pp. 1-8, 2012.

[6] M. G. De Giorgi, A. Ficarella and M. Tarantino, “Error analysis of short term wind power prediction models,” *Applied Energy,* vol. 88, pp. 1298-1311, 2011.

[7] R. Jursa and K. Rohrig, “Short-term wind power forecasting using evolutionary algorithms for the automated specification of artificial intelligence models,” *International Journal of Forecasting,* vol. 24, pp. 694-709, 2008.

[8] Q. Chen and K. Folly, “Comparison of three methods for short-term wind power forecasting,” in *International Joint Conference on Neural Networks (IJCNN)*, Rio de Janeiro, 2018.

[9] J. Schmidhuber, "Deep learning in neural networks: An overview," *Neural Networks,* vol. 61, pp. 85-117, January 2015.

[10] H. S. Hippert, C. E. Pedreira and R. C. Souza, “Neural networks for short-term load forecasting: a review and evaluation,” *IEEE Transactions on Power Systems,* vol. 16, no. 1, pp. 44-54, 2001.

[11] A. More and M. Deo, “Forecasting Wind With Neural Networks,” *Marine Structures,* vol. 16, pp. 35-49, 2003.

[12] K. G. Sheela and S. Deepa, “Review on methods to fix number of hidden neurons in neural networks,” Hindawi Publishing Corporation, Coimbatore, 2013.

[13] M. A. Hall, “Correlation-based feature selection for machine learning,” The University of Waikato, Hamilton, April 1999.

[14] S. Garcia, S. Ramirez-Gallego, J. Luengo, J. M. Benitez and F. Herrera, “Big data preprocessing: methods and prospects,” Bid Data Analytics, Granada, 2016.

[15] H. Wimmer and L. Powell, “Principle component analysis for feature reduction and data preprocessing in data science,” in *The Conference on Information Systems Applied Research*, Las Vegas, 2016.

[16] S. S. Soman, H. Zareipour, O. Malik and P. Mandal, “A review of wind power and wind speed forecasting methods with different time horizons,” in *North American Power Symposium*, Arlington, TX, USA, 2010.

[17] J. Liu, X. Wang and Y. Lu, “A novel hybrid methodology for short-term wind power forecasting based on adaptive neuro-fuzzy inference system,” *Renewable Energy,* vol. 103, pp. 620-629, 2017.

[18] T. Chai and R. R. Draxler, “Root mean square error (RMSE) or mean absolute? - arguments against avoiding RMSE in the literature,” *Geoscientific Model Development,* vol. 7, pp. 1247-1250, 2014.

[19] C. J. Willmott and K. Matsuura, “Advantages of the mean absolute error (MAE) over the root mean square error (RMSE) in assessing average model performance,” *Climate Research,* vol. 30, pp. 79-82, 2005.

[20] S. Kim and H. Kim , “A new metric of absolute percentage error for intermitter demand forecasts,” *International Journal of Forecasting,* vol. 32, pp. 669-679, 2016.

[21] A. Vaccaro, P. Mercogliano, P. Schiano and D. Villacci, “An adaptive framework based on multi-model data fusion for one-day-ahead wind power forcasting,” *Electric Power Systems Research,* vol. 81, pp. 775-782, 2011.

2019 SAUPEC/RobMech/PRASA Conference
Bloemfontein, South Africa, January 28-30, 2019

Deployment of a renewable energy power generation in a typical rural village: A Case Study

Mpho J. Lencwe[a] and SP Daniel Chowdhury[b]
[a]Student Member IEEE, Tshwane University of Technology, Pretoria, South Africa
[b]IEEE Senior Member, Tshwane University of Technology, Pretoria, South Africa
mpholencwe@gmail.com, spchowdhury2010@gmail.com

***Abstract*— Electricity access and availability for South African rural areas, such as Taung at North West remains a challenge to the society. Electricity shut downs occurs more frequently and for a long period of time due to high power demand in the country (i.e. South Africa). This leaves the society more stranded, compelling them to practice traditional wood fireworks for basic boiling of water and cooking. However, this constitute carbon emission immensely to the climate. Therefore, it is the purpose of this research to study, analyze and recommend the alternative renewable energy supply system suitable for households for the entire village. The analyses is performed using Homer Pro Software. Based on the analyses conducted in Homer, the results indicate that the deployment of renewable energy source based on solar is viable to supply the entire village, furthermore, recommendations are described to overcome certain challenges. The analyses are conducted based on the load profile during winter season, in this study, the months of June-July are of utmost interest. In this research study, optimization and sensitivity of the results are presented. Hence, the results provide the best renewable energy system to be implemented for the entire village in terms of resources and costs, in this case is Solar.**

Keywords—Electricity, Renewable Energy Sources, Outages/Shutdowns, Villages

I. Introduction

Taung is situated at the South of South Africa, Bokone Bophirima (North West). The area is about 5 635 km2. South African Government placed some measures to introduce the socio economic development for households. However, studies indicated that solar power and mini-grid system are the dominating technologies currently for households. Based on the South African National Development Plan (NDP), independent energy producers remain the focus and priority for energy mix [1]. Randall et al. indicated that sum of local energy demand and supply increased by 8-4 times from 2010 to 2070. However, South Africa presented a minor portion contributing to the change in both sectoral arrangement of request and the topography of the request [2]. Saul *et al.* argues that off-grid solar PV system for households in Sub-Sahara African countries is way too expensive and if required to be a success, it needs to be subsidized by the Government throughout [3]. Chowdhury et al. compared the different standalone electrification systems applicable for different consumer load profiles at the Eastern Cape. However the studies were carried out at the coastal areas of South Africa, of which energy demand is very huge during the winter season [4]. In [5] Samuel et al. provided insight to smart grid integration for rural households. This insight provides the information for policy makers in any African country as a reference to implementation of smart grid, however the cost of materials are not covered by this study. Failure on extending electrification to rural areas lead to loss of potential development, furthermore electrification to rural areas clearly benefit the households at many levels [6]. Johannes Urpelainen [7] overviewed several methodologies of roles played by grid extension and off-grid electrification. Methodologies includes; separation, uncoordinated integration and integrated development. He emphasized that many conflicting factors arise if the electrification approach are treated separately. The integration development of grid extension and off-grid electrification indicate that socio economic development can be achieved significantly. Resistance by the nation utility to deployment of off-grid systems can be astounded. This will benefit both parties. This integration will highly reduce strain on the national grid, which allows the customers to feed excess electricity to the grid. This ensures that the poor communities are able to spend less on electricity and able to sustain their daily life. Paul Cook in [8], stated that electrification in rural areas have been very slow, this is due to implementation of cost recovery methodologies and reliance to private entities to deliver electricity widely. He pinned deeply into poverty reduction and emphasized that even though grid-extension have been introduced through stand-alone and mini-grid approaches, this still left many areas without access to reliable electricity. Effective cost of electricity remains a challenge and obtaining the target of the universal electrification by the year 2030 also remains a challenge for developing countries. It is stated that the successful implementation of projects in many developing countries are governed by financial, organizational and governance weakness [9]. For the South African government to alleviate poverty, necessary measures needs to be taken into consideration in order to fast track rural electrification. Unreliable electricity supply has a negative impact in organizations operating in those areas, this includes; closing of operations, loss of employment and increased criminal activities. The paper is organized as follows; Section II present the background of the study, Section III describes the Methodology used to solve the problem statement, Section IV shows the Results analyzed and Section V describes the Conclusions and Recommendations of the research study undertaken.

II. Background

Taung is situated at the North West, South Africa. It consist of various sub-areas, which includes; Pudumoe, Mokgareng, Mokasa, Manthe, Maphoitsile and etc. All this areas are under one municipality district known as Dr Ruth Segomotsi Mompati. Unreliable electricity supply to this areas is a major concern. Only Taung town, which is centrally located, suffice the entire communities at these areas for their necessary shopping, which however, is small to cater for the population at hand. North West including Taung consisting with no sub-areas. Different sub-areas within Taung rely on the national electricity utility supply

978-1-7281-0368-6/19/$31.00 ©2019 IEEE

(Eskom). During load shedding, areas as Taung are the first on the list to be cut-off power. However, it is necessary for renewable energy systems to be introduced to ensure sustainable supply of electricity at all times. In [10], the population distribution among different provinces within the South African provinces are illustrates. It is so sporadic recently to witness areas that are still using paraffin for basic lighting in this era. Moreover, South African country still have those areas. One would ask that, how will poverty alleviation be sustained if mini-grid deployment in areas such as Taung is still a problem? What does grid-extension mean to South Africa, is this traditional way of building coal powered fired station and nuclear power stations a solution? What does reduction to emission mean? Although, the sources of energy in the North West province is indicated in [10], and paraffin source of energy is a small portion (constituted by 21 893 population), the living conditions of people is not improved in any manner, therefore, it is the purpose of this paper to analyze and recommend an alternative possible renewable energy system based on Solar that can be used to improve the socio-economic conditions of North West communities. Employment rate can be enhance and skill transfer be feasible. This is done by using Homer Pro Software to analyse and recommend the possible renewable energy source in terms of deployment and cost.

III. Methodology

Analysis of system requirement in terms of cost was conducted using Homer Pro. The comparison between the on-grid and off-grid system was carried out. The sensitivity results were also of utmost importance. The month of June-July during the year was chosen as it is the peak month for electricity usage. The following criterion was considered during simulation;

- Location selected is Taung.
- The cost is in South African currency.
- Solar PV system is chosen as an on-grid or off-grid system.
- Energy storage to be used is lead-acid battery at 1kWh/day.
- Generator cost to be 10.15/kW.
- Discount rate to be kept at 7%.

The methodology chosen provide clear considerations of the type of renewable system to select in terms of cost and future development. Firstly on the analysis, the assumptions that are made includes; projection discount to be 6%. The average load of 11.13 kW-h/day, with peak usage month of month of June-July is considered. The residential load profile is selected. No grid is added during this simulation. Further assumptions are made that the generator cost is R10.15/kW with the fuel cost of R11.63/l maybe required. However, the renewable energy system is Solar PV with a capital cost of R3000/kW. No wind turbine is included in this system simulation. An energy storage system of generic 1kW-h lead-acid battery is used with the assumption cost of R300/kW-h. The South African inflation rate is kept at 6% for the purpose of this simulation. Homer Pro suggested various systems to be considered for the implementation of renewable energies with different costs allocated to them. Hence the successful simulation is conducted through and without any disruptions or error erupted.

The design of the system development is shown in figure 1 below.

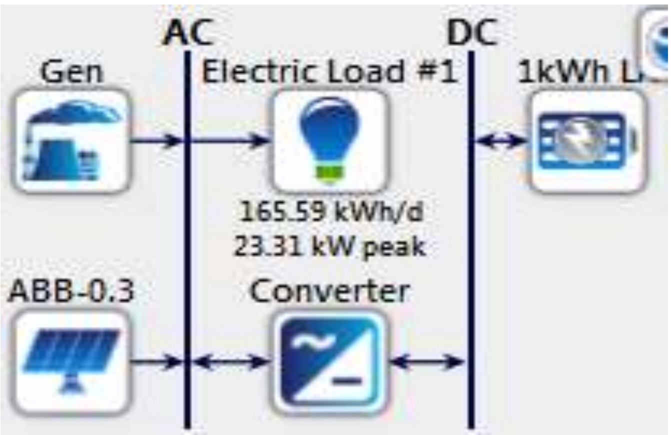

Figure 1 Schematic development of the system in Homer Pro Software.

The generator set is assumed to have the following characteristics;

- Fuel: Diesel.
- Fuel curve intercept: 1.07 l/hr.
- Curve slope: 0.25 l/hr/kW.

Therefore in terms of emission, the following are present;

- CO (g/l fuel): 16.5
- Unburned HC: 0.72 g/l fuel.
- Particulates: 0.1 g/l fuel.
- Fuel sulfur to PM: 2.2%.
- NO_x: 15.5 g/l.

It is further assumed that the generator set utilizes a particular fuel of diesel, which has the below properties;

- Lower Heating Values: 43.2 MJ/kg.
- Density: 820 kg/m^3.
- Carbon content: 88%.
- Sulfur content: 0.4%

In this research study, the generator automatically sizes itself to meet the load demand. The capacity of the generator will be the smallest and will produce no capacity shortage in all the sensitivity cases. It also adjust the fuel curve match its size.

A. Control

For the system control, the homer load following control strategy is used. This strategy is used to as a dispatch strategy, whereby, whenever a generator operates, it produces only enough power to meet the primary load. Lower priority objectives such as charging the storage bank or serving the deferrable load are left to the renewable power sources, in this case is solar PV. The generator ramps up and sell power to the grid if it is economically advantageous.

B. Energy Storage

The generic 1kwh Lead Acid Battery (LAB) is used as an energy storage bank for this research study. This is due to their robustness, deep cycling capability and tolerant to temperature changes amongst other advantages. Figure 2 shows the battery capacity curve.

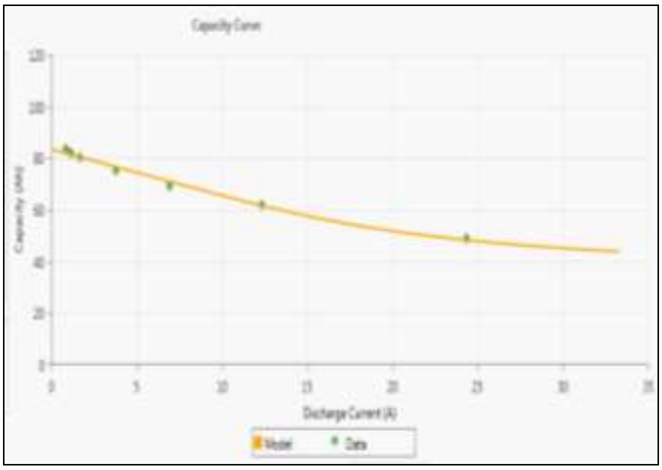

Figure 2. Lead Acid Battery Capacity curve.

In Fig.2 it is illustrated that the battery capacity is increased if the discharge current is significantly reduced. Therefore, this leads to the control strategy of the dispatch to allow the storage device hold great capacity.

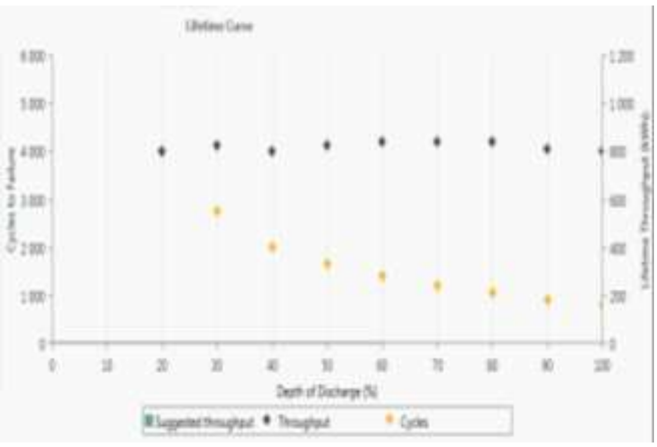

Figure 3. Lead Acid Battery lifetime curve.

Figure 3 shows the chosen battery lifetime curve. It is shown that the battery failure is highly dependent on depth-of-discharge. Therefore, this research study uses deep cycle lead acid batteries because their throughput lifetime is great. Thus the characteristics of these batteries is shown in figure 3 above.

IV. RESULTS AND DISCUSSIONS

The AC primary load and the PV power output for the month of June-July is captured and indicated in figure 6 below, the optimum AC load is above 2kW and the PV output is 2.7kW. The results obtained herewith are for PV system with converter and the energy storage system. The system results are optimized by including the off-grid system, thus indicating which system will be cost effective to deploy. However during the month of June-July, the sensitivity of the increase price of fuel and population by 5% in the following year were also taken into consideration.

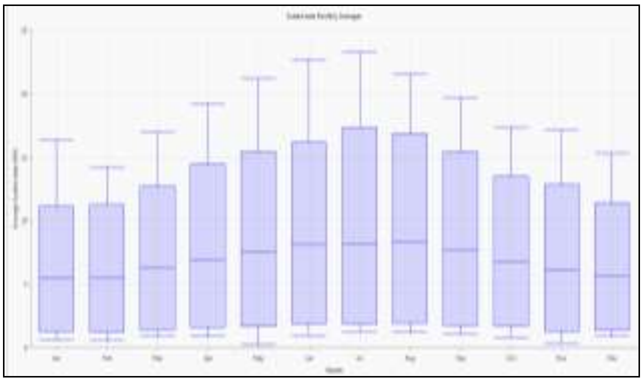

Figure 4. Annual Power demand for Taung village.

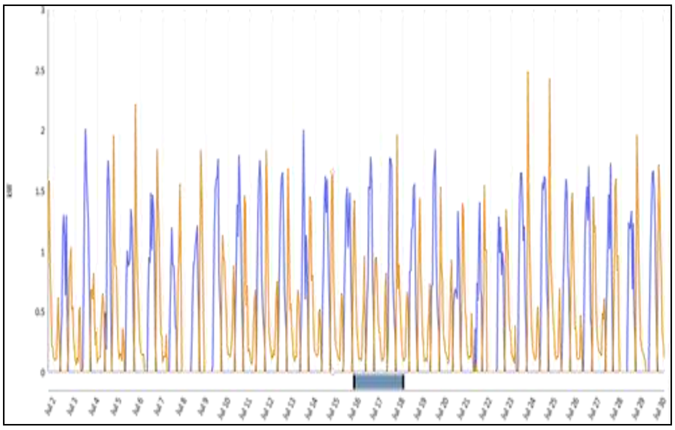

Figure 5. Battery charge and discharge power.

Fig 1. Shows the average annual power demand for Taung village at North West Province. The highest power demand occurs during the month of June-July at an average of 24kW. The results of these research study are hence, based on the Jun-Jul month as indicated in Fig.1 above. Consequently, Fig.2 shows the battery charge and discharge during the operation of the micro-grid. The maximum discharge power indicated is 2.8 kW, therefore deep cycle batteries are suitable for this application. The economics of the grid system and off-grid system were compared and the off-grid system resulted in very low prices in terms of cost, operation and lifetime. Therefore, Figure 3 below shows the cost of different components of the system.

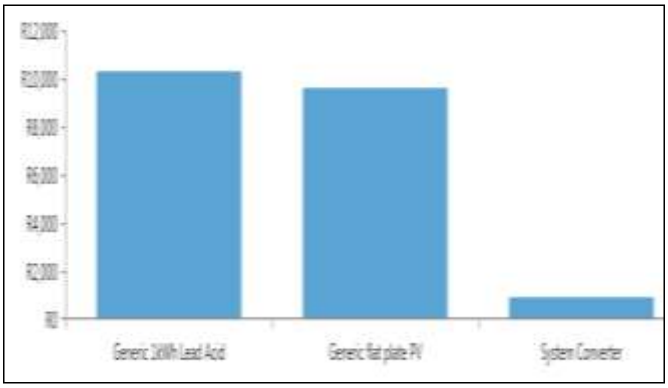

Figure 6. Cost summary of components for off-grid system.

In Fig.3 it is indicated that the energy storage for the system cost approximately R10900.00, the PV flat plane around R 9000.00 and lastly the system converter of the energy storage device cost is R 1000.00. The results as indicated in Fig.3 are the summary of the cost for the off-grid system approach. Moreover, figure 4 below shows the cost of the system integrated with the grid.

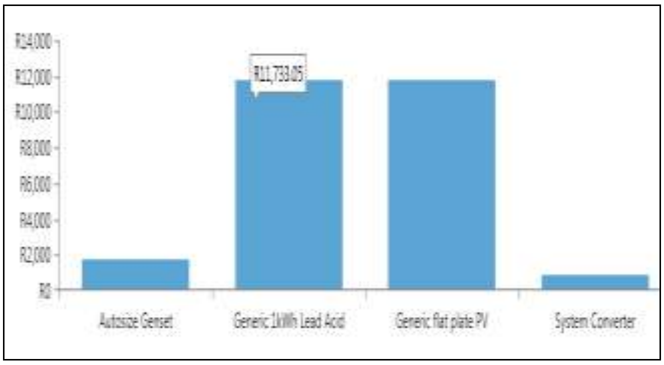

Figure 7. Cost summary for an on-grid system components.

As shown in Fig.4, the cost of the generator set is R 2000.00. This generator sizes itself to meet the load demand. Hence, the capacity of the generator is small and is capable of producing no capacity loss or shortage in all sensitivity cases presented in this research study. Therefore, table I below shows the systems operating cost.

TABLE I OPERATING SYSTEMS COST

Component	Capital(R)	Replacement(R)	O&M(R)
Generic 1kWh Lead Acid	5 100.00	4 070.00	1 333.34
Generic flat plate PV	9 390.97	0	245.51
System Converter	770.04	140.68	0
System	15 251.01	4 211.08	1 578.85

As shown in table I, the summary of the components cost is clearly indicated. Table II below, describes the continuation of the operating systems cost above as described in table I.

TABLE II OPERATING SYSTEMS COST.

Component	Fuel(R)	Salvage(R)	Total(R)
Generic 1kWh Lead Acid	0	0 165.96	10 337.78
Generic flat plate PV	0	0	9 636.48
System Converter	0	0 015.10	0 895.62
System	0	0 181.06	20 869.88

Table II above indicate that there are no fuels that are being utilized during the systems operation, hence, the system is emission free.

TABLE III CAPITAL AND OPERATING COST FOR ON-GRID SYSTEM.

Component	Capital(R)	Replacement(R)	O&M(R)
Autosize Genset	27.41	0	35.57
Generic 1kWh Lead Acid	6 300.00	3 887.36	1 647.07
Generic flat plate PV	11 436.71	0	298.99
System Converter	740.01	135.20	0
System	18 504.13	4 022.56	1 981.63

Table III describes the capital required as well as the operating cost analysis for the on-grid tied system.

TABLE IV CAPITAL AND OPERATING COST FOR ON-GRID SYSTEM.

Component	Fuel(R)	Salvage(R)	Total(R)
Autosize Genset	1 710.62	1.46	1 772.14
Generic 1kWh Lead Acid	0	101.38	11 733.05
Generic flat plate PV	0	0	11 735.70
System Converter	0	14.51	860.70
System	1 710.62	117.35	26 101.59

Table IV is the continuation of Table III, and it clearly indicate the cost of the on-grid tied system. The result indicate that the cost of the on-grid tied system is higher than that of the off-grid. Hence, the usage of the on-grid system uses the fuel, as this is a disadvantage as compared to off-grid. The fuel usage contribute significantly to the carbon emission to the climate. Therefore, it is of this critical disadvantage to use the off-grid system and to play an important role in minimizing gas emissions to the climate.

V. Conclusion and Recommendations

Homer Pro software is very useful for analysis of suitable renewable systems for deployment in rural areas. As indicated on the results, the cost of off-grid system for deployment in rural areas is cheaper than the traditional on-grid system deployment in terms of capital and operating cost. Taungs' required residential load is therefore not large as it can be assumed. The analyzed renewable system indicate that the capital cost is less and can be developed to sustain the area for the entire year. This also indicate that the system will be more efficient even in summer due to less usage of electricity during that season. It is therefore recommended that further analysis be conducted to evaluate the sensitivity of population growth of 2% and physically deploying the system as to ensure socio-economic development for the poor is well attained. Moreover, not only enhancing the socio-economic well fair, but increasing chances for unemployment rate to reduce significantly and positive economic impact as well as significant carbon emission reductions.

Acknowledgment

The authors would like to acknowledge the Tshwane University of Technology, Pretoria, Department of Science and Technology, Eskom and Taung community for providing necessary research infrastructure to conduct this research.

References

[1] C. L. Azimoh, P. Klintenberg, F. Wallin, B. Karlsson, and C. Mbohwa, "Electricity for development: Mini-grid solution for rural electrification in South Africa," Energy Convers. Manag., vol. 110, pp. 268–277, Feb. 2016.

[2] R. Spalding-Fecher et al., "Electricity supply and demand scenarios for the Southern African power pool," Energy Policy, vol. 101, pp. 403–414, Feb. 2017.

[3] S. Baurzhan and G. P. Jenkins, "Off-grid solar PV: Is it an affordable or appropriate solution for rural electrification in Sub-Saharan African countries?," Renew. Sustain. Energy Rev., vol. 60, pp. 1405–1418, Jul. 2016.

[4] Z. Xu, M. Nthontho, and S. Chowdhury, "Rural electrification implementation strategies through microgrid approach in South African context," Int. J. Electr. Power Energy Syst., vol. 82, pp. 452–465, Nov. 2016.

[5] S. A. O. Ilupeju and F. L. Inambao, "Smart electricity distribution for sustainable development in Southern Africa sub-urban settlements," in 2014 International Conference on the Eleventh industrial and Commercial Use of Energy, 2014, pp. 1–8.

[6] C. Kirubi, A. Jacobson, D. M. Kammen, and A. Mills, "Community-Based Electric Micro-Grids Can Contribute to Rural Development: Evidence from Kenya," World Dev., vol. 37, no. 7, pp. 1208–1221, Jul. 2009.

[7] J. Urpelainen, "Grid and off-grid electrification: An integrated model with applications to India," Energy Sustain. Dev., vol. 19, pp. 66–71, Apr. 2014.

[8] P. Cook, "Infrastructure, rural electrification and development," Energy Sustain. Dev., vol. 15, no. 3, pp. 304–313, Sep. 2011.

[9] S. C. Bhattacharyya and D. Palit, "Mini-grid based off-grid electrification to enhance electricity access in developing countries: What policies may be required?," Energy Policy, vol. 94, pp. 166–178, Jul. 2016.

[10] "North West municipalities." [Online]. Available: https://www.localgovernment.co.za/provinces/view/8/north-west. [Accessed: 15-Jun-2017].

2019 SAUPEC/RobMech/PRASA Conference
Bloemfontein, South Africa, January 28-30, 2019

Application of Artificial Intelligence Technique in Predicting 7-Days Solar Photovoltaic Electrical Power

Raymond O. Kene*, SP. Daniel Chowdhury, Thomas O. Olwal
Department of Electrical Engineering, Tshwane University of Technology, Pretoria, South Africa
rayykene@yahoo.com*, spchowdhury2010@gmail.com, olwalto@tut.ac.za

***Abstract*— To be able to dispatch electrical power effectively to consumers using solar photovoltaic (SPV) cells, there is a need to have information about the SPV power generation. This information is best derived from predicting the SPV power ahead of any supply. Artificial neural network intelligence technique is employed in this study with the aim of predicting SPV electrical power for a period of 7 days. The maximum power produced on a daily basis is been identified as well as the daily average power that is produced and predicted. With this information, the short-term availability of daily solar irradiation can be maximized. A statistical regression analysis has been used to establish the relationship between the produced and predicted power, using statistical functions like the mean bias error (MBE), the mean square error (MSE), root mean square error (RMSE), mean absolute deviation (MAD), mean absolute percentage error (MAPE), and the correlation coefficient (CC). The algorithm used in training the network is the backpropagation algorithm with feed-forward neural network. A total of 14,300 datasets have been used to establish this study with the application of artificial neural network (ANN) for prediction analysis. The result indicates that, the uncertainty in SPV power generation can be mitigated using ANN to predict its performance, thereby creating visibility as to what the SPV system can generate. This enables load balancing, efficient power dispatch and accurate scheduling.**

***Index Terms*-- SPV, artificial intelligence, neural networks, SPV prediction, backpropagation, error functions.**

I. Introduction

The integration of renewable energy sources as a mix to the existing electricity network is gaining popularity, with solar energy been the most used alternative source of electricity supply. Solar photovoltaic (SPV) application has reached a global cumulative of about 177GW of installed capacity as at 2014 [1]. This growth has been fueled largely by government policies and incentives which encourages independent power producers to participate in the energy sector, in order to boost the movement for green economy and saving our earth.

But the short-term availability of solar power has made SPV systems unreliable due to the intermittent electricity supply [2]. The effects of this nonlinear characteristics of the SPV [3], leads to equipment failures and operational mishaps. In addition to the numerous challenges and problems encountered with the short-term availability of SPV power, it is even more difficult to manage [4] the SPV power supply because, the SPV electrical power production profile cannot be established. Research findings has been able to establish that, modeling and prediction of SPV power can help minimize the losses and impacts of the intermittent SPV power supply to loads. Amongst which, wavelet transform (WT) and deep convolutional neural network (DCNN) have been used by Huaizhi *et al.* [5] to reduce the negative impacts of SPV power.

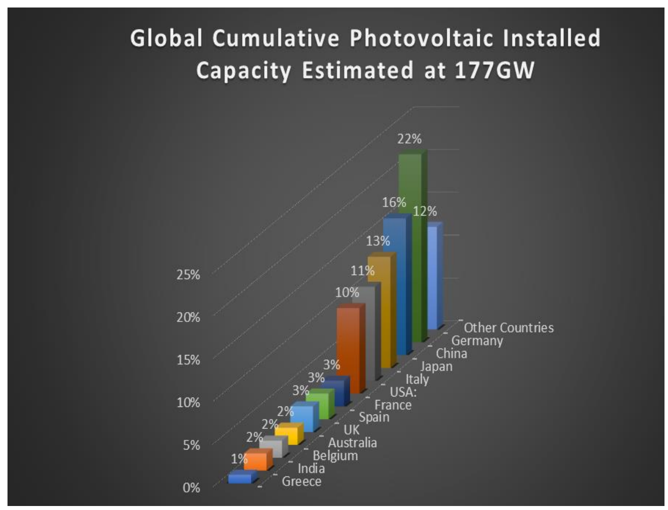

Fig.1. Global cumulative PV capacity end 2014 [1].

II. Related Work

The application of SPV energy systems and integration for both private and commercial consumption, requires smart intelligence that is able to manage the limited available SPV power. To this end, the application of artificial intelligence techniques with other related techniques have been applied directly and indirectly to SPV power systems to achieve reasonable forecasting models. The work of Yona *et al.* [6],

978-1-7281-0368-6/19/$31.00 ©2019 IEEE

made use of neural network application to forecast SPV power generation. Hossain *et al*. [7] used a model which involved extreme learning machine (ELM) to determine the power output of grid-connected SPV plants. Oudjana *et al.* [8], employed the use of artificial neural network with regression model to forecast the power of a SPV, where solar irradiance and temperature are inputs to the model. Hybrid models have also been employed to forecast SPV power as in the case of Zhu *et al.* [9], where wavelet decomposition and ANN was used as a forecasting model for PV power plant. The accuracy of ANN in the calculation of the energy provided by a SPV generator was carried out by Almonacid *et al.* [10]. In the research work conducted by Saberian *et al.* [11], feed-forward neural network with back propagation algorithm was used to model and predict SPV output power. Naci *et al.* [12], conducted a study to predict the operating current of a SPV using a generalized regression neural network (GRNN), the result was satisfactory when compared to other models.

This conference paper proposes the use of neural network as an artificial intelligence technique, to model and predict the electrical power produced from an array of SPV modules. It will focus on a 7-days SPV electrical power prediction, as opposed to models that are limited to an hour ahead and 24 hours ahead predictions. This study also contributes to existing research studies, by making use of real time datasets obtained from the SPV array under operational conditions, as opposed to previous studies which makes use of numerical weather datasets. The benefit of this study also includes the advantage of knowing how most SPV cells/array will behave in real-time conditions.

III. Artificial Intelligence Model Description

The model applied to this study involves the use of a multilayer perceptron feed-forward neural network with backpropagation algorithm. A typical architecture of the ANN used for this study is given as in Fig.2.

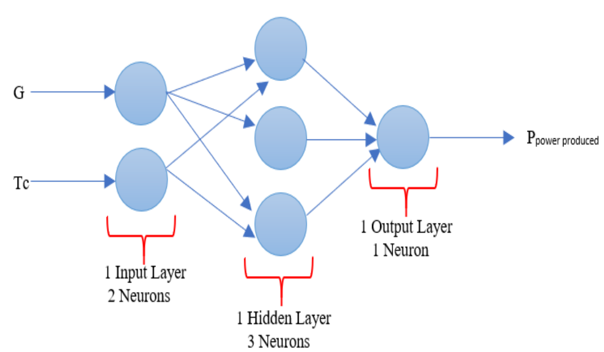

Fig.2. FFNN MLP Structure with 3-Layers

A. Data Analysis

Weather datasets which relates to the local climate solar insolation (G) with units in watts per square meter (W/m^2) and the module temperature (T_c) with units in degree Celsius (°C) have been collected. Other datasets relate to the SPV electrical parameters which includes SPV array current, voltage, DC electrical power (W) and the inverter AC power (W) produced. All datasets have been collected at 15-minutes interval. More than 17,875 datasets analysed for this study.

B. ANN Modeling of SPV Electrical Power

Artificial neural network as explained by McCulloch and Pitts as far back as 1943 [13]; has been very useful in the field of electrical engineering [14]. The McCulloch-Pitts model can be mathematically represented with equation (1).

$$Y = F(\sum_{i=1}^{n} x_i \, . w_i + b) \tag{1}$$

C. Ativation Functions

The outputs of ANN depend on the type of activation function applied to it. Activation functions are very crucial in order to process datasets in and out of the neural network. These functions usually transfer the output of the neurons from one layer to the next in a feed-forward fashion [15]. The following activation function can be used in ANN models:

I. Logsigmoid Activation Function

One of the most popular activation function applied to the neural network is the Logsigmoid transfer function. It processes the ANN inputs ranging from negative infinity (- ∞) to positive infinity (+ ∞) and gives output which ranges from zero to one. So, in most cases, the logsigmoid function is used when the expected neural network output should be in the positive range (i.e. 0 to + ∞). The logsigmoid function is represented by the equation (2) below:

$$f_{(y)} = \frac{1}{1 + e^{-x}} \tag{2}$$

The Logsigmoid is also mainly used in feedforward neural network and the backpropagation algorithm because its function can be differentiated.

II. Linear Activation Function

The linear activation (transfer) function mainly takes in the value of the data applied to the input and produces a linear output which goes through positive and negative values. Equation (3) represents the linear activation function.

$$f_{(y)} = x \tag{3}$$

III. Hyperbolic Tangent Function

This function is applied to neural network when the expected output should be a positive or negative value. The hyperbolic tangent function is represented as in equation (4).

$$f_{(y)} = \frac{e^{2x} - 1}{e^{2x} + 1} \quad (4)$$

IV. Simulations, Results and Discussion

Datasets for this simulation exercise was obtained from Rosherville, South of Johannesburg, South Africa (Latitude: 26.2314º S, Longitude: 28.1152º E). The local weather conditions here are such that, solar irradiation begins to reach the earth surface from around 5:00AM local time zone until about 7:00PM.

A. *SPV 7-Days Electrical Power Model Simulation*

The input layer is configured with two neurons which consists of the SPV DC electrical output power, the hidden layers have ten neurons, and the output layer has one neuron consisting of the SPV inverter AC output power.

In this model, Logsigmoid activation function has been applied to the hidden layer for best performance modeling of the SPV modules power predictions. The output of the ANN model utilized the purelin activation function in order to produce the SPV power. The block diagram for this model as derived from the actual MATLAB simulation experiment is shown in Fig.3.

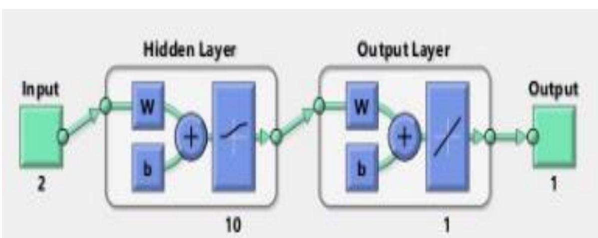

Fig.3. SPV ANN Model Block Diagram.

B. *Training SPV Datasets*

Datasets collected for modeling the electrical power of the SPV array is feed into the ANN machine and have been normalized for processing. During the training process, 16 iterations was achieved, this is the number of epochs with regards to each training conducted. Learning rate value for the training was set to 0.1 making sure that it's not too small or too large in order to optimize training process. Fig.4. depicts the MATLAB training performance

The interpretation of Fig.4. for the SPV model shows that, the mean square error of the developed network has been reduced significantly as indicated by the blue line. The green line indicates the validation error on the network; once the validation error can no longer be reduced, it flags the backpropagation algorithm to stop the network training process.

The red line indicates clearly the error that has been encountered within the test data required for the SPV power prediction and it tells us how the developed ANN model will

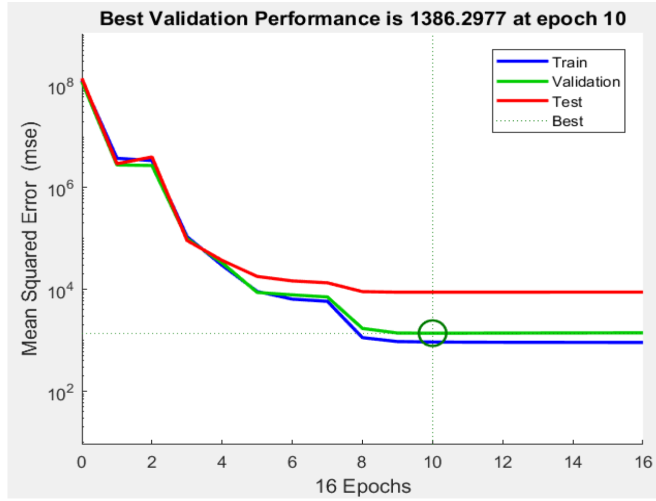

Fig.4. Best Validation Performance

be able to generalize the test data in the accurate prediction of the SPV power. Generalization has to do with the ability of the artificial neural network to determine a correct or an approximate output vector, which can be associated with a given input vector. This generalization property is analogous to the associative memory property which states that: close inputs should produce close outputs.

C. *Regression Analysis*

Statistical analysis of the applied neural network model and algorithm is provided by the regression plots from the network training process. The plots are explained thus:

*1) **Training Regression Plot***

Fig.5. as indicated shows the distribution of the datasets centered around the line of best fit, and no outliers have been found. This an indication that, the developed artificial intelligence (ANN) technique have been able to train the data to fit the predictions of the produced SPV electrical power. This prediction is further strengthened with the correlation coefficient (R) of 0.99998 as seen on Fig.5.

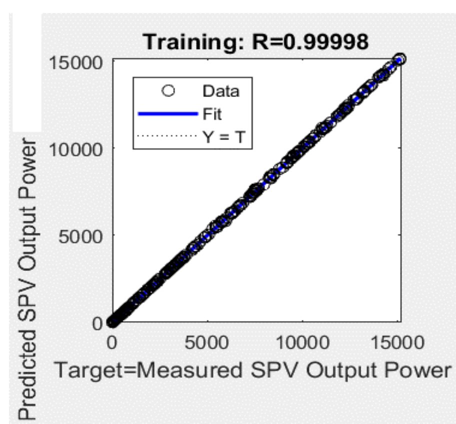

Fig.5. Training Regression Plot

*2) **Validation Plot***

From the validation performance of Fig.4., the network converged at the 10th epoch. At this point, the training process had to stop, since the validation error had reached its minimum.

Fig.6. shows the validation plot with its correlation coefficient (R) at 0.99997. This is a clear indicator that the values of predicted SPV power has a close relationship with the measured values of the SPV array.

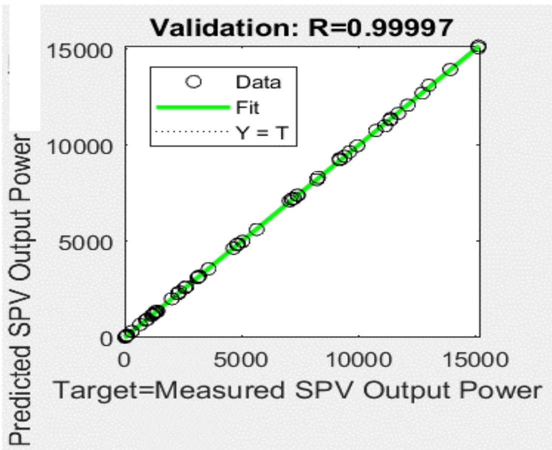

Fig.6. Validation Plot

*3) **Test Plot***

Once training and validation has been conducted, an appropriate testing of the sample datasets used during training and validation is required. This exercise establishes generalization ability of the ANN, on how well it was able to estimate the given input values for an appropriate output value. This can be confirmed by the correlation coefficient (R) figure 0.99983 as shown on the test plot of Fig.7.

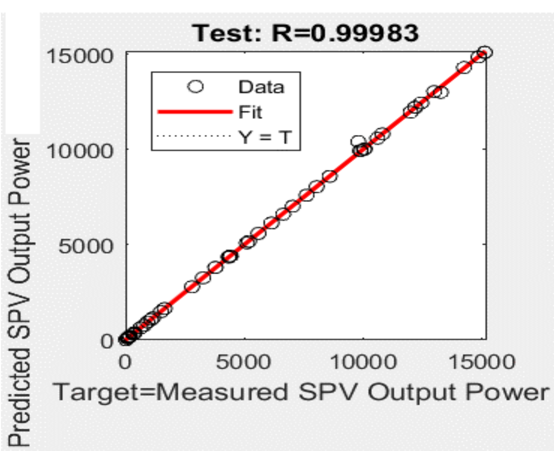

Fig.7. Test Plot

D. Measured and Predicted SPV Output Power

As seen in Fig.8., the actual SPV electrical output power as produced from the SPV array is given. This plot shows seven different SPV power profile as produced from January 22 to 28 of 2016.

A weekly SPV power outlook will go a long way in ensuring that, energy supply is managed according to its production capacity and in relation to meeting the demand-side of the consumers. For a closer look into the weekly power production profile of the SPV array as seen in Fig.8., a snap shot on the SPV power analysis produced for day 6, the 27th January 2016 is given as in Fig.9.

The maximum power produced as seen from Fig.9 was 15,166kW at about 12:15PM in the afternoon, the closest figure to this, is the 15,164kW which was produced at about 12:00 noon time, while at about 11:45AM, 15,160kW was produced. The average SPV power produced on this day was around 6,465kW.

E. Predicted SPV Output Power

Fig.8, is presented, to prove that the applied ANN artificial intelligence technique has high accuracy for SPV electrical power modeling and prediction. A graphical plot is displayed, for the 7-Days SPV power that was predicted, this can be seen directly below the measured SPV values in Fig.8. The correlation coefficient for this prediction is quite high and it stands at 99% accuracy.

V. CONCLUSION

In conclusion, the application of artificial intelligence techniques, in this case artificial neural network, shows high accuracy in predicting the electrical power as produced from the SPV arrays. As seen in Table I, the statistical analysis table shows how close the predicted power is, when compared with the measured power. The 99% correlation coefficient figure of merit as obtained from the network simulation, is also a clear indicator that the predicted power is close to the power produced from the array of SPV in the plant. Therefore, the ANN has a generalization property of associating close inputs to close outputs. The simulation has been carried out using the MATLAB software.

This study had a focus on a 7-days SPV electrical power prediction, as opposed to models that are limited to an hour ahead and 24 hours ahead predictions.

This paper contributes to existing research studies through the use of real time datasets obtained from the SPV array under real time operational conditions, as opposed to previous studies which makes use of numerical weather datasets. In addition, this study provides the advantage and benefit of knowing how most SPV cells/array will behave in real-time conditions.

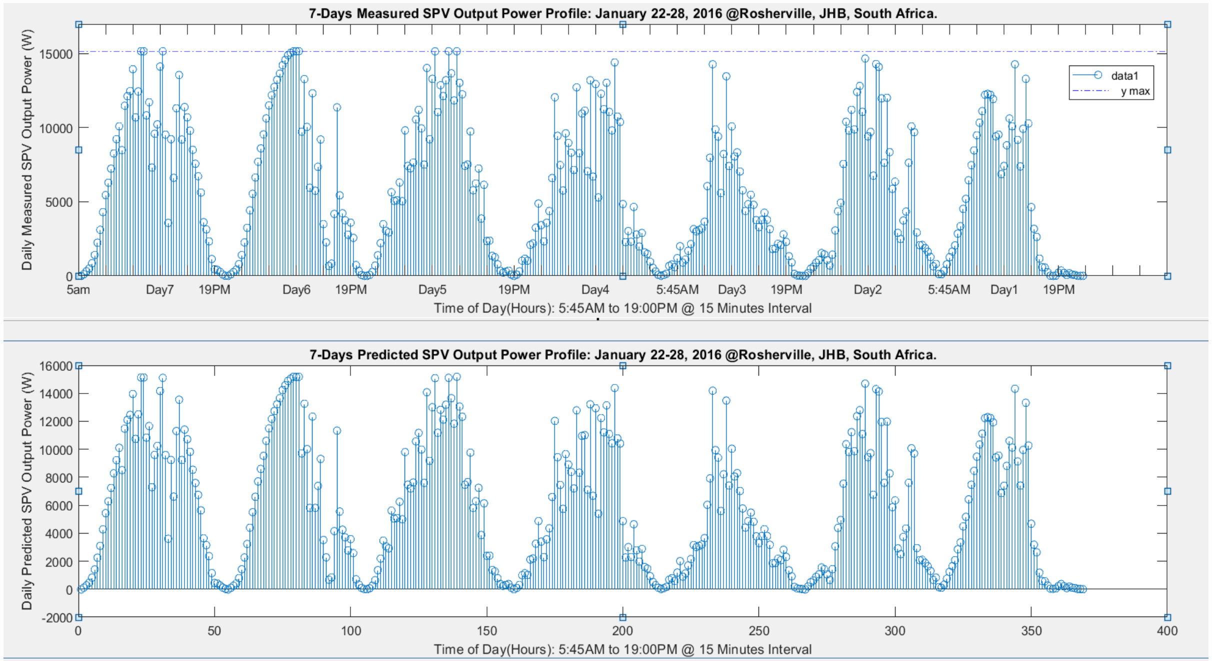

Fig.8: 7-Days Measured and Predicted SPV Output Power Profile: January 22-28, 2016 @Rosherville, JHB, South Africa.

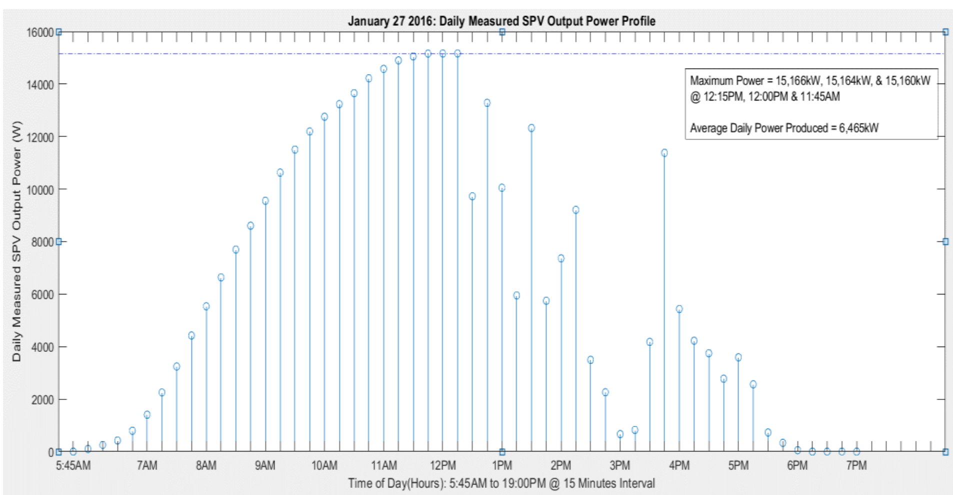

Fig.9.January 27 SPV Output Power Profile

TABLE I. 7-DAYS STATISTICAL ANALYSIS FOR SPV MEAASURED AND PREDICTED ELECTRICAL POWER OUTPUT

DATE	TIME	MEAN MEASURED AC POWER (W)	ANN MEAN PREDICTED POWER (W)	MBE	MSE	RMSE	MAPE	MAD	CORRELATION COEFFICIENT(R)
1/22/2016	5:45AM -7:00PM	4916.309074	4927.83	-11.5209743	517.23	22.74271852	9.48032694	17.90388667	0.999992651
1/23/2016	5:45AM -7:00PM	5231.363333	5238.43	-7.063268349	498.8531831	22.33502145	0.850832634	15.94389597	0.999989749
1/24/2016	5:45AM -7:00PM	3813.942222	3821.98	-8.042735393	691.0494903	26.28782019	7.965040948	17.88978541	0.99997878
1/25/2016	5:45AM -7:00PM	5855.708148	5880.38	-24.667073	9137.749904	95.59157863	1.696341431	41.75	0.999804762
1/26/2016	5:45AM -7:00PM	6631.991852	6643.23	-11.23365023	5381.59	73.3593214	3.02	45.13537198	0.999889306
1/27/2016	5:45AM -7:00PM	6464.481296	6473.43	-8.951268802	1560.256237	39.50007895	1.510458918	23.64547982	0.999975681
1/28/2016	5:45AM -7:00PM	7133.346852	7152.75	-19.3988149	20320.95706	142.5515944	5.43405777	19.3988149	0.999991639

ACKNOWLEDGMENT

The authors of this paper would like to acknowledge the research support provided by Tshwane University of Technology, the National Research Foundation, Council for Scientific and Industrial Research and Eskom South Africa.

REFERENCES

[1] International Energy Agency (IEA): Photovoltaic power systems programme, Trends 2015. In: Photovoltaic applications - survey report of selected IEA countries between 1992 and 2014.

[2] J.M. Vindel and J. Polo, 2014. Intermittency and variability of daily solar irradiation. In: Atmospheric Research 143(2014). Elsevier. 313-327.

[3] Zheng Zeng, Huan Yang, Rongxiang Zhao and un Meng, 2013. Nonlinear characteristics of observed solar radiation data. In: Solar Energy 87 (2013). Elsevier. 204-218.

[4] A.S.O. Ogunjuyigbe, T.T. Ayodele and O.E. Oladimeji, 2016. Management of loads in residential buildings installed with PV systems under intermittent solar irradiation using mixed integer linear programming. In: Energy and buildings 130(2016). Elsevier. 253-271.

[5] Huaizhi Wang, Haiyan Yi, Jianchun Peng, Guibin Wang, Yitao Liu, Hui Jiang and Wenxin Liu, 2017. Deterministic and probabilistic forecasting of photovoltaic power based on deep convolutional neural network. In: Energy conversion and management 153(2017). Elsevier. 409-422.

[6] Yona A., Senyiu T., Funabshi T., Sekine H., 2008. Application of neural network to 24-hours-ahead generating power forecasting for PV system. In: IEEJ Trans Power Energy 128(2008). 33-39.

[7] Hossain M., Mekhilef S., Danesh M., Olatomiwa L., and Shamshirband S., 2017. Application of extreme learning machine for short term power forecasting of three grid-connected PV systems. 2017, 395-405.

[8] Oudjana SH., Hellal A., Mahamed IH., 2012. Short term photovoltaic power generation forecasting using neural network. In: Proceedings of the 11th international conference on environmental and electrical engineering (EEEIC). IEEE. 2012. 706-711.

[9] Zhu H., Li X., Sun Q., Nie L., Yao J., and Zhao G., 2015. A power prediction method for photovoltaic power plant based on wavelet decomposition and artificial neural networks. In: Energies 2015. Elsevier.

[10] F. Almonacid, C. Rus, P. Perez-Higueras and L. Hontoria, 2011. Calculation of the energy provided by a PV generator. Comparative study: Conventional methods vs. artificial neural networks. In: Energy 36(2011). Elsevier. 375-384.

[11] Saberian A., Hizam H., Radzi MAM., Kadir MZAA., and Mirzaei M., 2014. Modeling and prediction of photovoltaic power output using artificial neural networks. In: International journal for Photoenergy. 2014. 1-10

[12] Naci Celik A., Artificial neural network modeling and experimental verification of the operating current of mono-crystalline photovoltaic modules. In: Solar energy 85(2011). 2507-17.

[13] Simon Haykin, 1999. Neural networks: a comprehensive foundation, 2nd Edition, ISBN. 81-7808-300-0, Pearson Education Publishing (Singapore).

[14] H. Silver. Neural networks in electrical engineering. In Proceedings of the ASEE New England Section 2006 Annual Conference.

[15] Abul Kashim Md. Fujail, Shahin Ara Begum, and Abdul Karim Barbhuiya. Comparison of artificial neural network transfer functions abilities to predict scour depth around bridge abutment. In: Elsevier. 65-70.